Adaptive Rollover Control Algorithm Based on an Off-Road Tire Model

Brad Michael Hopkins

Thesis submitted to the faculty of the
Virginia Polytechnic Institute and State University
in partial fulfillment of the requirements for the degree of

Master of Science
In
Mechanical Engineering

Saied Taheri, Chair
Mehdi Ahmadian
Steve C. Southward

November 30, 2009
Blacksburg, VA

Keywords: off-road tire model, Pacejka Magic Formula, scaling factors, adaptive control, vehicle handling stability

Adaptive Rollover Control Algorithm Based on an Off-Road Tire Model

Brad Michael Hopkins

Abstract

Due to a recent number of undesired rollovers in the field for the studied vehicle, rollover mitigation strategies have been investigated and developed. This research begins with the study of the tire, as it is the single component on the vehicle responsible for generating all of the non-inertial forces to direct the motion of the vehicle. Tire force and moment behavior has been researched extensively and several accurate tire models exist. However, not much research has been performed on off-road tire models. This research develops an off-road tire model for the studied vehicle by first using data from rolling road testing to develop a Pacejka Magic Formula tire model and then extending it to off-road surfaces through the use of scaling factors. The scaling factors are multipliers in the Magic Formula that describe how different aspects of the force and moment curves scale when the tire is driven on different surfaces. Scaling factors for dirt and gravel driving surfaces were obtained by using an existing portable tire test rig to perform force and moment tests on a passenger tire driven on these surfaces. The off-road tire model was then used as a basis for developing control algorithms to prevent vehicle rollover on off-road terrain. Specifically, a direct yaw control (DYC) algorithm based on Lyapunov direct method and an emergency roll control (ERC) algorithm based on a rollover coefficient were developed. Emergency evasive maneuvers were performed in a simulation environment on the studied vehicle driven on dry asphalt, dirt, and gravel for the controlled and uncontrolled cases. Results show that the proposed control algorithms significantly improve vehicle stability and prevent rollover on a variety of driving surfaces.

Acknowledgement

I first thank the Holy Spirit for friendship, company, advice, guidance, comfort, encouragement, and laughter. I thank Jesus for my salvation, for opening the doors that only He can open and closing the doors that only He can close. I thank God the Father for love, relief, provision, and His grace that brings me to places that I could never get to on my own.

I thank Mom and Dad for loving me and supporting me, and for having hearts to continually give to me (in many ways), regardless of what I choose to do.

I thank Dr. Taheri for being an awesome advisor and providing the opportunity for me to do this research. I thank Dr. Ahmadian for his advice along the way, and Dr. Southward for his advice and his controls class.

I would also like to thank a number of my peers who played a large role in the completion of my research: Josh Caffee for allowing me to live at his house and for helping out with the tire test rig and testing; Bryan Sides for helping make the test rig operational, for helping with testing, and for driving the trailer to Blacksburg and back; Michael Craft for answering all my questions and for helping with the completion of the test rig; William Burke for helping with the design of the test rig; Hossein Tammadoni for help with the control algorithms; Brian Templeton for advice on curve-fitting. I would also like to thank Harry Gong for his advice on the curve-fitting routine and Nenggen Ding for his help with the control algorithms. I also thank Sue Teel for helping out with the logistics around the lab. I thank Al Reid and Jose Mabesa at TACOM for funding this research and allowing it to be possible. I also thank Danville Regional Airport, the Department of Animal and Poultry Sciences at Virginia Tech, and Wright Patterson Air Force Base for providing facilities to perform tire testing.

Table of Contents

List of Tables

All tables property of Brad Hopkins

List of Figures

All figures property of Brad Hopkins

Chapter 1: Introduction

This research focuses on the development of an off-road tire model that was used in vehicle handling performance and stability studies. Specifically, rollover mitigation for the studied vehicle was desired. The off-road tire model developed in this research was used as a foundation for developing stability control algorithms for preventing vehicle rollover.

This chapter first explains the motivation behind this research, which includes the problem description. Next, the general approach behind solving the problem is explained. Finally, an outline of the thesis is provided.

1.1: Motivation

The vehicle studied in this research has previously experienced an undesired number of rollovers while being driven on off-road surfaces. These rollover instabilities are caused by a combination of vehicle properties, tire properties, and terrain conditions. The tire is the component of the vehicle responsible for supplying all non-inertial forces that will direct the motion of the vehicle, therefore it is important to understand the tire for accurate vehicle handling performance and stability studies. Because of the lack of existing literature on the force and moment behavior of tires on off-road terrain, this research first focused on developing a tire model suitable for off road conditions. Gaining an understanding of the tire behavior while being driven on off-road terrain provides insight into how the vehicle will perform. This is accomplished by utilizing the tire model in a simulation environment capable of providing vehicle dynamic performance responses to various steering, braking, and throttle inputs. From here, control algorithms can be developed that will increase vehicle roll stability on a variety of driving surfaces, thus helping to prevent vehicle rollover

1.2: Research Approach

The first step in this research was to establish the tire force and moment properties for various levels of load, speed, camber, and slip angle inputs. This was first accomplished by performing force and moment testing on the studied tire on a rolling road. A rolling road is an indoor test facility that simulates a driving surface and is able to apply various vertical loads, slip angles, and camber angles to the tire. Next, a Matlab script was developed that receives the force and moment data from the rolling road tests and creates a tire model. The tire model used is the Pacejka Magic Formula (MF), which is capable of accurately describing the force and moment behavior of a tire as a function of vertical load, slip angle, and camber angle. The MF is widely used in the automotive industry because of its ability to accurately interpolate within the range of tested values as well as extrapolate outside of it.

Next, a hardware control and data acquisition system was designed for an existing portable tire test rig to perform off-road tire testing. Using the rig, tests were performed on a passenger tire on dry asphalt, dirt, and gravel. The dry asphalt tests were used as a baseline to develop scaling factors for the dirt and gravel driving surfaces. This is due to the fact that lab test data for the same tire was available which was collected on a surface that closely mimics the dry asphalt road surface. The scaling factors essentially characterize the driving surface independent of vehicle type, tire size and type, and forward speed. This allows for the force and moment model of the studied tire that was developed on the rolling road to be extended to dirt and gravel driving surfaces. An off-road tire model for the studied tire is then formed without having to perform off-road tire testing on it. This is time and cost efficient because of the difficulty in developing an off-road tire test rig that could accommodate a tire of such large size.

The off-road tire model is then placed in a full vehicle model so that off-road simulations can be performed. Stability control algorithms were then investigated and developed to prevent rollover for the studied vehicle. Specifically, a direct yaw control (DYC) algorithm and an emergency roll control (ERC) algorithm are developed and implemented in the vehicle model. Simulations were run to test the robustness of the control algorithms on dry asphalt, dirt, and gravel driving surfaces.

1.3: Thesis Outline

Chapter 2 is a summary of the literature that was used in this research. This includes literature related to the physics of vehicle rollover, tire modeling, yaw stability control, and roll stability control. Chapter 3 discusses the sign convention and nomenclature that were used in the development of the tire model. Concepts such as slip angle and camber angle are introduced and explained. The force and moment testing of the studied tire that was performed on a rolling road is also discussed in this chapter. Chapter 4 discusses the portable tire test rig that was used for off-road tire testing, as well as the development of the hardware control and data acquisition software. Validation of the rig is shown, and the off-road tire test procedure is explained. Chapter 5 explains the Pacejka Magic Formula and the Matlab script that was developed for transforming the collected tire data into a force and moment tire model. The baseline model for the studied tire is presented. This chapter also discusses the development of scaling factors from the off-road tire test data. The scaling factors are applied to the model of the studied tire to produce an off-road tire model for use in vehicle dynamics studies. Chapter 6 explains the vehicle models used in this research. TruckSim vehicle simulation software is explained, and a two degrees of freedom vehicle model is developed as a basis for developing control algorithms.

Chapter 7 covers some concepts in the physics of vehicle rollover and then proceeds in developing a yaw stability control algorithm and an emergency roll algorithm, both of which are used for the prevention of vehicle rollover. The control algorithms are implemented into Matlab Simulink and linked with TruckSim to test their performance. Emergency maneuvers are performed on the studied vehicle, which includes the developed tire model, for the controlled and uncontrolled cases. Simulations with the vehicle containing the developed off-road tire model are also run on simulated dirt and gravel surfaces to show the robustness of the controllers. Chapter 8 contains conclusions of the research and offers recommendations for any user of this research. Chapter 9 discusses future work to be performed in this area of research.

Chapter 2: Review of Literature

In order to gain a better understanding of tire modeling techniques and vehicle stability behavior, a search of existing literature was performed. The review of literature is separated into three categories: tire modeling, vehicle rollover, and vehicle yaw and roll control and stability. Each one will be examined in the following sections. After that, conclusions that have been drawn from the literature will be presented. These conclusions are useful in the research that is presented in the following chapters.

2.1: Review of Tire Model Literature

The tire model for the studied vehicle in this paper was developed from the Magic Formula tire model. The Magic Formula is a semi-empirical tire formula developed by Hans Pacejka [1], [2], [3]. The general form of the Magic Formula is:

$$N = D\sin\left(C\arctan\left(B\left(x+S_H\right)-E\left(B\left(x+S_H\right)-\arctan\left(B\left(x+S_H\right)\right)\right)\right)\right)+S_V \qquad (2.1)$$

where N is a force or moment acting on the tire, x is the tire slip, either slip angle or longitudinal slip, and B, C, D, E, S_H, and S_V are coefficients that are a function of the tire camber angle and the vertical load acting on the tire. This formula can be used to model tire characteristics for lateral force, aligning moment, and overturning moment as a function of slip angle, and longitudinal force as a function of longitudinal slip. The coefficients B, C, D, E, S_H, and S_V, called main coefficients, are defined individually for each force or moment, and are further defined by more coefficients, called Pacejka coefficients.

The Magic Formula is a semi-empirical formula. Force and moment data is collected for several combinations of tire slip, tire camber angle, and tire vertical load and then curve-fitted to obtain a set of Pacejka coefficients. The set of Pacejka coefficients is used with the definitions of the main coefficients and the Magic Formula from equation (2.1) to accurately predict the force or moment response of the tire. Chapter 5 discusses the Magic Formula in greater detail.

In [4] the Magic Formula is used to model tires from tire data collected on the road. It is shown that on the road tire testing (as compared to rolling road testing) is beneficial for vehicle dynamics studies.

The determination of Pacejka coefficients from the MF is presented in [5]. It is shown that initial guesses for the coefficients can be determined by intuition and reasoning. The values of the coefficients can then be determined by using the initial guesses with an optimization routine.

In [6] the modeling of overturning moment vs. slip angle was explored. It is known that overturning moment is defined as the pneumatic scrub times the vertical force acting on the tire. The paper compares a previously studied model for calculating pneumatic scrub to a new model. The old model is:

$$P_s = F_y / K_L - R_L \tan\gamma, \tag{2.2}$$

Where P_s is the pneumatic scrub, F_y is the lateral force acting on the tire, K_L is the lateral stiffness of the tire, R_L is the static loaded radius of the tire, and γ is the tire camber angle. It is shown that this model can not be used to accurately describe the overturning moment behavior of a tire. The new model proposed is:

$$P_s = F_y / K_L - R_L \tan\gamma - P_r, \tag{2.3}$$

where P_r is called the residual pneumatic scrub. It is found that the residual pneumatic scrub plotted against slip angle displays the same shape as lateral force vs. slip angle. Therefore, the Magic Formula definition used for lateral force is also used to describe the residual pneumatic scrub. This model is discussed in further detail in Chapter 5.

In [7] the author examines the use of a scaling factor extension to the Magic Formula proposed in [3]. The purpose of the scaling factors is to extend the Magic Formula tire model developed on a rolling road to different driving surfaces. In this model, each of the main coefficients from equation (2.1) are multiplied by a scaling factor. The author hypothesized that the scaling factors are not tire dependent but rather surface dependent. That is, that the same set of scaling factors can be used to scale any Magic Formula tire model to that particular surface. The research found that this hypothesis was primarily true.

In the case of rolling road testing, the scaling factors are all equal to unity. Force and moment data is then collected for five different tires on dry asphalt, wet asphalt, ice, and snow. The scaling factors in the MF are then determined using a minimization approach. Statistical analysis is performed on the scaling factors to determine if a set of scaling factors can accurately describe a driving surface. It was found that dispersion of scaling factors for the five tires was very small in most cases. The influence of the road on the scaling factors is mostly seen peak value factor (the scaling factor for D) and the stiffness factor (the scaling factor for $K = B \times C \times D$).

Steady state and transient vehicle tests were also performed to assess the validity of the scaling factors in the overall vehicle model. In both high and low friction cases, the inclusion of

scaling factors in the vehicle model provides a good description of the vehicle's steady state behavior. The scaling factors also improve the estimation of lateral acceleration and yaw rate during transient maneuvers.

In [8] and [9] the use of the Magic Formula tire model in vehicle dynamics studies is investigated. It was shown that the MF can accurately model a tire from measured data. The MF is also able to model ply steer and conicity effects.

Transient tire models have been discussed in [2], [10], [11], [12], [13], [14], [15], and [16]. It is shown that lateral force transient response to slip angle can be modeled accurately as a first order relationship.

2.2: Review of Vehicle Rollover Literature

In [17] the physics of automobile rollover are studied. The simplest way of analyzing a vehicle's propensity to roll over is through the use of the static stability factor (SSF). The SSF is defined as:

$$SSF = \frac{t_w}{2h_{CG}}, \tag{2.4}$$

where t_w is the vehicle track width and h_{CG} is the distance from the ground to the center of gravity (CG) of the sprung mass. The SSF can also be considered the lateral acceleration in g's required to begin vehicle rollover when the vehicle is represented by a rigid body with no deflections in suspension or tires. This can be seen by resolving the acceleration vectors acting at the vehicle center of gravity.

The author then considers two categories of rollover. First, when the vehicle is moving laterally and runs into obstacle and the vehicle pivots about the two tires that struck the obstacle. This is also called tripped rollover. The second case is when a vehicle is moving in a circular path. A centripetal force between the tires and road forces the vehicle around the curve. The centripetal acceleration acts at the CG of the sprung mass, which causes a centrifugal force in the opposite direction at the body CG. This force can cause vehicle rollover called un-tripped rollover.

A way of classifying vehicle rollover safety for the tripped case is through the use of vehicle critical speed. First, the critical point of the vehicle is defined as the point where a vehicle will roll over if there is any lateral velocity when the vehicle is pivoting about two tires (either front left and rear left or front right and rear right) by some object, such as a curb. Critical speed is then defined as the initial lateral speed at which a vehicle can collide with an object laterally and reach its critical point. Therefore, if a vehicle strikes an object laterally while moving at a lateral speed higher than the critical speed, the vehicle is expected to roll over. Critical speed can be calculated by:

$$v = \left[2g\left(\sqrt{\left(\frac{t_w}{2}\right)^2 + h_{CG}^2} - h_{CG} \right) \right]^{1/2} \tag{2.5}$$

The author believes that critical speed is a more accurate representation of vehicle rollover tendency than SSF. However, critical speed is only valid for tripped rollovers in which the vehicle is moving laterally and hits an obstacle. SSF and critical speed are both reasonably accurate indicators of vehicle rollover tendency; however, they are not completely accurate because they do not take into account any vehicle stability control systems.

In [18] several methods for detecting vehicle rollover were tested. The purpose of the tests was to find a method for detecting impending vehicle rollover that will activate active chassis subsystems when needed and minimize unnecessary activations of the chassis control systems. First, estimates obtained from the use of single sensors were examined. A lateral acceleration sensor, roll rate sensor, and suspension relative position sensor were all used to obtain estimates of the vehicle roll angle.

For the lateral acceleration sensor, the following equation was used to determine roll angle:

$$\phi = -\left(M_s h_{roll} / k_{roll}\right) a_{ym}, \tag{2.6}$$

where ϕ is the body roll angle, M_s is the vehicle sprung mass, h_{roll} is the distance between the roll axis and sprung mass center of gravity, and a_{ym} is the lateral acceleration measured by the sensor. This method provides good estimation of the roll angle at low angles during cornering on smooth roads. Rough roads and high angles cause poor estimates.

The roll rate sensor integrates the measured roll rate by passing it through a low-pass filter with transfer function $1/(s+a)$ to obtain an estimate of the roll angle. The purpose of the low pass filter is to get rid of sensor bias since pure integration is sensitive to sensor bias. Since the roll rate sensor measures the vehicle absolute roll rate rather than the angular rate with respect to the road, banks in the road are included in the measured roll rate. Changes in the bank of the road are typically slow with respect to changes in road roughness. Therefore, the bank angle can be estimated by taking the roll rate measured from the sensor and subtracting the measured value from a lateral acceleration sensor and then passing this through a low pass filter.

This estimate of the bank angle effect is then subtracted from the measured roll rate to produce a centered value of the body roll rate. It was found that this method works well for determining the roll angle during quick changes in roll angle and also works well for both small and large angles. The disadvantages of this method are its sensitivity to sensor bias and poor ability to estimate the roll angle during steady state turns.

The author then proposes an observer based approach to determining the roll angle. The observer consists of a simple vehicle roll model. The observer subtracts its output from the roll angle estimates obtained from the sensor measurements which are then fed through a gain and then back into the observer. The gain matrix is adaptive and is able to change based on different driving situations to reflect the confidence of the measurements of each of the two sensors. The observer itself is also adaptive and changes based on the roll angle. The preliminary estimates of roll angle form the sensors are used to determine the operating condition of the observer. For low angle situations, the vehicle model is:

$$I_{xx1}\frac{d^2\phi}{dt^2} + c_{roll}\frac{d\phi}{dt} + k_{roll}\phi = -M_s a_{ym} h_{roll}, \tag{2.7}$$

where I_{xx1} is the moment of inertia of the vehicle body with respect to the roll axis. During two wheel lift off conditions, the model then becomes:

$$I_{xx2}\frac{d^2\phi}{dt^2} = -Ma_{ym}h - Mg(t_w/2)\cos\phi, \tag{2.8}$$

where I_{xx2} is the moment of inertia of the entire vehicle with respect to the axis of rotation, which runs through center of the contact patches of the outside tires. M is the total vehicle mass, and t_w is the track width.

A rollover index was proposed that is a function of measured lateral acceleration, measured and centered roll rate, and estimated roll angle. The index was then used in vehicle dynamics testing to show the validity of the observer-based predictor of roll index. Simulation and actual vehicle test results show that the proposed observer is a good estimator of roll angle for a wide range of maneuvers, and that the roll index is a good predictor of impending vehicle rollover. The rollover index operates independently of any other stability control systems that the vehicle may be equipped with, and may be used to activate an emergency subsystem.

In [19], the authors discuss algorithms for predicting vehicle rollover and the necessary selection of accompanying sensors. The authors state that the goal in designing a rollover sensing module (RSM) is to select a proper discrimination algorithm that will deploy a safety restraint when needed and have high immunity to non-rollover events. For example, an accelerometer is not able to tell the difference between acceleration due to gravity and acceleration due to inertial effects. Therefore, a robust discrimination algorithm is needed to allocate the measured acceleration appropriately.

An RSM usually consists of a primary discrimination path and a secondary arming path. The primary discrimination path consists of a set of sensors, such as angular rate sensors and accelerometers, which provide information to a micro-controller that makes the decision on whether or not safety restraints need to be deployed. The purpose of the secondary arming path is to prepare the system to trigger desired actions in the case of anticipated rollover and to prevent undesired triggering in the case of faults in the primary path. An example of undesired triggering is a brake torque applied by the control algorithm in an attempt to stabilize the yaw moment of the vehicle when it is not needed. The application of the brakes in an unnecessary

situation can alter the driver's desired path of travel without significantly improving the stability of the vehicle.

The proposed RSM was tested in a Simulink environment. Data was collected from real-world simulations and then fed into the RSM Simulink model to calibrate it. It was shown that the proposed method for a discrimination and deployment algorithm produces an RSM that meets the requirements for deployment time to fire and requirements for no trigger situations.

In [20] the authors investigate the claim proposed by the National Highway Traffic Safety Administration (NHTSA) that the static stability factor (SSF) of a vehicle is the primary indicator of a vehicle's lateral stability. The authors propose a worst-case methodology and compare it to the SSF as a predictor for a vehicle's propensity to roll over. The worst-case methodology seeks to find the values of the inputs (vehicle speed, steering wheel angle, and surface friction) that produce a worst case-scenario for vehicle rollover. This worst case scenario will be different for every vehicle. The worst case scenario is determined by using an iterative algorithm along with the vehicle model. The worse case scenario is then simulated in a vehicle simulation environment using software such as CarSim and TruckSim.

By comparing the worst-case methodology to the SSF of the vehicle, it was shown that the SSF is not a sufficient indicator of a vehicle's lateral stability. One of the reasons is that SSF does not take into account any onboard control systems, specifically vehicle stability control (VSC), which can greatly improve the lateral stability of a vehicle. It was shown that a sport utility vehicle (SUV) with a lower SSF and equipped with VSC can have a higher resistance to rollover than a vehicle with a higher SSF that is not equipped with VSC. This research shows

the importance of including lateral stability control systems when rollover mitigation is desired and not simply relying on favorable geometry of the vehicle.

In [21], the author investigates the sustained roll, heave, and yaw oscillations that occur during the steady state portion of a fishhook maneuver. In a fishhook maneuver, the steering wheel is first steered rapidly in the positive direction and then immediately steered in the negative direction and then held constant at some high magnitude steer angle. During the constant steer angle the vehicle enters the steady state portion of its maneuver. The phenomenon of the sustained roll, heave, and yaw oscillations during the steady state portion of the maneuver has been accredited to the coupling of the roll, heave, and yaw modes. Body roll and heave are coupled due to jacking in the suspension links. As the body moves up and down, vertical loads on the tires oscillate and therefore cause the lateral forces on the tires to oscillate. This oscillation of lateral force directly effects the vehicle roll and yaw response.

The effect of changing vehicle parameters on vehicle stability was studied. In particular, it was found that raising the roll center heights increases the suspension jacking forces, which is the primary cause for roll and heave coupling. As a result, raising the roll center heights causes instability. Non-linear, progressive spring stiffness also causes instability as it gives rise to additional suspension jacking forces. It was also shown that increasing suspension damping will help vehicle stability, but is a tradeoff when ride comfort is desired.

2.3: Review of Vehicle Yaw Control and Rollover Control Literature

In [22], the author develops a new control algorithm for vehicle stability. The control algorithm is based on Lyapunov direct method. Adaptation laws are included in the algorithm to allow for estimation of unknown vehicle parameters. The following candidate Lyapunov function is proposed:

$$V(x,p,t)=\frac{1}{2}\left[\tilde{x}^T A\tilde{x}+\tilde{p}^T\Gamma\tilde{p}\right]+\int\left(\tilde{x}^T B\tilde{x}\right)dt\,, \tag{2.9}$$

where x is the state vector, p is a vehicle parameter vector, Γ is the adaptation gain matrix, and A and B are matrices that contain coefficients for two degree of freedom equations of motion. The two degrees of freedom considered are vehicle lateral speed and yaw rate. The ~ denotes an error vector, which is the difference between the actual value and the desired value.

Local asymptotic stability is guaranteed for the system when the control law and adaptation law are chosen such that $V(x,p,t)$ is positive definite and $\dot{V}(x,p,t)$ is negative definite. The control law and adaptation laws are developed to insure that these two conditions hold. The control law has the form:

$$U = A\dot{x}_d + Bx_d + C - D\tilde{x}\,, \tag{2.10}$$

where A, B, and C are matrices containing coefficients from the vehicle equations of motion, x_d is a vector containing the desired values, and D is the control gain matrix. $U = [U_v \;\; U_r]^{\mathrm{T}}$ where U_v and U_r are the force and moment required to stabilize the vehicle lateral velocity and yaw moment, respectively. The control force and moment can be generated using anti-lock brakes or active steering. The author tested the control algorithm an 8 degree of freedom vehicle model. It

was shown that this control algorithm causes the vehicle to maintain a yaw rate close to the desired stable yaw rate.

In [23], the author proposes implementation of the control algorithm developed in [22]. The author proposes a direct yaw control (DYC) method using a differential braking strategy to generate the desired corrective yaw moment. The author also uses active front steering (AFS) to generate the desired lateral force for vehicle stability. Front and rear axle tire cornering stiffness is used as the adaptation parameter (p in equation (2.9)) to enhance controller robustness for use on a variety of driving surfaces. The control algorithm is developed the same way as in [22].

The proposed differential braking strategy for generating the corrective yaw moment U_r is shown in Table 2-1. The actual vehicle yaw moment in r and the desired vehicle yaw moment is r_d.

Table 2-1. Braking strategy for generating corrective yaw moment

r_d	$r - r_d$	U_r	**Braked wheel**
+	+	+	None
+	+	-	Front Left
+	-	+	Rear Right
+	-	-	None
-	+	+	None
-	+	-	Rear Left
-	-	+	Front Right
-	-	-	None

With positive moment meaning the vehicle is rotating clockwise from a bird's eye view of the vehicle, the interpretation of Table 2-1 is as follows: if the vehicle is supposed to be rotating to the right, but is rotating to the right more than it should, and the calculated corrective

moment will cause the vehicle to rotate to the right less, then a brake torque is applied to the front left wheel. If the vehicle is supposed to be rotating to the right, but is not rotating to the right as much as it should, and the calculated corrective moment will cause the vehicle to rotate to the right, then a brake torque is applied to the rear right wheel. Conditions for braking the rear left and front right wheels can be obtained by using this same logic. If none of the above conditions are met, then no wheel is braked. If a wheel is selected to be braked, then the desired brake torque to be applied to that wheel is:

$$T_b = \frac{2R_s}{t_w} U_r \tag{2.11}$$

where T_b is the desired brake torque, R_s is the tire static loaded radius, and t_w is the vehicle track width.

This control algorithm was implemented into an 8-DOF vehicle model that includes a combined slip tire model and a single-point preview driver model. From the simulations it was shown that the control algorithm can significantly improve vehicle stability during emergency maneuvers. It was also shown that the control algorithm is robust and is functional for a wide range of driving surfaces with different values of friction coefficient.

In [24], the author develops a control algorithm that implements active front steering and braking to achieve vehicle roll stability. The algorithm consists of three control loops: one for continuous steer control, one for emergency steer control, and one for emergency brake control. The continuous steer control loop uses sensor feedback of body roll rate and body roll acceleration to determine the front steer angle to be added or subtracted from the driver steer input.

The emergency steer control and emergency brake control are activated based on the value of a roll coefficient. The roll coefficient is determined by the formula:

$$R = \frac{F_{z,R} - F_{z,L}}{F_{z,R} + F_{z,L}}, \tag{2.12}$$

where $F_{z,R}$ is the combined vertical load on the front right and rear right tires and $F_{z,L}$ is the combined vertical load on the front left and rear left tires. When $F_{z,R} = 0$, the right side of the vehicle will experience two-wheel lift-off (TWLO) and the roll coefficient will be R = -1. When $F_{z,L} = 0$, the left side of the vehicle will experience TWLO and the roll coefficient will be $R = 1$. When there is equal load on the left and right side of the vehicle the roll coefficient will be zero. The roll coefficient can further be approximated by:

$$R \approx \left(\frac{2h_{CG}}{t_w} \right) \left(\frac{a_{y,s}}{g} \right) \tag{2.13}$$

where h_{CG} is the distance from the ground to the center of gravity (CG) of the sprung mass, t_w is the track width, $a_{y,s}$ is the lateral acceleration of the sprung mass, and g is the acceleration due to gravity.

Since $|R| = 1$ is the criteria for TWLO, the roll coefficient is a good indicator of an emergency roll situation. It was shown that steering and braking control based on rollover coefficient can significantly improve vehicle roll stability. One of the drawbacks of using active front steering is that it causes the vehicle to change its desired course. The course deviation is, however, reduced by concurrence of emergency braking which causes the vehicle to decelerate.

2.4: Conclusions

From the review of literature the following conclusions have been made about tire models:

- A semi-empirical tire model called the Magic Formula exists that will provide accurate force and moment vs. slip characteristics for a tire
- The Magic Formula can be used if the tire is tested over a wide range of forward speeds, slip angles, camber angles, and vertical loads
- A scaling factor extension can be included in the Magic Formula to account for terrain effects
- Scaling factors are primarily surface dependent, and for the most part, remain independent of tire type, vehicle type, or vehicle speed
- Scaling factor effects show up mostly in the scaling of the peak value and stiffness

From the literature, the following conclusions have been drawn about vehicle rollover:

- SSF and vehicle critical speed generally give a good description of vehicle rollover tendency, however, they do not take into account the effects of vehicle stability control systems
- A rollover index that is a function of vehicle lateral acceleration, roll rate, and roll angle is a good indicator of impending vehicle rollover

- Compared to SSF, a more accurate way of determining vehicle rollover propensity is through vehicle simulation of worst-case scenarios

- A vehicle with a lower SSF and equipped with vehicle stability control can have significantly better roll stability than a vehicle with a higher SSF and no vehicle stability control

- Vehicle yaw, roll, and heave responses are coupled, primarily through suspension links

- Yaw instability can cause skidding, which increases the risk of tripped rollover

- Yaw instability can cause increased lateral acceleration, which increases the risk of un-tripped rollover

From the literature, the following conclusions have been drawn about vehicle stability control:

- A control algorithm based on Lyapunov direct method can significantly improve vehicle yaw stability

- This control algorithm can be implemented in a vehicle using stock architecture, including braking and steering

- A roll coefficient that is function of vehicle track width, sprung mass CG height, and vehicle lateral acceleration is a good indicator of impending vehicle rollover

- This roll coefficient can be used to implement emergency roll control strategies that can help vehicle roll stability

Chapter 3: Tire Testing and Modeling

An accurate tire model is of absolute importance in developing an accurate vehicle model. The major functions of a tire include handling/ steering, traction, braking, and ride. Each of these functions plays a primary role in vehicle performance. Extensive tests must be performed in order to obtain all of the necessary information to properly characterize a tire for vehicle dynamics studies.

This chapter begins with a discussion of the studied tire, which includes nomenclature and terminology that is relevant to developing the tire model. Next, the rolling road testing that was used to form the baseline force and moment tire model will be discussed. The chapter will conclude with a discussion of the collected data and the processing that is involved to prepare it to be used in the tire model generating software that will be presented in chapter 5.

3.1: Studied Tire

The studied tire has radial plies and is 49.5 inches in diameter. Its free section width is 15.1 inches and its loaded section width is 16.8 inches. The rated load of the tire is 7200 lbs. It has an off-road tread pattern that consists of thick lugs with a depth of 0.92 inches. The tread pattern is shown in Figure 3.1.

Figure 3.1. Tread pattern of studied tire

The tire is mounted on a 20 inch wheel with 10 bolt holes. The wheel has a tire inflation valve that works with the central tire inflation system that automatically inflates and deflates the tire for improved performance on different driving surfaces. The tire typically operates with an inflation pressure between 65 psi and 110 psi.

3.1.1: Nomenclature and Sign Conventions

This section includes a discussion of the nomenclature and sign conventions that will be used in tire testing and modeling for the remainder of this paper. Figure 3.2 shows relevant variables for tire characterization for vehicle rollover studies. These sign conventions are to be strictly observed for all tire modeling in this paper.

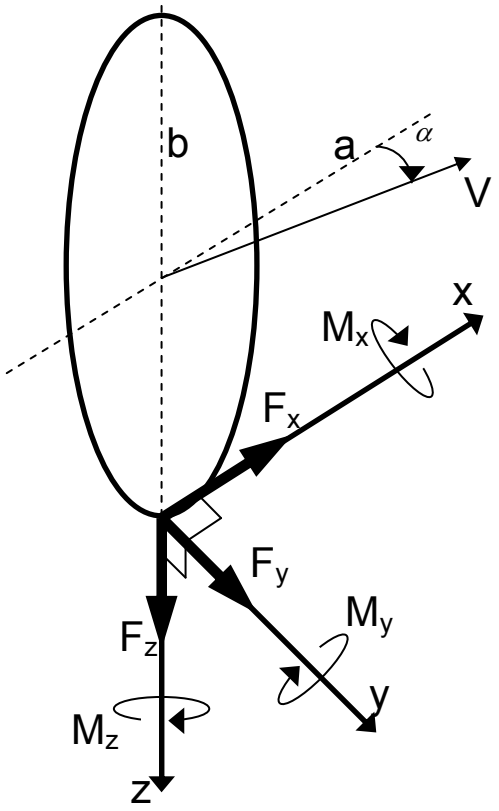

Figure 3.2. Forces and moments acting on tire from driving surface

The tire contact patch is defined as the area of tread on the tire that is contacting the driving surface. In figure 3.2, line *a* and *b* intersect at the geometric center of the wheel. The origin of the tire coordinate axis is the projection of the intersection of *a* and *b* onto the tire contact patch plane. The x-axis runs parallel to *a* and is defined to be positive in the direction of forward motion of the vehicle. The z-axis is collinear with *b* and is positive in the downward direction. The y-axis forms a right angle with both the x-axis and z-axis and is positive to the right when looking at the tire from the rear.

The force F_x acting on the tire is called the longitudinal force and is positive along the positive x-axis. The force F_y acting on the tire is called the lateral force and is positive along the positive y-axis. The force F_z acting on the tire is called the vertical force or vertical load and is

positive along the positive z-axis. The moment M_x acting on the tire is called the overturning moment and is positive rotating clockwise about the x-axis when looking down the length of the x-axis from the origin. The moment M_y acting on the tire is called the rolling resistance moment and is positive rotating counterclockwise about the y-axis when looking down the length of the y-axis from the origin. The moment M_z acting on the tire is called the aligning moment and is positive rotating clockwise about the z-axis when looking down the length of the z-axis from the origin.

The angle α is called the slip angle, and is the angle between the direction the tire is heading, a, and the direction of the tire velocity vector, V. Slip angle is defined as positive when V is rotated in a clockwise direction from a when looking at the tire from above. Slip angle will be discussed in greater detail in the next section.

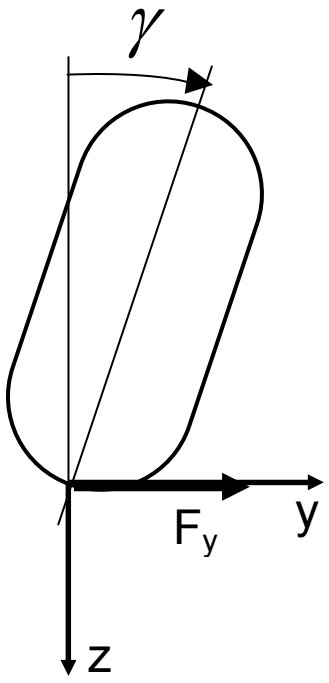

Figure 3.3. Camber angle of tire, viewed from the rear

Figure 3.3 defines the camber angle of a tire. Camber angle, γ, is the angle between the negative z-axis and the wheel center plane. Camber angle is positive when the wheel center plain is rotated in a clockwise direction from the negative z-axis when viewing the tire from the rear. According to the sign convention used, a positive camber angle will produce a positive lateral force. Camber angle is discussed in greater detail in section 3.1.3.

3.1.2: The Effect of Slip Angle on Tire Forces and Moments

The presence of slip angle will cause force and moment interactions between the tire and driving surface due to tread deflections in the tire contact patch. The effect of slip angle on tread deflection can be illustrated by a simple figure showing the deflection path of a tread element as it travels through the contact patch.

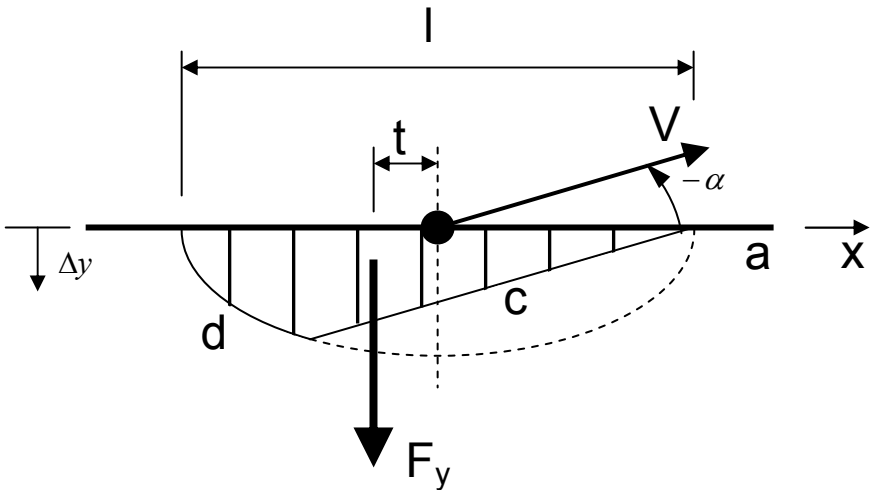

Figure 3.4. Tread center line deflection in tire contact patch resulting from slip angle

Figure 3.4 shows a diagram of tread center line deflection in the contact patch as a result of slip angle. As the tire rotates, a tread element along the center line of the tire, *a,* will enter the

contact patch at the right side of the figure. It will then travel along the straight line *c,* along the curved line *d,* and then exit the contact patch on the left side along the tire center line, *a.* The semi-oval represents the maximum deflection due to friction limitations for a tread element entering the contact patch at the center line. When a tread element first enters the contact patch, it will travel along the straight line *c*, which is called the adhesion region. The line *c* is parallel to the tire velocity vector, *V*. When the tread element intersects the maximum deflection oval, the friction force between the tread element and driving surface is no longer able to force the tread element along the straight line *c*. The tread element then brakes free from the adhesion region and follows the remainder of the path of the maximum deflection oval, the line *d*. This is called the slip region. After the tread element travels along line *d*, it leaves the contact patch on the left side of the figure along the center line of the tire.

At each location along the deflection trajectory the driving surface will exert a force, f_y, on the tire proportional to the lateral deflection of the tread element, Δy. The proportionality constant between force and deflection is the tire lateral stiffness, K_y. This is shown in equation (3.1).

$$f_y = \Delta y \cdot K_y \tag{3.1}$$

Defining the function

$$f_y(x) = \delta_y(x) \cdot K_y, \tag{3.2}$$

where $\delta_y(x)$ is the value of Δy at each location x along the contact patch, we can integrate over the length of the contact patch to get the total lateral force, F_y.

$$F_y = \int_0^l f_y(x)dx = \int_0^l (\delta_y(x) \cdot K_y)dx \tag{3.3}$$

In figure 3.4 it can be seen that the lateral force, F_y, will be positive when the slip angle, α, is negative, which adheres to the sign convention in section 3.1.1.

The lateral force will act at the centroid of the area enclosed by lines *a*, *c*, and *d* of figure 3.4. Therefore, the lateral force will act on the contact patch a distance of *t* behind the center point of the wheel. The distance *t* is called pneumatic trail, and is the variable responsible for generating the aligning moment, M_z. This is defined by the equation:

$$M_z = F_y \cdot t \tag{3.4}$$

Torque about the z-axis can also arise from mechanical trail due to caster angle and offset of the kingpin axis. For all tire testing, it is assumed that the caster angle is zero degrees and there is no kingpin offset, so torque due to mechanical trail can be ignored.

Figure 3.5 shows the cause of overturning moment, M_x. When the acting center of the vertical force shifts laterally, the vertical load causes a moment about the longitudinal axis. The lateral shift is called pneumatic scrub, P_s. Overturning moment is then modeled by the equation

$$M_x = F_z \cdot P_s \tag{3.5}$$

Overturning moment is heavily dependent on slip angle because the value of P_s is a function of, amongst many other things, slip angle.

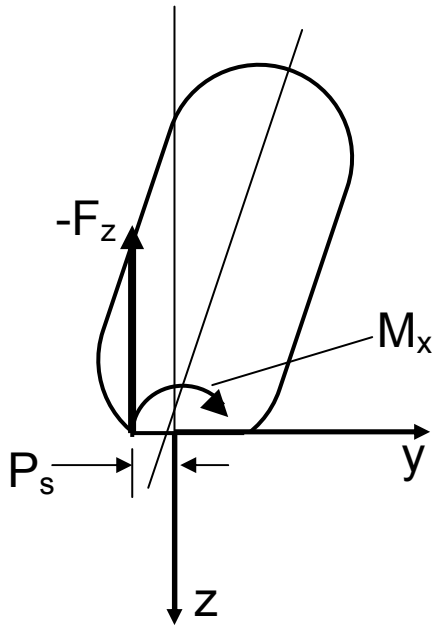

Figure 3.5. Lateral shift in acting point of F_z causes M_x

Figure 3.6 shows sample plots of the general shape of the curves for lateral force, aligning moment, and overturning moment vs. slip angle. The slope at the origin of the lateral force vs. slip angle plot is called the cornering stiffness, $C_{F_y\alpha}$. The slope at the origin of the aligning moment vs. slip angle plot is called the aligning stiffness, $C_{M_z\alpha}$. The slope at the origin of the overturning moment vs. slip angle plot is called the overturning stiffness, $C_{M_x\alpha}$.

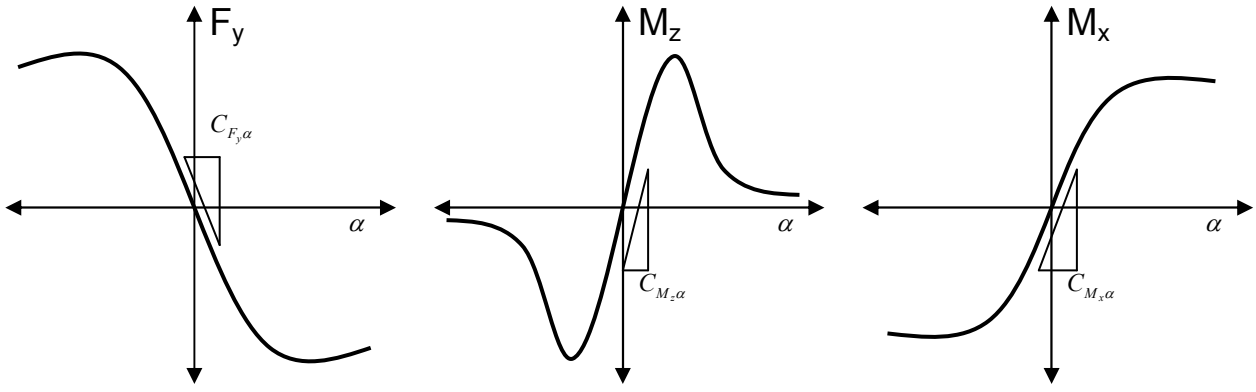

Figure 3.6. Typical shapes for lateral force, aligning, and overturning moment vs. slip angle

3.1.3: The Effect of Camber Angle on Tire Forces and Moments

The lateral force that results from a cambered tire is called camber thrust. The camber thrust characteristics of a tire play an important roll in the vehicle behavior in near rollover situations. Figure 3.7 shows a diagram of the camber thrust that acts on the tire from the tire being cambered due to an inclined surface. This is different from figure 3.3, which shows a tire cambered due to vehicle roll. The incline of the surface, γ, in figure 3.7 is the same as the camber angle of the tire. When a tire is driven on an inclined surface there is also a lateral force due to vertical load acting on the tire in the direction opposite that of camber thrust, F_W.

The camber stiffness of a tire, $C_{F\gamma}$, is defined as the slope of the lateral force vs. camber angle curve at the origin. The camber coefficient is defined as $C_{F\gamma} / F_z$. The camber coefficient is the determining factor is whether or not a tire will climb up the incline or fall down the incline. If $C_{F\gamma} / F_z > 0.0175$ N/N/deg then the camber thrust will be greater than the lateral force due to the weight of the vehicle and the tire will climb up the incline. If $C_{F\gamma} / F_z < 0.0175$ N/N/deg then the camber thrust will be less than the lateral force due to the weight of the vehicle and the tire will slide down the incline.

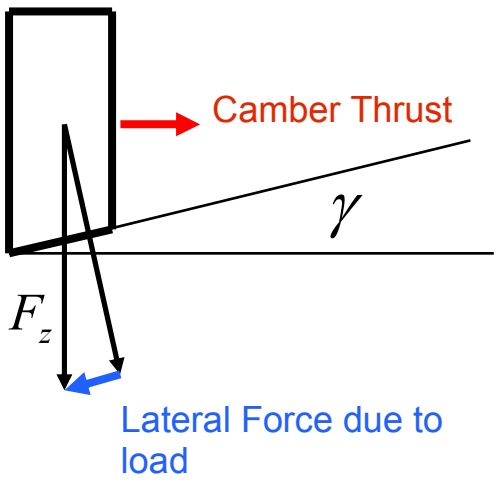

Figure 3.7. Camber thrust acting on tire due to inclined surface

3.2: Description of Facilities and Rolling Road Tire Test Rig

Tests were performed on the studied tire in order to model the tire for proper prediction of force and moment response due to slip angle, camber angle, and vertical load. These tests were carried out at the Landing Gear Test Facility at Wright Patterson Air Force Base (WPAFB) in Dayton, Ohio. Figure 3.8 shows the test rig with the studied tire mounted. The carriage that holds the tire is hydraulically actuated. The carriage presses the tire against a stainless steel flywheel to apply a vertical load. The flywheel rotates to give the tire a forward speed. The entire carriage rotates left and right to apply a camber angle to the tire. The front part of the carriage rotates clockwise and counterclockwise to apply a slip angle to the tire.

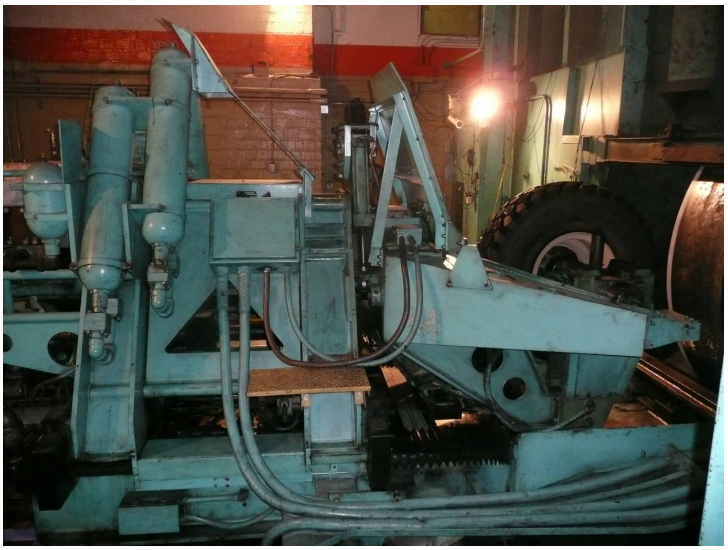

Figure 3.8. WPAFB tire test rig with studied tire mounted

3.3: Discussion of Experimental Procedure

Tests were performed over a wide range of slip angles, camber angles, speeds, and vertical loads to collect force and moment data. The tire was tested at seven different vertical

loads: 7200 lbs, 7650 lbs, 9000 lbs, 10800 lbs, 12600 lbs, 14400 lbs, and 15300 lbs. The tire was tested at four different flywheel speeds: 5 mph, 20 mph, 40 mph, and 65 mph. At each combination of vertical load and speed, a slip angle sweep and a camber angle sweep was performed. The slip angle sweep was one period of a sine wave with amplitude of 20 degrees slip angle and frequency of 0.033 Hz. The camber angle sweep was one period of a sine wave with amplitude of 16 degrees camber angle and frequency of 0.033 Hz. When a slip angle sweep was performed the camber angle was held at a constant 0 degrees, and when a camber angle sweep was performed the slip angle was held at a constant 0 degrees. Table 3-1 shows a table of the test matrix.

Table 3-1. Test matrix for studied tire testing

		Speed, Test #							
		5 mph		20 mph		40 mph		65 mph	
		Test 1	Test 2	Test 3	Test 4	Test 5	Test 6	Test 7	Test 8
	run #	Camber	Slip	Camber	Slip	Camber	Slip	Camber	Slip
Load,lbs	7200	1	8	15	22	29	36	43	50
	7650	2	9	16	23	30	37	44	51
	9000	3	10	17	24	31	38	45	52
	10800	4	11	18	25	32	39	46	53
	12600	5	12	19	26	33	40	47	54
	14400	6	13	20	27	34	41	48	55
	15300	7	14	21	28	35	42	49	56

The runs were grouped into eight sets of tests: at each speed a separate set of tests for both slip angle and camber angle sweeps. For each test, seven runs were performed which included the respective angle sweep for each of the seven vertical loads. During each test, data was continually collected for time, flywheel speed, slip angle, camber angle, vertical load, lateral force, longitudinal force, aligning moment, overturning moment, and rolling resistance moment.

Prior to each test a tire warm up was performed to get the tire to normal operating temperature for testing. The tire was warmed up by running it at 40 mph at the rated load (7200 lbs) for 10 miles. Before each test the tire inflation pressure was set at 71 psi. The inflation pressure was allowed to rise over the course of the test as the tire heated up. A two hour cool down was allowed after each test.

Four tires were provided, however, only one was needed for all 8 tests. Figure 3.9 shows the wear on the tread over the course of the tests. During testing, a thin layer of rubber would melt off and stick to the flywheel. As the speed increased, more rubber would melt off. However, not very much damage was done to the tire; therefore one tire was used for all tests.

Figure 3.9. Tread wear on studied tire. From left to right: post 20 mph, post 40 mph, post 65 mph

3.4: Discussion of Collected Data

The collected data was immediately filtered by the data acquisition software. This filtered out random fluctuations due to slight vertical load changes and electronic noise. The result was a characteristic curve containing a hysteresis loop for each force and moment vs. slip angle and camber angle. Figure 3.10, 3.11, and 3.12 show an example of the data. The hysteresis loop is present because of tire tread and carcass compliance and damping.

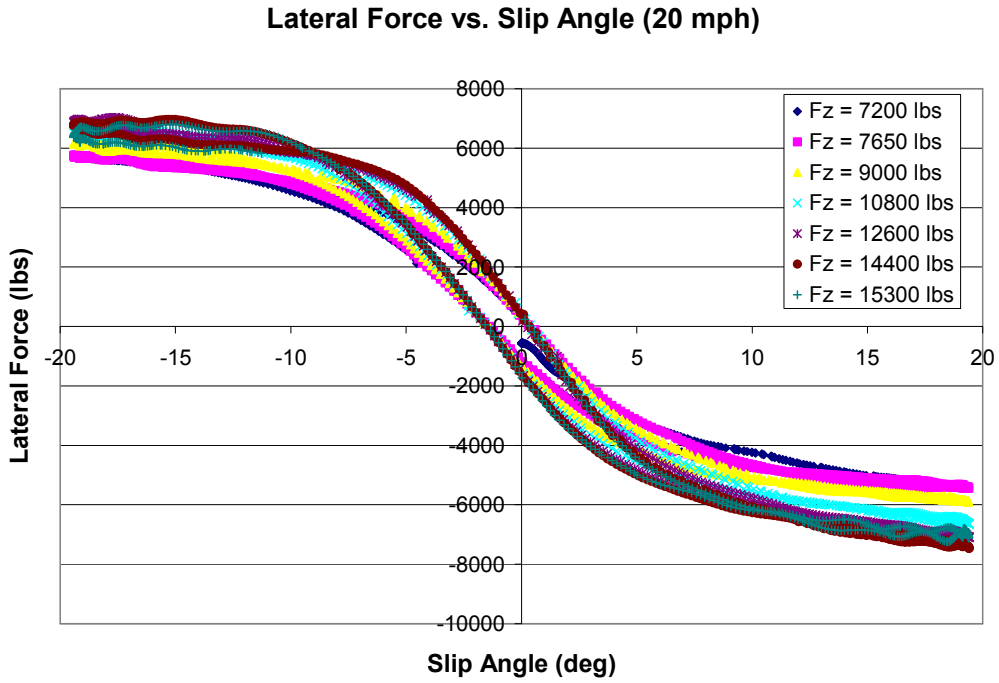

Figure 3.10. Lateral force vs. slip angle for 20 mph

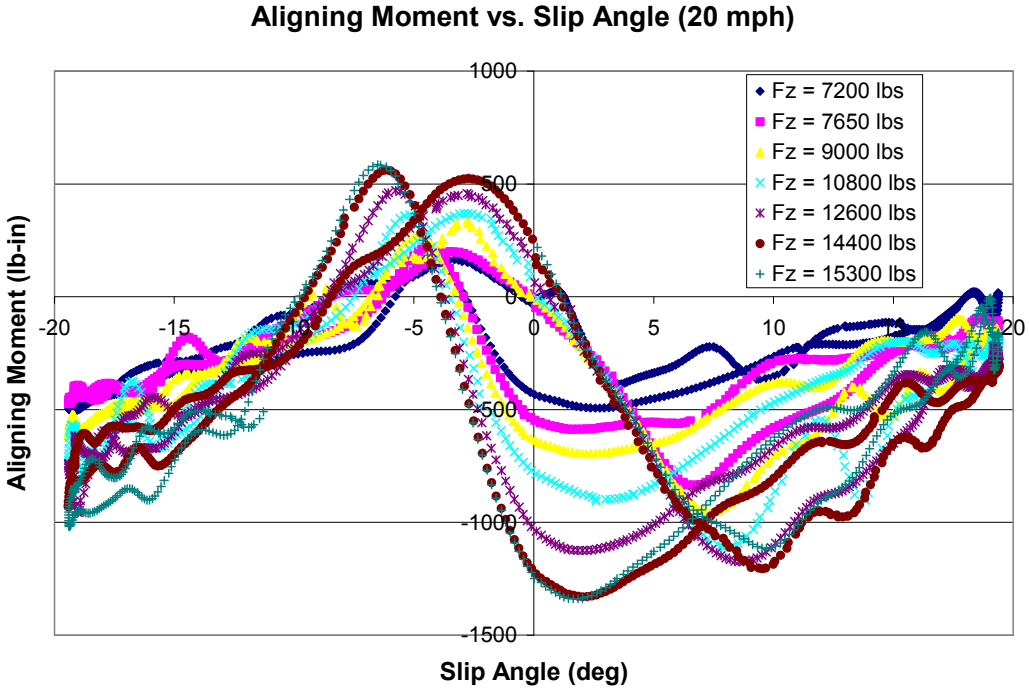

Figure 3.11. Aligning moment vs. slip angle for 20 mph

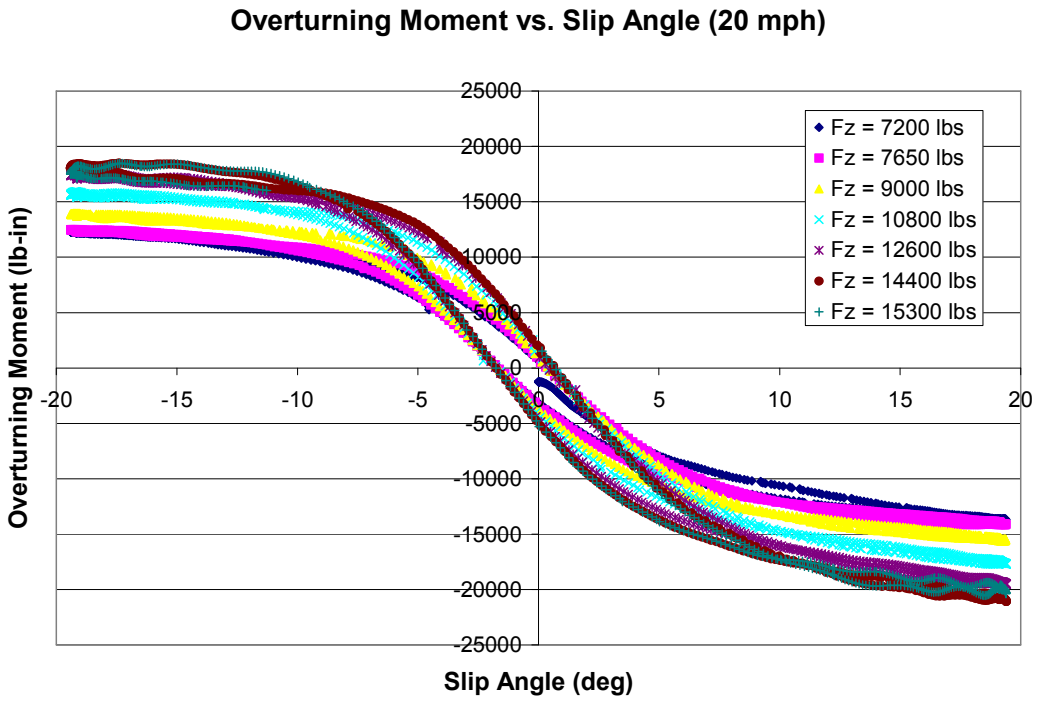

Figure 3.12. Overturning moment vs. slip angle for 20 mph

As the forward speed increased during testing, the data became noisier and thus less easy to model. All of the collected lateral force and overturning moment data was useable. However, only the 5 mph and 20 mph aligning moment data were useable. Figure 3.13 shows the aligning moment vs. slip angle raw data. At higher speeds, the amplitude of the tire vibrations became high. As a result, the vertical load fluctuations became high. Figure 3.14 shows that the vertical load fluctuations for the slip angle sweep at 40 mph and 7200 lbs vertical load varied between about 6900 lbs and 7400 lbs. Therefore, aligning moment data above 20 mph was not used in the tire modeling.

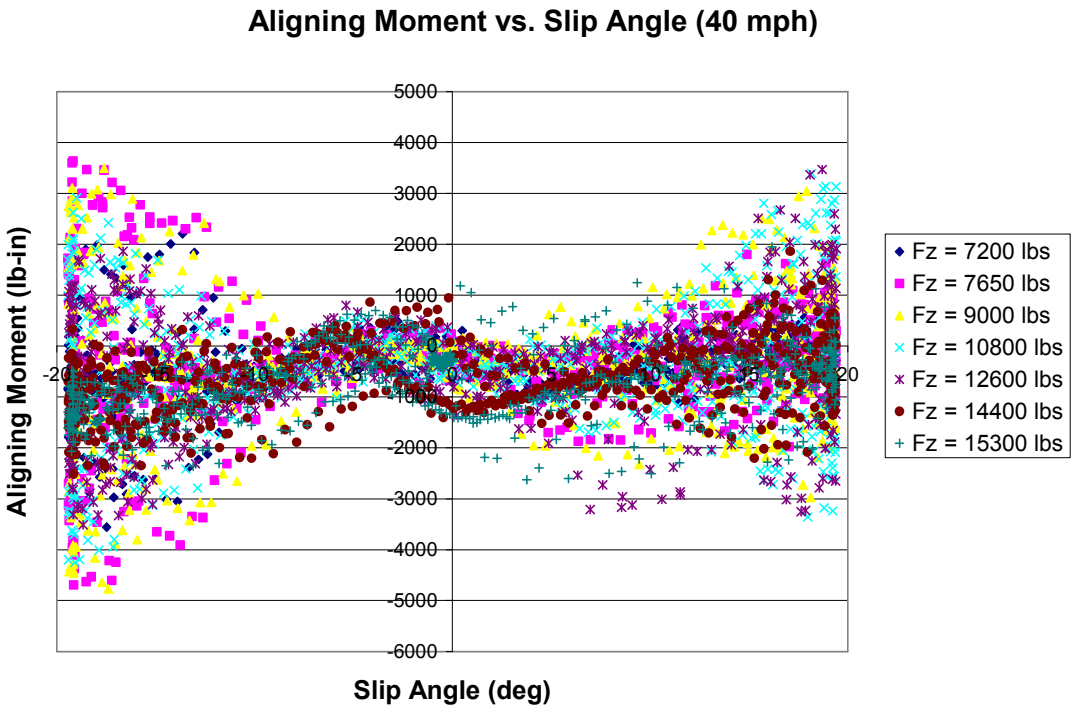

Figure 3.13. Aligning moment vs. slip angle for 40 mph

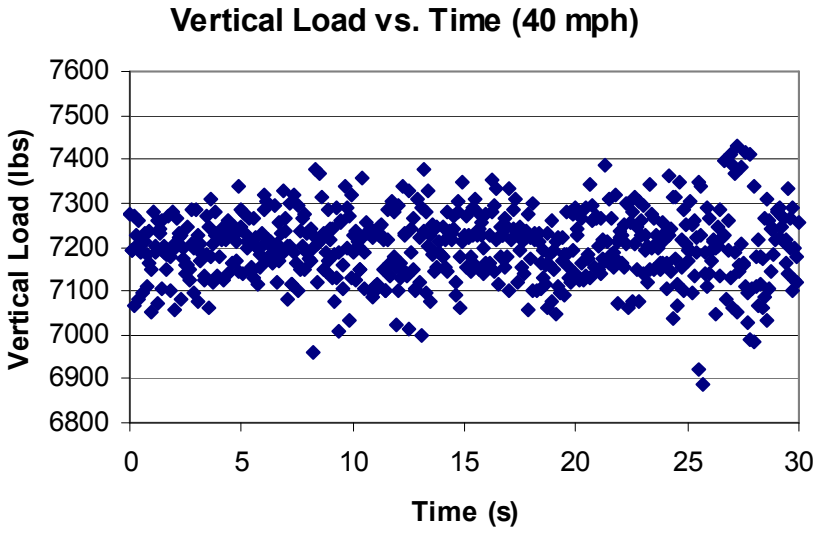

Figure 3.14. Vertical load vs. time for the 40 mph, 7200 lb vertical load run

3.5: Data Processing

Although the data was filtered as soon as it was acquired, additional processing had to be done to the data so that it was useable for a curve-fitting routine to model the tire. The data processing consisted of two steps: first smoothing the curve to get rid of force or moment fluctuations that rose from a natural frequency being excited, and second, averaging the hysteresis loop to produce a steady state curve. The model-fitting software discussed in Chapter 5 requires steady state data input, therefore the hysteresis loop must be transformed into a single steady-state curve before using the tire modeling software.

When the collected data is plotted vs. time, an interesting trend arises that does not show up when the force or moment is plotted vs. slip angle or camber angle. Figure 3.15 shows lateral force vs. time for a slip angle sweep at 65 mph and 10,800 lbs vertical load. As the lateral force increases in magnitude, the lateral force begins to oscillate at a frequency around 1.15 Hz. The first natural frequency of a tire is typically around 1.1 – 1.2 Hz, which explains why this occurs. The two regions of oscillation, which occur at high magnitude of positive or negative slip angle, can be smoothed by using a Fast Fourier Transform (FFT) filter. The FFT filter removes the oscillations and leaves a smooth curve. This leaves a smoothed curve, which is also shown in Fig. 3.15.

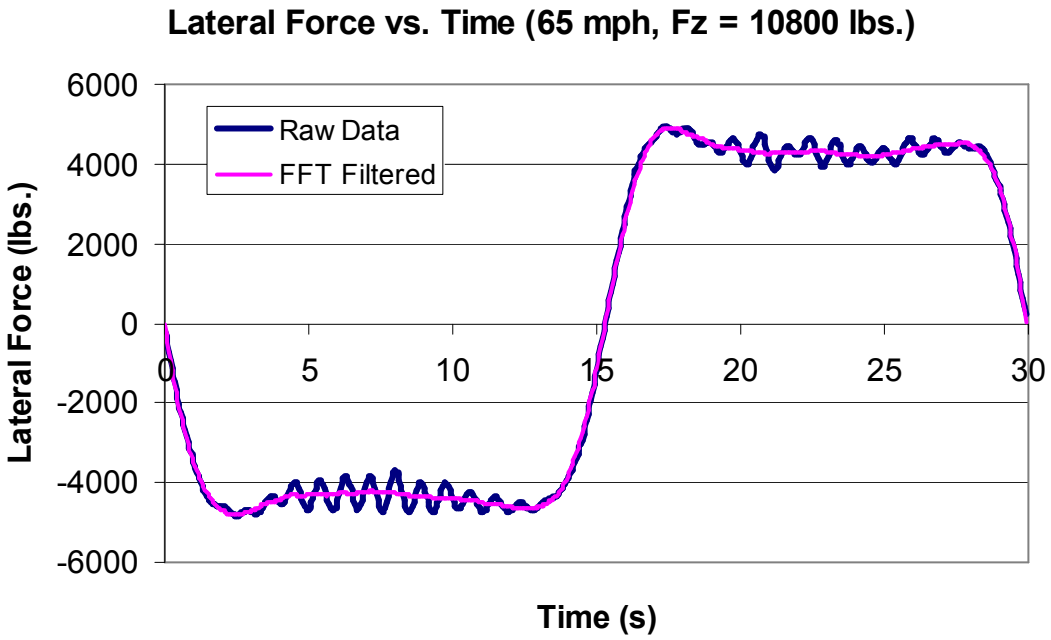

Figure 3.15. Lateral force vs. time for slip angle sweep at 65 mph, 10,800 lbs vertical load

After the oscillations are smoothed out using an FFT filter, a smoothed hysteresis loop exists. Since the tire model that is used is a steady state model, the hysteresis loop needs to become a solid curve that accurately represents the steady state response of the respective force or moment. For both the slip angle and camber angle sweeps, the sweep from positive to negative and the sweep from negative to positive exhibit the same lag, therefore it is a good assumption that averaging the hysteresis curve will produce a steady state curve. The data was averaged to transform the hysteresis loop into a steady state curve. Figure 3.16 shows the original data, FFT filtered data, and averaged data for a slip angle sweep at 65 mph and vertical load of 10,800 lbs. The data processing technique of smoothing out oscillations with an FFT filter and producing a steady state curve through data averaging was applied to all of the useable data to prepare it for the modeling program that is discussed in Chapter 5.

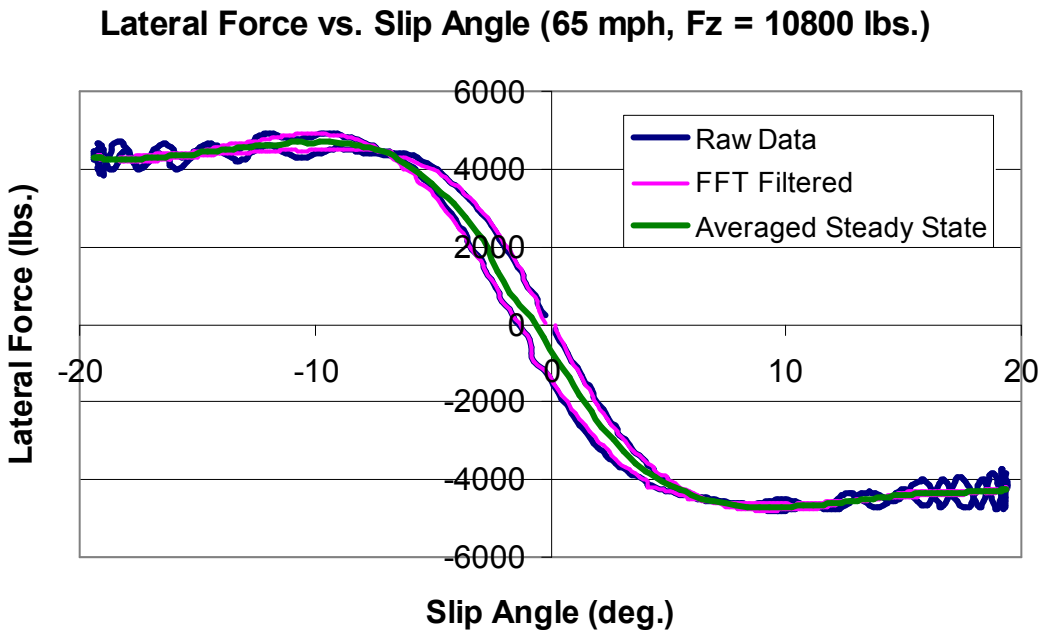

Figure 3.16. Raw data, FFT filtered data, and averaged steady state data for lateral force vs. slip angle at 65 mph, and vertical load of 10,800 lbs.

3.6: Conclusions

Because of recent fatalities in the studied vehicle due to vehicle rollover, force and moment testing was performed on the studied tire for use in vehicle dynamics studies and development of rollover mitigation strategies. The force and moment testing was carried out at Wright Patterson Air Force Base in Dayton, Ohio. A wide range of vertical loads, slip angles, camber angles, and forward speeds were applied to the tire. Forces and moments relevant to vehicle handling studies such as tire lateral force, aligning moment, and overturning moment were recorded. The data was processed to make it suitable for use in tire model fitting software, which is discussed in detail in Chapter 5.

Chapter 4: Off-Road Force and Moment Tire Testing

Tire force and moment testing is typically done on a rolling road. Chapter 3 included a discussion of the studied tire testing on a stainless steel flywheel. The information obtained from this testing is valuable for modeling the tire. The coefficient of friction between the tire and flywheel is representative of a typical tire/asphalt interaction. However, the studied vehicle will typically be driven on off-road surfaces such as dirt and gravel. Extensions must be made to the tire model to incorporate the effects of different driving surfaces.

Data acquisition and hardware control software was developed for an existing portable tire test rig to allow the rig to be operational for off-road tire testing [25]. The design and fabrication of the rig was primarily the work of another graduate student and can be found in [26]. The rig is capable of both dry and wet-road testing, as well as dirt, grass, and gravel. The rig records tire force and moment responses to various parameters such as forward speed, vertical load, slip angle, camber angle, and inflation pressure. The rig is able to accommodate a tire up to 44 inches in diameter. Since the studied tire is 49.5 inches in diameter, on- and off-road tests can be performed on smaller tires so that the general relationship between dry, on-road response and various off-road responses can be observed.

This chapter will first discuss the operation of the portable tire test rig, including the data acquisition and hardware control software. Next, the process of collecting data and an analysis of the collected data will be discussed. A sample set of collected data will be compared to an existing third party model to prove validation of the test trailer. Finally, off-road tire testing with the tire test rig will be discussed. The tire model extensions for the various surfaces will be discussed in Chapter 5.

4.1: Description of Portable Tire Test Rig

The design of the portable tire test rig was the work of another graduate student and can be found in [26]. The operation of the rig will be briefly explained in sections 4.1.1 – 4.1.3. The development of the data acquisition and hardware control software was the work of the current author and will be discussed in section 4.1.4.

The rig is housed in an 8 ft. x 32 ft. three-axle trailer. The three axles have a combined loading capacity of 13,000 lbs. The trailer is towed by a Ford F-350 crew cab dually. All of the hardware and software onboard the trailer is powered by a gasoline generator that sits in the bed of the truck. The generator supplies single-phase 120 V and 240 V power as well as three-phase 480 V power. This setup is shown in Figure 4.1.

Figure 4.1. Portable tire test rig towed by Ford F-350 with gasoline generator

The tire to be tested is mounted to a force and moment measurement hub that is connected to a steel load frame via control arms and a mounting plate. The load frame surrounds a 4 ft. x 8 ft. opening in the floor of the trailer which is located forward of the trailer axles. The

test tire accesses the driving surface through this opening. Figure 4.2 shows the rig setup where the tire is in contact with the driving surface.

Figure 4.2. Tire access to the driving surface

4.1.1: Tire Size Adjustment and Vertical Loading

Figure 4.2 shows the tire set up in the test rig. The tire is mounted to a force and moment measuring hub. The hub is supported by upper and lower control arms. The control arms are attached to a support plate with pillow block bearings. The support plate is able to move up and down a set of two vertical sliders that are mounted to the load frame inside the trailer. A screw actuator is able to move the support plate up and down the vertical sliders. Different tire sizes can be accounted for by raising the support plate, mounting the tire, and then lowering the support plate until the control arms are parallel with the driving surface.

An upside down L-shaped frame is welded to the support plate. A steel cage is mounted inside the L-frame. In between the top of the cage and the L-frame is an airspring that is responsible for applying the vertical load to the tire. The airspring is inflated with nitrogen to apply a vertical load of up to 10,000 lbs. A pressure regulator is placed in the plumbing to ensure that a relatively constant vertical load is applied to the tire throughout testing.

4.1.2: Tire Steering and Cambering

The steel cage that applies the vertical load to the tire also houses servo motors for steering and cambering the tire. Figure 4.3 shows the mechanism responsible for steering the tire. A steel fork is connected to the two sides of the force and moment measurement hub. The fork rotates to steer the tire. A servo motor sits inside of the cage above the tire to power the steer fork. The steer fork and servo motor are coupled to one another by a 153:1 planetary gear set. The rig is capable of doing steer sweeps of ± 20 degrees.

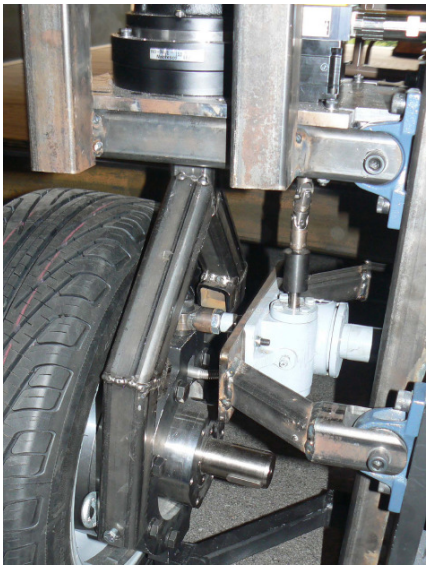

Figure 4.3. Steel fork responsible for steering the tire

On the upper control arm is a screw actuator that extends and retracts to camber the tire. Figure 4.3 shows this setup. The screw actuator is powered by a servo motor that is housed in the cage directly above the tire. The screw actuator and servo motor are coupled to one another by a series of universal joints. When the tire is cambered, the cage must also move up and down. Manual adjustments have to be made when cambering the tire, therefore the rig is currently capable of testing at discrete camber angles. The rig can accommodate camber angles between +10 degrees and – 5 degrees.

4.1.3: Wet-Road Testing

The trailer is equipped with a 500 gallon water tank with pump and spray nozzles to make the rig suitable for wet-road testing. Seven brass nozzles are mounted beneath the trailer in front of the rig. The nozzles spray water straight down in front of the tire to produce a layer of water up to 5 mm thick.

4.1.4: Hardware and Software for Data Collection and Control

A LabView Virtual Instrument (VI) was developed for the purpose of controlling the test rig hardware and collecting data. The VI runs on a laptop that sits inside the trailer. The VI interfaces with all of the necessary hardware via a National Instrument Data Acquisition (NI-DAQ) board. The NI-DAQ board is connected to the measurement hub to record force and moment measurements. Three forces (longitudinal, lateral and vertical) and three moments (aligning, overturning, and rolling resistance) are measured and recorded for the duration of the test. The NI-DAQ board also receives position feedback from the steer servo motor to record the steer angle of the tire. The NI-DAQ board receives feedback signals from the airspring pressure

regulator and the steer servo motor so that the VI can compute the necessary control signals and then supply them to the hardware via the NI-DAQ board. The developed VI front panel allows the user to input the desired steer angle sweep, including maximum angle and sweep frequency. The front panel of the VI is shown in figure 4.4. The VI will automatically perform one period of a sine sweep of steer angle according to the user's desired maximum steer angle and sweep frequency.

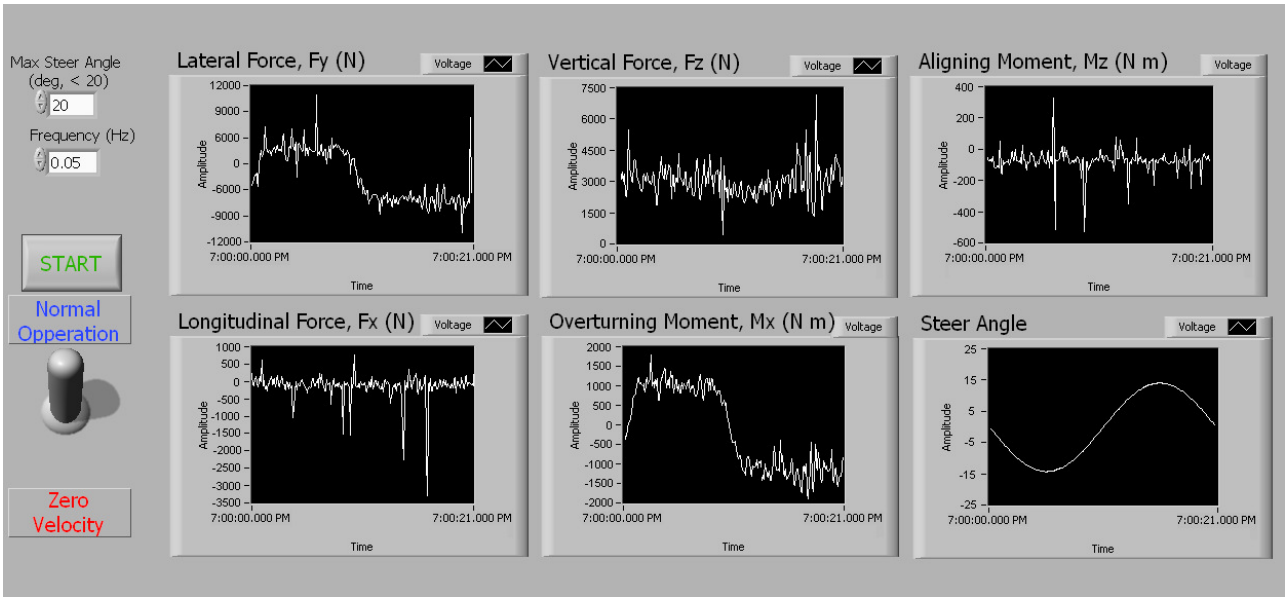

Figure 4.4. Front panel of LabView VI use to control test rig and collect data

4.2: Discussion of Experimental Procedure

There are several safety features that have been installed on the test rig in order to prevent damage to equipment and possible injury. While the trailer is being transported to its test location, the support plate on the rig is raised up so that a safety cover can be placed over the opening. For testing, a wireless video camera has been installed in the trailer which projects to a monitor inside the cab for the towing vehicle. Additionally, an emergency shut off switch is also

installed in the cab of the truck. The user can monitor the test from inside the cab and shut down the moving equipment in case of emergency.

After safety checks have been performed and all of the equipment in the trailer is up and running, the tire is mounted to the measurement hub. The tire is then lowered to the driving surface and the tire is loaded up to half of its rated load. The tire is driven for ten minutes at 30 mph to get the tire up to normal operating temperatures.

The user then manually adjusts the camber angle for each test. The tire is inflated or deflated to the desired pressure. The user then inputs the desired steer sweep and vertical load in the VI front panel. Once the trailer is brought up to speed the test can begin. It should be noted that the variable of interest is slip angle (see section 3.1.2) and not steer angle. However, all testing is carried out with straight line driving. With the assumption of no trailer sideslip, the slip angle will be equal to the steer angle.

Table 4-1 shows an example of a set of tests carried out on a Michelin HydroEdge P215/60R16. The tire was tested at camber angles of 0, 2, 4, and 6 degrees and vertical loads of ½ rated, ¾ rated, and rated vertical load. At each combination of vertical load and camber angle, a 15 degree slip angle sweep at 0.05 Hz was performed. All tests were performed at a forward speed of 31 mph and a tire inflation pressure of 35 psi. All of the testing for this tire was done on dry asphalt on an out of commission section of runway at Danville Regional Airport in Danville, VA. Lateral force, aligning moment, and overturning moment responses to slip angle, camber angle, and vertical load were measured and observed.

Table 4-1. Sample set of tests performed on Michelin HyrdoEdge P215/60R16

Model	Michelin HydroEdge
Size	P215/60R16
Load Index	94 (1477 lbs)
Speed Index	T (118 mph)
Inflation Pressure	35 psi
Forward Speed	31 mph (50 km/h)
Driving Surface	Dry Asphalt

Run #	Vertical Load (lbs)	Slip Angle (deg)	Camber Angle (deg)	Time
Warmup	½ rated (738.5)	0	0	10 min
1	½ rated (738.5)	15*sin(2*pi*0.05*t)	0	20 s
2	½ rated (738.5)	15*sin(2*pi*0.05*t)	2	20 s
3	½ rated (738.5)	15*sin(2*pi*0.05*t)	4	20 s
4	½ rated (738.5)	15*sin(2*pi*0.05*t)	6	20 s
5	¾ rated (1107.75)	15*sin(2*pi*0.05*t)	0	20 s
6	¾ rated (1107.75)	15*sin(2*pi*0.05*t)	2	20 s
7	¾ rated (1107.75)	15*sin(2*pi*0.05*t)	4	20 s
8	¾ rated (1107.75)	15*sin(2*pi*0.05*t)	6	20 s
9	rated (1477)	15*sin(2*pi*0.05*t)	0	20 s
10	rated (1477)	15*sin(2*pi*0.05*t)	2	20 s
11	rated (1477)	15*sin(2*pi*0.05*t)	4	20 s
12	rated (1477)	15*sin(2*pi*0.05*t)	6	20 s

4.3: Discussion of Collected Data and Trailer Validation

The data collected from the experiment in Table 4-1 was compared to an existing third party model as a means of validating the operation of the test trailer. The third party model is a lateral force tire model for the Michelin HydroEdge P215/60R16. The model was obtained by performing force and moment testing on the tire at 31 mph forward speed and 35 psi inflation pressure. All tests were carried out on a rolling road. The third party model provides lateral force response due to slip angle, camber angle, and vertical load.

Figure 4.5 – 4.8 shows plots of the collected data compared to the third party model. The dotted lines are the data collected from the test trailer and the solid lines are the third party fit for the respective vertical load, slip angle, and camber angle. The data displayed in the charts was processed according to the techniques described in section 3.5. The collected data matches the third party model within 14% error. A large portion of this error resides in the results from the four degree camber angle testing, in which there appeared to be an unknown source of error in the vertical load measurements. This data set has been included because it was part of the original test matrix, however, if it was excluded the error would be brought down below 10%.

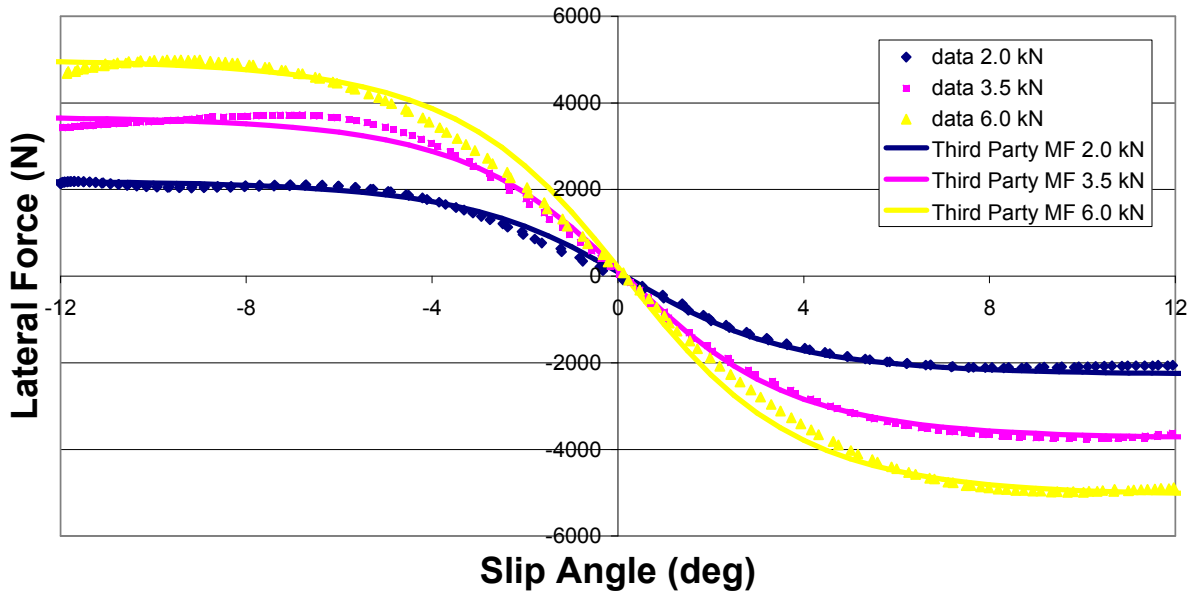

Figure 4.5. Lateral Force vs. Slip Angle (Michelin Hydroedge P215/60R16, 35psi, 31mph, 0 degree camber).

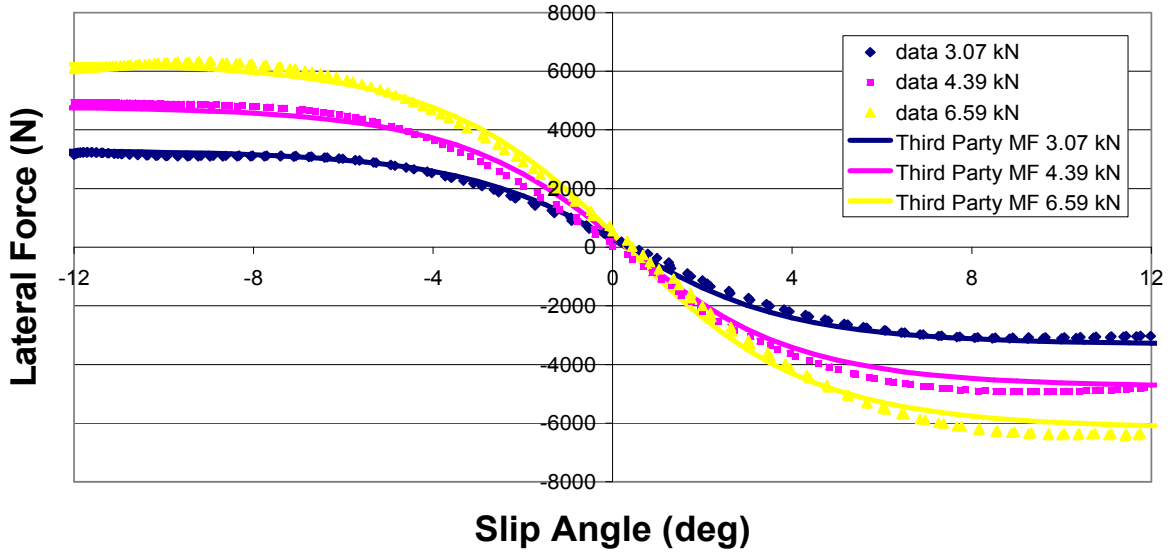

Figure 4.6. Lateral Force vs. Slip Angle (Michelin Hydroedge P215/60/R16, 35psi, 31mph, 2 deg camber).

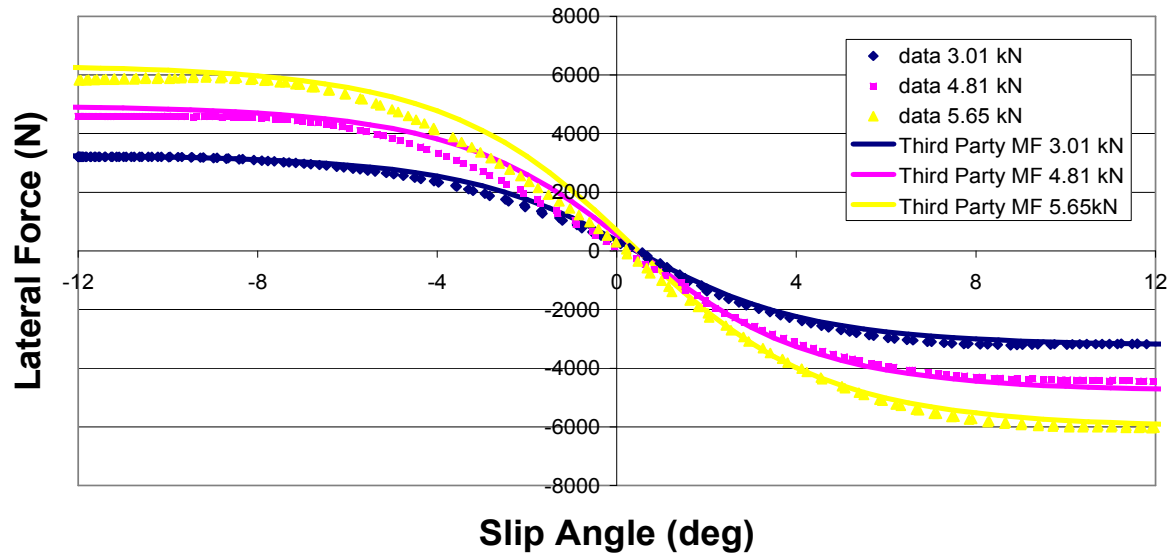

Figure 4.7. Force vs. Slip Angle (Michelin Hydroedge P215/60/R16, 35psi, 31mph, 4 deg camber).

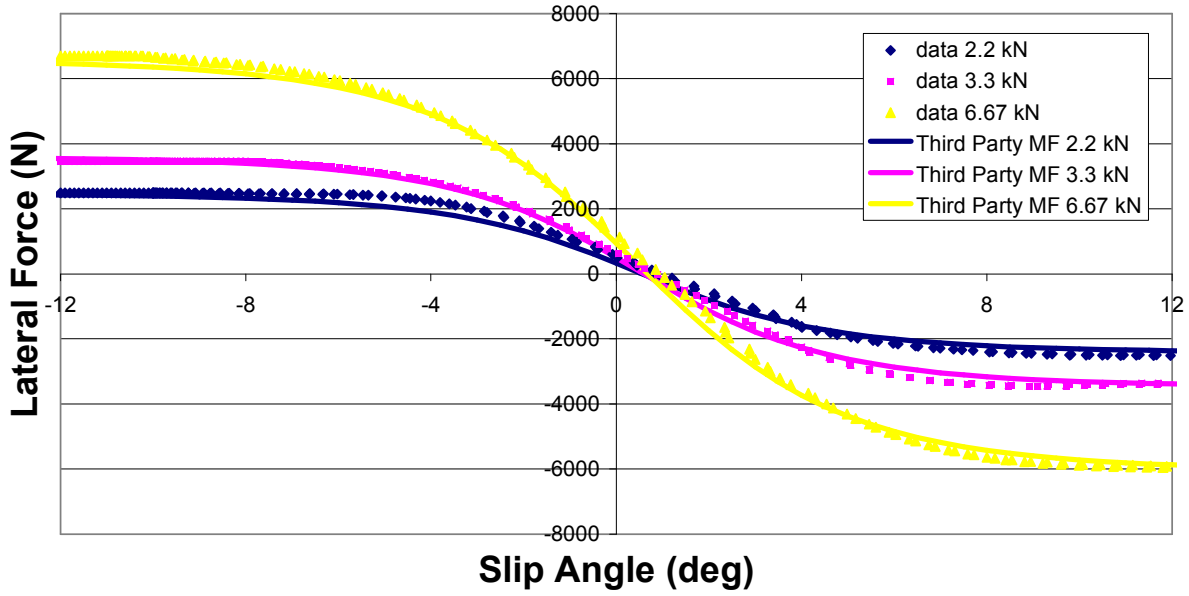

Figure 4.8. Force vs. Slip Angle (Michelin Hydroedge P215/60/R16, 35psi, 31mph, 6 deg camber).

4.4: Tire Testing on Off-Road Surfaces

In [7], the author performs tire force and moment testing on dry asphalt, wet asphalt, ice, and snow. The collected data was compared to force and moment data from a flat track test machine. This comparison allowed for the development of scaling factors. The scaling factors are effectively multipliers of each of the main coefficients in the Pacejka Magic Formula. The data from the flat track is used as a baseline set of data. The scaling factors from each of the driving surfaces can then be applied to the Magic Formula baseline to produce the force and moment characteristics for each of the respective driving surfaces. Some of the major findings in [7] are that the scaling factors are surface dependent, and are mostly independent of tire type, vehicle type, or vehicle speed. It was also found that the majority of the scaling occurs in the peak value scaling factor and the cornering stiffness scaling factor. These findings provide a

good basis for developing an off-road tire model for the studied tire. Because scaling factors are primarily independent of tire type, vehicle type, and vehicle speed, low speed off-road tests can be performed on a common passenger tire with the portable tire test rig to determine scaling factors for each off-road surface. The scaling factors can then be applied to the force and moment equations of the model of the studied tire, which was developed from rolling road testing. This will result in a tire model for different driving surfaces.

Since the studied tire is often driven on dirt and gravel, these two surfaces were studied. Dry asphalt was chosen as the baseline for this set of tests. Figure 4.9 shows a picture of the dry asphalt that the tire was tested on. The asphalt is standard black. Figure 4.10 shows a picture of the dirt surface that the tire was tested on. The dirt was compact and contained light gravel imbedded in it and resting on the surface. The gravel ranged in size from 0.125 inches to 0.75 inches in diameter. A picture of the gravel road is shown in figure 4.11. The gravel road consisted of heavy gravel resting on a dirt surface. The gravel ranged in size from about 0.125 inches to 1.5 inches in diameter. The ruler in the pictures is eight inches in length.

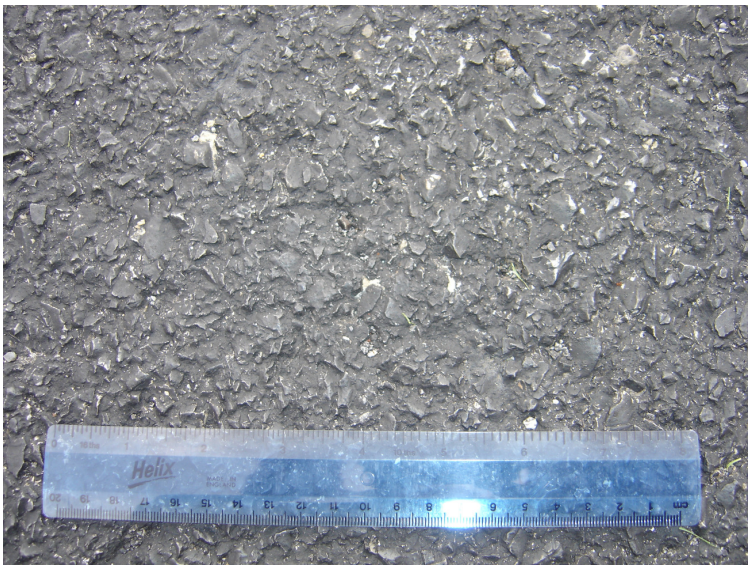

Figure 4.9. Dry asphalt driving surface used as a baseline for the off-road testing

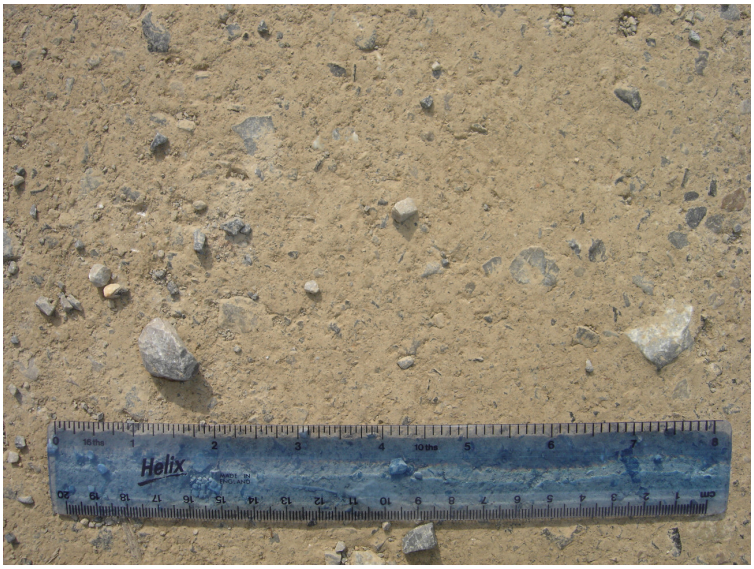

Figure 4.10. Dirt driving surface used for off-road tire testing

Figure 4.11. Gravel driving surface used for off-road tire testing

Tests were carried out by performing slip angle sweeps at different vertical loads on a Goodyear Assurance TT P215/60/R16 on each of the driving surfaces. The slip angle sweep consisted of a 19 degrees amplitude of a sine wave at 0.1 Hz. The vertical loads that were attempted were 20%, 40%, 60%, 80%, 90%, and 100% of the tire's rated vertical load. The actual vertical loads varied from these values and were recorded. The tire was inflated to 31 psi for all tests, was driven at 10 mph, and had zero degrees camber angle. This test matrix is shown in Table 4-2. For each test, the respective values were recorded in the open cells.

Table 4-2. Test matrix for off-road tire testing

Tire	Goodyear Assurance TT
Size	P215/60R16
Inflation Pressure	31 psi
Max Load	1477 lbs
Max Slip	19 deg
Slip Frequency	0.1 Hz
Camber Angle	0 deg
Driving Surface	Dry Asphalt, Dirt, Gravel
Forward Speed	10 mph
Warmup Speed	10 mph
Warmup Time	10 minutes
Warmup Load	300 lbs

	Vertical Load	**Inflation Pressure**	**Camber Angle**	**Speed**	**Max Slip Angle**	**Sweep Frequency**
Test 1 (20%, 295.4 lbs)						
Test 2 (40%, 590.8 lbs)						
Test 3 (60%, 886.2 lbs)						
Test 4 (80%, 1181.6 lbs)						
Test 5 (90%, 1239.3 lbs)						
Test 6 (100%, 1477 lbs)						

The majority of the scaling from one driving surface to another occurs in the peak friction scaling factor and the cornering stiffness scaling factor. Therefore, peak lateral force and cornering stiffness were extracted from the collected data for each test. Figure 4.12 shows a plot of peak lateral forces for different vertical loads for all three driving surfaces. Figure 4.13 shows a plot of cornering stiffness for different vertical loads for all three driving surfaces. As can be seen from both figures, the peak lateral force and cornering stiffness scale down fairly significantly for dirt and gravel, as compared to the dry asphalt. The determination of the scaling factors from this data will be discussed in Chapter 5.

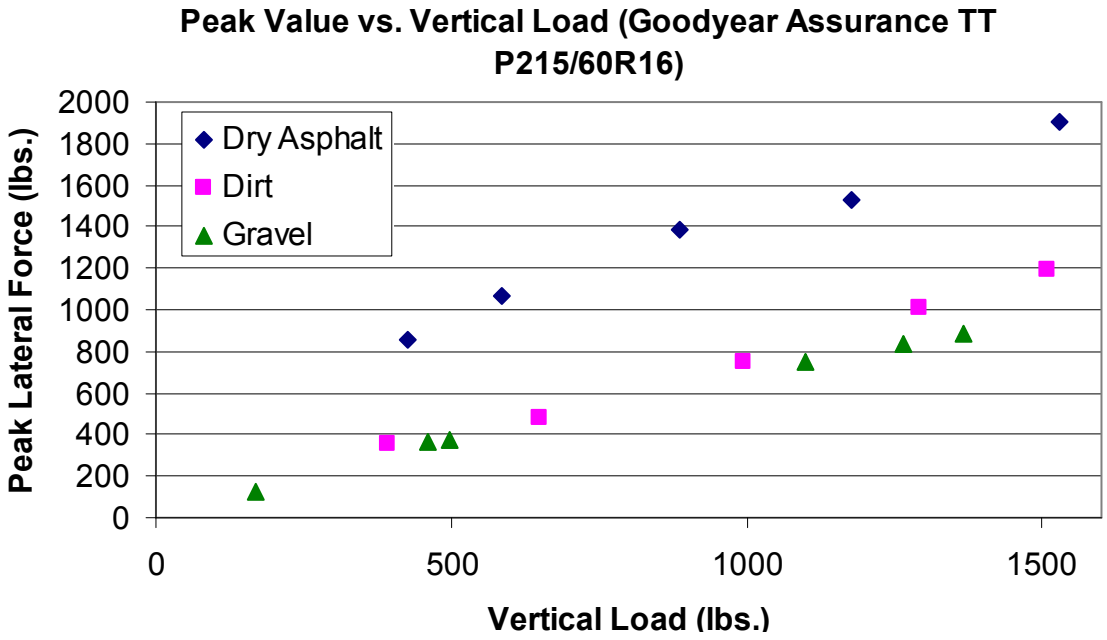

Figure 4.12. Peak lateral force vs. vertical load for different driving surfaces

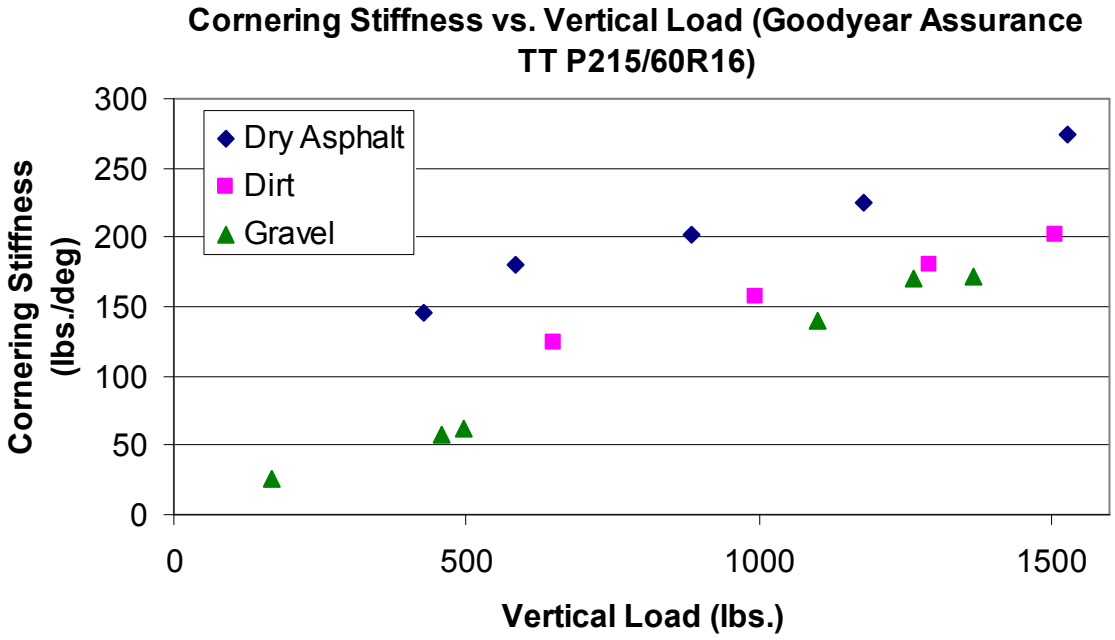

Figure 4.13. Cornering stiffness vs. vertical load for different driving surfaces

4.5: Conclusions

Tire force and moment testing is typically performed on a rolling road. These tests provide valuable information for vehicle dynamics studies. However, rolling roads are not able to simulate off-road surfaces. Off-road tire force and moment testing is needed to develop accurate tire models for vehicle dynamics studies, particularly for the studied vehicle. Data acquisition and hardware control software was developed for an existing portable tire test rig for the purpose of performing tire force and moment testing on on-road and off-road driving surfaces. The rig is capable of collecting force and moment response due to various inputs, such as: vertical load, slip angle, camber angle, forward speed, and inflation pressure. A sample set of data was collected on dry asphalt and compared to an existing third party model to prove operational validation of the test rig. The collected data matched the third party model within 14% error. Tests were also carried out dirt and gravel in order to obtain scaling factors that will

allow for the extension of flat track or dry asphalt tire model to off-road surfaces. The development of the force and moment tire model with off-road extensions is discussed in the following chapter.

Chapter 5: Tire Model Development with Off-Road Extensions

The data that was collected and described in Chapter 3 and Chapter 4 can be used in a semi-empirical tire model to accurately describe the force and moment characteristics of the studied tire. The force and moment testing performed on a stainless steel flywheel at Wright Patterson Air Force Base can be used as the basis for the studied tire model. The stainless steel flywheel data provides a good description of how the tire will perform on dry asphalt. The Pacejka Magic Formula [3] is a well known semi-empirical tire model that is widely used in the tire and automotive industry to describe the force and moment behavior of tires. The Magic Formula is an equation that is a function of slip and several coefficients that will be called main coefficients in this paper. The main coefficients in the Magic Formula are further defined by Pacejka coefficients and are functions of tire vertical load and camber angle. The main coefficients in the Magic Formula are individually defined for each force or moment acting on the tire. The Pacejka coefficients can be determined by a curve-fitting routine. Section 5.1 will explain the Magic Formula in detail and Section 5.2 and 5.3 will discuss a Matlab script that was developed for determining Pacejka coefficients.

The data collected from the off-road force and moment testing described in Chapter 4 will allow extensions to be made to the tire model developed using the Pacejka Magic Formula. These extensions include driving surface effects on tire lateral force. A method proposed in [7] describes how this can be done. Section 5.4 and 5.5 explain the driving surface extensions to the studied tire model.

5.1: Pacejka Magic Formula

The Pacejka Magic Formula [3] is a semi-empirical tire model that is widely used in the tire and automotive industry to describe force and moment behavior of tires as a function of vertical load, slip, and camber angle. The Magic Formula is a general equation that provides force and moment characteristic curves for a tire. Since the current study is focused on vehicle handling and stability, forces and moments that are primarily a function of slip angle are of interest (longitudinal force and rolling resistance are not studied). The general formula is

$$N = D\sin\left(C\arctan\left(B\left(\alpha + S_H\right) - E\left(B\left(\alpha + S_H\right) - \arctan\left(B\left(\alpha + S_H\right)\right)\right)\right)\right) + S_V, \tag{5.1}$$

where N is a force or moment acting on the tire, α is the slip angle, and B, C, D, E, S_H, and S_V are called main coefficients. B is the stiffness factor, C is the shape factor, D is the peak value, E is the curvature factor, S_H is the horizontal shift, and S_V is the vertical shift. The main coefficients are individually defined for each force or moment. For lateral force, N becomes F_y in equation 5.1, and the main coefficients are

$$C = a_0 \tag{5.2}$$

$$D = \left(a_1 F_z^2 + a_2 F_z\right)\left(1 - a_{15}\gamma^2\right) \tag{5.3}$$

$$E = \left(a_6 F_z + a_7\right)\left(1 - \left(a_{16}\gamma + a_{17}\right)\text{sign}\left(\alpha + S_H\right)\right) \tag{5.4}$$

$$K = a_3 \sin\left(2\arctan\left(F_z / a_4\right)\right)\left(1 - a_5|\gamma|\right) \tag{5.5}$$

$$B = K/\left(CD\right) \tag{5.6}$$

$$S_H = a_8 F_z + a_9 + a_{10}\gamma \tag{5.7}$$

$$S_V = a_{11} F_z + a_{12} + \left(a_{13} F_z + a_{14}\right) F_z \gamma \tag{5.8}$$

where γ is the camber angle, F_z is the vertical load, and a_0, a_1, … a_{17} are the Pacejka coefficients for lateral force. The Pacejka coefficients are determined by curve fitting the data from a series

of tests in which force and moment are measured in response to vertical load, slip angle, and camber angle (like those described in Chapter 3 and Chapter 4). The Magic Formula is able to accurately extrapolate outside of the range of measured inputs.

For aligning moment, N becomes M_z in equation (5.1) and the main coefficients are:

$$C = c_0 \tag{5.9}$$

$$D = \left(c_1 F_z^2 + c_2 F_z\right)\left(1 - c_{18}\gamma^2\right) \tag{5.10}$$

$$E = \left(c_7 F_z^2 + c_8 F_z + c_9\right)\left(1 - \left(c_{19}\gamma + c_{20}\right)\text{sign}\left(\alpha + S_H\right)\right)/\left(1 - c_{10}|\gamma|\right) \tag{5.11}$$

$$K = \left(c_3 F_z^2 + c_4 F_z\right)\exp\left(-c_5 F_z\right)\left(1 - c_6|\gamma|\right) \tag{5.12}$$

$$B = K/\left(CD\right) \tag{5.13}$$

$$S_H = c_{11}F_z + c_{12} + c_{13}\gamma \tag{5.14}$$

$$S_V = c_{14}F_z + c_{15} + \left(c_{16}F_z + c_{17}\right)F_z\gamma \tag{5.15}$$

where c_0, c_1, … c_{18} are the Pacejka coefficients for aligning moment.

It is shown in [6] that modifications can be made to the Magic Formula to model overturning moment. It was found that a quantity called the residual pneumatic scrub, P_r, closely resembles the shape of a lateral force vs. slip angle characteristic curve. The Magic Formula can be used to model the residual pneumatic scrub and then combined with other tire characteristics to obtain the overturning moment. The residual pneumatic scrub is:

$$P_r = D\sin\left(C\arctan\left(B\left(\alpha + S_H\right) - \left(E_0 + \Delta E\,\text{sign}\left(\alpha + S_H\right)\right)\left(B\left(\alpha + S_H\right) - \arctan B\left(\alpha + S_H\right)\right)\right)\right) + S_V \tag{5.16}$$

where,

$$C = m_0 \tag{5.17}$$

$$D = \left(m_1 F_z^2 + m_2 F_z\right)\left(1 - m_{15}\gamma^2\right) \tag{5.18}$$

$$K = m_3 \sin\left(2\arctan\left(F_z / m_4\right)\right)\left(1 - m_5|\gamma|\right) \tag{5.19}$$

$$B = K/(CD) \tag{5.20}$$

$$E_0 = m_6 F_z^2 + m_7 F_z \tag{5.21}$$

$$\Delta E = -\left(m_6 F_z^2 + m_7 F_z\right)\left(m_{16}\gamma + m_{17}\right)\text{sign}\left(\alpha + S_H\right) \tag{5.22}$$

$$S_H = m_8 F_z^2 + m_9 F_z + m_{10} F_z \gamma \tag{5.23}$$

$$S_V = m_{11} F_z^2 + m_{12} F_z + \left(m_{13} F_z^2 + m_{14} F_z\right)\gamma \tag{5.24}$$

where m_0, m_1, … m_{17} are the Pacejka coefficients for overturning moment. The modified pneumatic scrub can then be determined by

$$P_s = F_y / K_L - R_L \tan\gamma - P_r \tag{5.25}$$

where K_L is the lateral stiffness of the tire and R_L is the loaded radius of the tire. The overturning moment can then be determined by the relationship

$$M_x = P_s F_z \tag{5.26}$$

Once data is collected for a range of vertical loads, slip angles, and camber angles, the characteristic curves of lateral force, aligning moment, and overturning moment can be curve-fitted to produce the Pacejka coefficients for each.

5.2: Algorithm for Solving for Pacejka Coefficients

A Matlab script was developed to receive tire force and moment data as an input and calculate Pacejka coefficients to be used in equations (5.1) – (5.26). The program operates slightly different depending on whether slip angle and camber angle sweeps were performed, or if slip angle sweeps were performed at discrete camber angles. For the force and moment testing on the studied tire on the stainless steel flywheel, slip angle sweeps and camber angle sweeps were performed. For the off road testing using the portable tire test rig, slip angle sweeps were

performed at discrete camber angles. In both cases, the same general approach is used to calculate the Pacejka coefficients. First, estimates for the main coefficients are calculated for each individual curve in the data set. Next, these main coefficient estimates are all used together to calculate estimates for the Pacejka coefficients. Finally, the estimates for the Pacejka coefficients are used as initial guesses in a curve fitting routine that globally fits the data. The procedures will be explained in more detail in the following sections.

5.2.1: Algorithm for Data Sets Consisting of Slip Angle Sweeps at Discrete Camber Angles

For the purpose of explaining the functionality of the Matlab script, the process of solving for the Pacejka coefficients for lateral force will be used. For data sets that include slip angle sweeps at discrete camber angles, the data is first organized according to vertical load and camber angle. For each combination of vertical load and camber angle, there will be a lateral force vs. slip angle characteristic curve. For n vertical loads and m camber angles, there will be $p = m \times n$ curves. For each characteristic curve, estimates of the main coefficients are calculated, that is B_i, C_i, D_i, $E_{pos\text{-}i}$, $E_{neg\text{-}i}$, $S_{H\text{-}i}$, and $S_{V\text{-}i}$, for i= 1: p. E_{neg} is the value of E when $\text{sign}(\alpha + S_H)$ is negative, and E_{pos} is the value of E when $\text{sign}(\alpha + S_H)$ is positive.

Figure 5.1 shows a diagram that shows some of the data points that the Matlab script searches for in determining estimates for the main coefficients. $F_{y\text{-}max}$ is the maximum value of lateral force in the data set and $\alpha_{\max}$ is the slip angle at which this maximum value occurs. Likewise, $F_{y\text{-}min}$ is the minimum value of lateral force in the data set and $\alpha_{\min}$ is the slip angle at which this minimum value occurs.

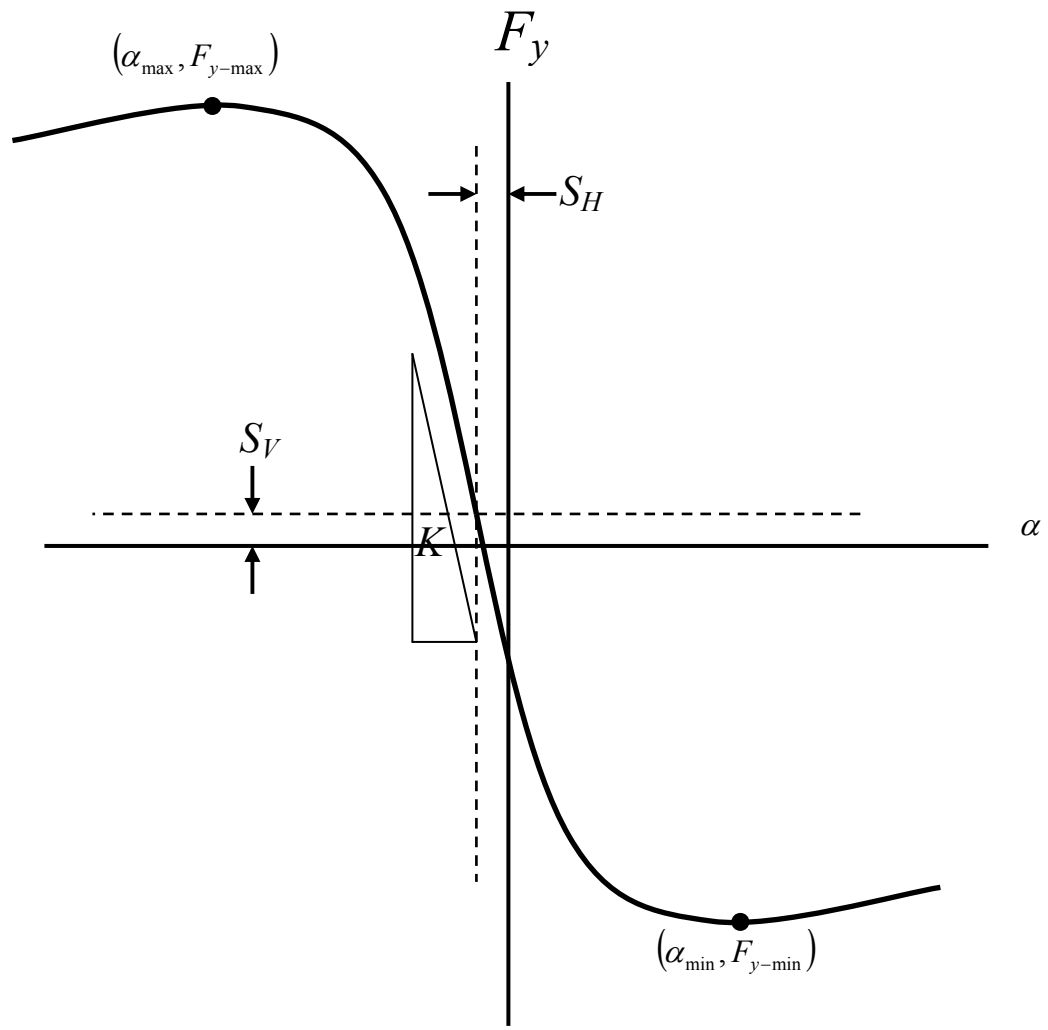

Figure 5.1. Figure used to help determine the initial guess for the main coefficients

The peak value estimate is determined by

$$D_i = \frac{F_{y-\max-i} - F_{y-\min-i}}{2} \tag{5.27}$$

The vertical shift estimate is determined by

$$S_{V-i} = \frac{F_{y-\max-i} + F_{y-\min-i}}{2} \tag{5.28}$$

The horizontal shift estimate is determined by

$$S_{H-i} = \frac{\alpha_{y-\max-i} + \alpha_{y-\min-i}}{2} \tag{5.29}$$

The shape factor estimate is $C_i = 1.3$. The shape factor for lateral force is usually around 1.3, so this is a good estimate. The cornering stiffness, K_i, is the slope of the curve at the coordinate: $\left(\alpha_i = -S_{H-i}, F_{y-i} = S_{V-i}\right)$. The stiffness factor estimate is determined by

$$B_i = \frac{K_i}{C_i D_i} \tag{5.30}$$

The positive and negative curvature factor estimates can then be determined by

$$E_{pos-i} = \frac{B_i\left(\alpha_{\min-i} + S_{H-i}\right) - \tan\left(\pi/2C_i\right)}{B_i\left(\alpha_{\min-i} + S_{H-i}\right) - \arctan\left(B_i\left(\alpha_{\min-i} + S_{H-i}\right)\right)} \tag{5.31}$$

$$E_{neg-i} = \frac{B_i\left(\alpha_{\max-i} + S_{H-i}\right) - \tan\left(\pi/2C_i\right)}{B_i\left(\alpha_{\max-i} + S_{H-i}\right) - \arctan\left(B_i\left(\alpha_{\max-i} + S_{H-i}\right)\right)} \tag{5.32}$$

After all of the main coefficient estimates have been calculated for each of the lateral force vs. slip angle curves, estimates of the Pacejka coefficients are calculated. First, Pacejka coefficients not related to camber angle are determined. This is done by using all of the lateral force vs. slip angle curves for camber angle equal to zero degrees. Setting $\gamma = 0$ simplifies equation (5.3) to

$$D_i = \left(a_{1\text{-e}} F_{z-i}^2 + a_{2\text{-e}} F_{z-i}\right) \tag{5.33}$$

where the subscript *e* denotes an estimate of a Pacejka coefficient. This equation is then used with the value D_i and $F_{z\text{-}i}$ from each data set where $\gamma = 0$ to create n –1 sets of a system of two equations. For each system of equations, $a_{1\text{-e}}$ and $a_{2\text{-e}}$ are solved for. This produces n – 1 values for $a_{1\text{-e}}$ and $a_{2\text{-e}}$. These values are averaged to produce estimates for $a_{1\text{-e}}$ and $a_{2\text{-e}}$, respectively.

This same procedure is used to determine the values for the estimates of $a_{6\text{-e}}$, $a_{7\text{-e}}$, $a_{8\text{-e}}$, $a_{9\text{-e}}$, $a_{11\text{-e}}$, and $a_{12\text{-e}}$ using the equations:

$$\frac{E_{pos-i} + E_{neg-i}}{2} = a_{6\text{-e}} F_{z-i} + a_{7\text{-e}} \tag{5.34}$$

$$S_{H-i} = a_{8\text{-e}} F_{z-i} + a_{9\text{-e}} \tag{5.35}$$

$$S_{V-i} = a_{11\text{-e}} F_{z-i} + a_{12\text{-e}} \tag{5.36}$$

along with the data sets for $\gamma = 0$.

Since estimates of $a_{6\text{-e}}$ and $a_{7\text{-e}}$ are calculated, several values for $a_{17\text{-e}}$ can be calculated using the equations

$$a_{17\text{-e}} = 1 - \frac{E_{pos-i}}{a_{6\text{-e}} F_z + a_{7\text{-e}}} \tag{5.37}$$

$$a_{17\text{-e}} = \frac{E_{neg-i}}{a_{6\text{-e}} F_z + a_{7\text{-e}}} - 1 \tag{5.38}$$

All of the values for $a_{17\text{-e}}$ from these two equations can be averaged to produce an estimate for $a_{17\text{-e}}$.

The estimate for $a_{0\text{-e}}$ is C_i, therefore the estimate for $a_{0\text{-e}} = 1.3$. An estimate of $a_{3\text{-e}}$ and $a_{4\text{-e}}$ can be obtained by creating a plot of the cornering stiffness, K_i, versus the vertical load, $F_{z\text{-}i}$, for all of the data sets where $\gamma = 0$. Figure 5.2 shows how $a_{3\text{-e}}$ and $a_{4\text{-e}}$ can be obtained from plotting K_i versus $F_{z\text{-}i}$. The maximum value of K_i is $a_{3\text{-e}}$, and the vertical load at which this maximum value occurs is $a_{4\text{-e}}$.

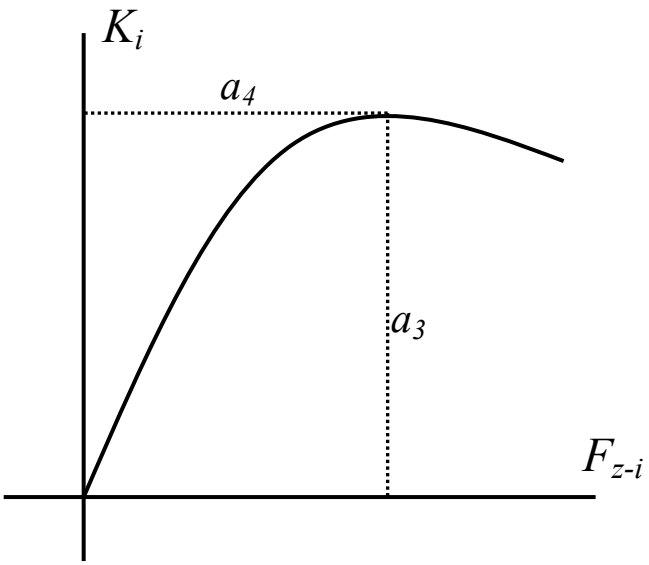

Figure 5.2. Cornering stiffness vs. vertical load for data sets with $\gamma = 0$

Once all of the Pacejka coefficient estimates for $a_{0\text{-e}}$, $a_{1\text{-e}}$, $a_{2\text{-e}}$, $a_{3\text{-e}}$, $a_{4\text{-e}}$, $a_{6\text{-e}}$, $a_{7\text{-e}}$, $a_{8\text{-e}}$, $a_{9\text{-e}}$, $a_{11\text{-e}}$, $a_{12\text{-e}}$, and $a_{17\text{-e}}$ have been solved for, these values can be used along with data sets with $\gamma \neq 0$ to solve for $a_{5\text{-e}}$, $a_{10\text{-e}}$, $a_{13\text{-e}}$, $a_{14\text{-e}}$, $a_{15\text{-e}}$, and $a_{16\text{-e}}$. The estimates for $a_{5\text{-e}}$, $a_{10\text{-e}}$, and $a_{15\text{-e}}$ can be solved for directly with the equations:

$$a_{5\text{-e}} = \left(\frac{1}{|\gamma_i|}\right)\left(1 - \frac{K_i}{a_{3\text{-e}} \sin\left(2\arctan\left(F_{z-i}/a_{4\text{-e}}\right)\right)}\right) \tag{5.39}$$

$$a_{10\text{-e}} = \frac{S_{H-i} - a_{8\text{-e}} F_{z-i} - a_{9\text{-e}}}{\gamma_i} \tag{5.40}$$

$$a_{15\text{-e}} = \left(\frac{1}{\gamma_i^2}\right)\left(1 - \frac{D_i}{a_{1\text{-e}} F_{z-i}^2 + a_{2\text{-e}} F_{z-i}}\right) \tag{5.41}$$

This will create sets of $(m-1)\times n$ values for each of $a_{5\text{-e}}$, $a_{10\text{-e}}$, and $a_{15\text{-e}}$. These sets can be averaged to get the estimate for each coefficient.

The values for $a_{13\text{-e}}$ and $a_{14\text{-e}}$ can be found using:

$$a_{13\text{-e}}F_{z-i} + a_{14\text{-e}} = \frac{S_{V-i} - a_{11\text{-e}}F_{z-i} - a_{12\text{-e}}}{F_{z-i}\gamma_i}, \tag{5.42}$$

and then creating $\left((m-1)\times n\right)-1$ sets of systems of two equations. The equations can be simultaneously solved for and the results from all of the sets averaged to produce estimates for $a_{13\text{-e}}$ and $a_{14\text{-e}}$.

The estimate for $a_{16\text{-e}}$ can found using the two equations

$$a_{16\text{-e}} = \left(\frac{1}{\gamma_i}\right)\left(1 - \frac{E_{pos-i}}{a_{6\text{-e}}F_{z-i} + a_{7\text{-e}}} - a_{17\text{-e}}\right) \tag{5.43}$$

$$a_{16\text{-e}} = \left(\frac{1}{\gamma_i}\right)\left(\frac{E_{neg-i}}{a_{6\text{-e}}F_{z-i} + a_{7\text{-e}}} - 1 - a_{17\text{-e}}\right) \tag{5.44}$$

These two equations will produce $2\times\left(m-1\right)\times n$ values for $a_{16\text{-e}}$ which can be average to obtain an estimate for $a_{16\text{-e}}$.

The estimates for all of the Pacejka coefficients are then used as initial guesses in a curve fitting routine that globally fits the data to the Magic Formula. Just like the calculations for the initial guesses, the actual values of the Pacejka coefficients are determined in two steps: first for the coefficients that are not related to camber angle, then for the coefficients that are. When solving for the coefficients related to camber angle, the values for coefficients not related to camber angle are used in the equations. The Matlab script will produce a final set of Pacejka coefficients that best fits the entire data set as a whole by minimizing the error. Similar routines are used to solve for the Pacejka coefficients for overturning moment and aligning moment.

5.2.2: Algorithm for Data Sets Consisting of Slip Angle Sweeps and Camber Angle Sweeps

In solving for the Pacejka coefficients for sets of data that include slip angle sweeps at zero camber angle and camber angle sweeps at zero slip angle, the same methods described in

the previous section are utilized to obtain estimates for $a_{0\text{-e}}$, $a_{1\text{-e}}$, $a_{2\text{-e}}$, $a_{3\text{-e}}$, $a_{4\text{-e}}$, $a_{6\text{-e}}$, $a_{7\text{-e}}$, $a_{8\text{-e}}$, $a_{9\text{-e}}$, $a_{11\text{-e}}$, $a_{12\text{-e}}$, and $a_{17\text{-e}}$. This includes the use of equations (5.27) – (5.38). A minimization routine can then be used to solve for the actual values of the Pacejka coefficients not related to camber angle, using the calculated estimates as initial guess for the coefficients.

Solving for a_5, a_{10}, a_{13}, a_{14}, a_{15}, and a_{16}, however, involves a different process. All of the data for $\gamma \neq 0$ is used for the computations. Since the slip angle is zero for all of the camber angle sweeps, the main equation becomes:

$$F_{y-i} = D_i \sin\left(C_i \arctan\left(B_i S_{H-i} - E_i\left(B_i S_{H-i} - \arctan\left(B_i S_{H-i}\right)\right)\right)\right) + S_{V-i} \tag{5.45}$$

The coefficients in this equation are:

$$D_i = d_i\left(1 - a_{15}\gamma_i^2\right) \tag{5.46}$$

$$E_i = e_i\left(1 - a_{17} - a_{16}\gamma_i\right) \tag{5.47}$$

$$K_i = k_i\left(1 - a_5\left|\gamma_i\right|\right) \tag{5.48}$$

$$C_i = a_0 \tag{5.49}$$

$$B_i = \frac{K_i}{C_i D_i} \tag{5.50}$$

$$S_{H-i} = s_{H-i} + a_{10}\gamma_i \tag{5.51}$$

$$S_{V-i} = s_{V-i} + \left(a_{13}F_{z-i} + a_{14}\right)F_{z-i}\gamma_i \tag{5.52}$$

where:

$$d_i = a_1 F_{z-i}^2 + a_2 F_{z-i} \tag{5.53}$$

$$e_i = a_6 F_{z-i} + a_7 \tag{5.54}$$

$$k_i = a_3 \sin\left(2\arctan\left(F_{z-i}/a_4\right)\right) \tag{5.55}$$

$$s_{H-i} = a_8 F_{z-i} + a_9 \tag{5.56}$$

$$s_{V-i} = a_{11}F_{z-i} + a_{12} \tag{5.57}$$

Equations (5.46) – (5.57) can be inserted into equation (5.45) to get:

$$\begin{aligned} F_{y-i} = d_i\left(1 - a_{15}\gamma_i^2\right)\sin\left(a_0 \arctan\left(x_i - e_i\left(1 - a_{17} - a_{16}\gamma_i\right)\left(x_i - \arctan\left(x_i\right)\right)\right)\right) + \ldots \\ \ldots + s_{V-i} + \left(a_{13}F_{z-i} + a_{14}\right)F_{z-i}\gamma_i \end{aligned} \tag{5.58}$$

where:

$$x_i = B_i S_{H-i} = \frac{b_i\left(1 - a_5\left|\gamma_i\right|\right)\left(s_{H-i} + a_{10}\gamma_i\right)}{1 - a_{15}\gamma_i^2} \tag{5.59}$$

Equation (5.58) is written so that the lateral force is now a function of camber angle, with vertical load and Pacejka coefficients not related to camber angle as constants. Since all of the Pacejka coefficients related to camber angle are typically close to zero in value, equation (5.58) can be used with a minimization routine with the initial guesses of zero for all Pacejka coefficients to solve for the actual values of a_5, a_{10}, a_{13}, a_{14}, a_{15}, and a_{16}. Similar routines are used to solve for the Pacejka coefficients for overturning moment and aligning moment.

5.3: Characterization of the Studied Tire Using Matlab Script

The data for the studied tire collected from the testing performed on a stainless steel flywheel (Chapter 3) was run through the Matlab script to calculate the Pacejka coefficients for the tire. The Pacejka coefficients for lateral force for 5 mph, 20 mph, 40 mph, and 65 mph forward speed are shown in Table 5-1, 5-2, 5-3, and 5-4, respectively. The Pacejka coefficients are used with equations (5.1) – (5.8) to solve for the lateral force acting on the tire as a function of vertical load, slip angle, and camber angle.

Table 5-1. Pacejka coefficients for lateral force for studied tire at 5 mph

a_0	1.0476	a_9	2.3074
a_1	-5.4979	a_{10}	-0.0211
a_2	-1038.0146	a_{11}	-10.9126
a_3	-4043.5115	a_{12}	4184.9585
a_4	-68.6282	a_{13}	-0.18775
a_5	-0.02238	a_{14}	-31.43279
a_6	-0.0010001	a_{15}	0.0000
a_7	0.3473	a_{16}	4.07498
a_8	0.008724	a_{17}	2.3612

Table 5-2. Pacejka coefficients for lateral force for studied tire at 20 mph

a_0	1.2391	a_9	0.8150
a_1	-6.5995	a_{10}	-0.00797
a_2	-1004.7562	a_{11}	-80.9979
a_3	-4519.5856	a_{12}	-580.2490
a_4	-73.64712	a_{13}	0.09147
a_5	-0.0163	a_{14}	-17.4167
a_6	-0.0175	a_{15}	0.0000
a_7	-0.2839	a_{16}	3.9122
a_8	-0.0134	a_{17}	1.0359

Table 5-3. Pacejka coefficients for lateral force for studied tire at 40 mph

a_0	1.5000	a_9	0.3058
a_1	-6.7531	a_{10}	-0.08954
a_2	-845.0971	a_{11}	-10.8582
a_3	-5397.5039	a_{12}	-698.9398
a_4	-72.2475	a_{13}	0.00728
a_5	0.0302	a_{14}	-11.9981
a_6	-0.0019	a_{15}	-0.0000524
a_7	1.1396	a_{16}	-1.9635
a_8	-0.00727	a_{17}	0.00827

Table 5-4. Pacejka coefficients for lateral force for studied tire at 65 mph

a_0	1.2000	a_9	0.5562
a_1	-5.8990	a_{10}	-0.04317
a_2	-899.2336	a_{11}	-10.9181
a_3	-5134.5637	a_{12}	-207.2104
a_4	-70.4025	a_{13}	-0.01239
a_5	0.03329	a_{14}	-15.8141
a_6	-0.00466	a_{15}	0.0000
a_7	1.2004	a_{16}	-16.4037
a_8	-0.0035	a_{17}	0.01877

Figure 5.3 and 5.4 show plots of lateral force vs. slip angle and lateral force vs. camber angle, respectively. The plots compare the raw data collected from the rolling road testing to the Magic Formula generated curve for three different vertical loads. The Magic Formula generated curve for these plots is based on the Pacejka coefficients from table 5-1, which are applicable for a forward speed of 5 mph. As can be seen from the plots, the Pacejka coefficients along with the Magic Formula do a good job of fitting the data. These two plots are just samples to show that the Pacejka coefficients accurately describe the tire force and moment characteristics.

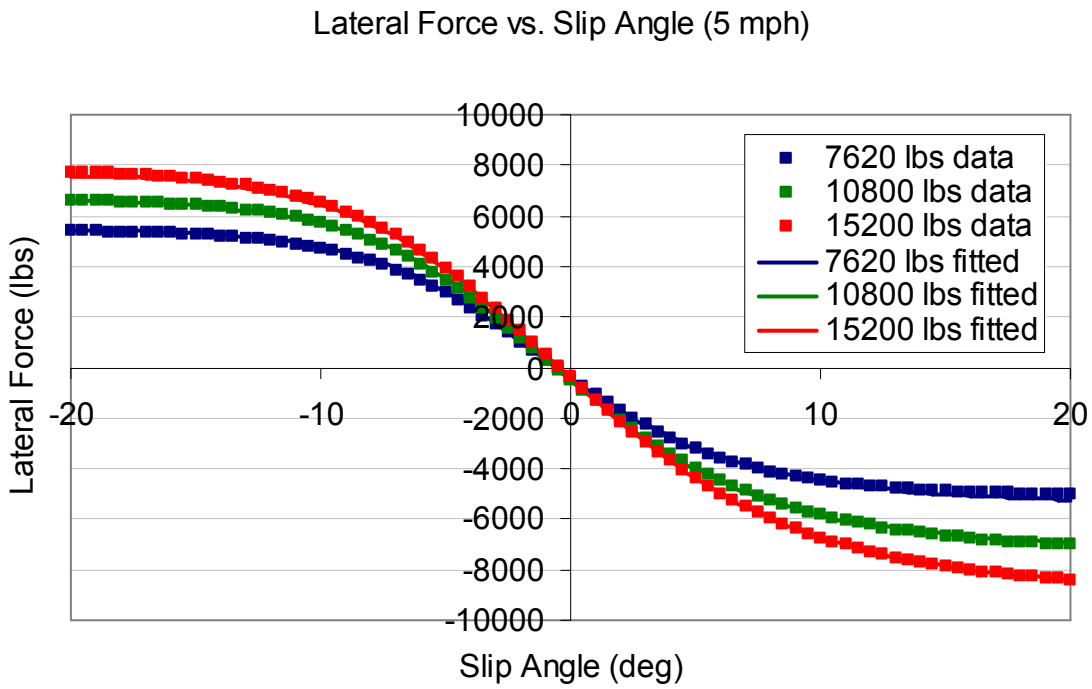

Figure 5.3. Lateral force vs. slip angle, raw data vs. Magic Formula fit

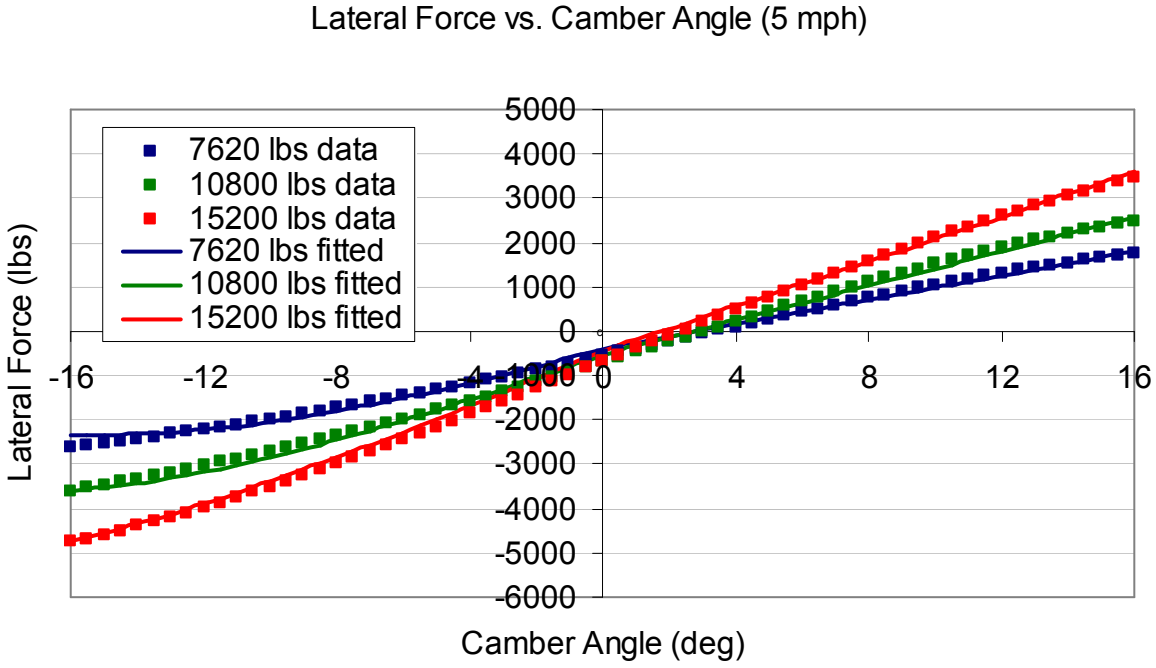

Figure 5.4. Lateral force vs. camber angle, raw data vs. Magic Formula fit

5.4: Determination of Scaling Factors from Off-Road Tire Testing

Section 4.4 discussed the experimental procedure of off-road tire force and moment testing on dirt and gravel. In [7], the author researches the effects of different driving surfaces on tire force and moment behavior. The author investigates the use of the scaling factor extension to the Magic Formula as shown in [3]. Setting $N = F_y$ in equation (5.1) gives the equation that will be used as a baseline for the lateral force scaling. A separate scaling factor is then applied to each of the main coefficients in the Magic Formula to account for the different driving surfaces. For lateral force, equations (5.2) – (5.8) become:

$$C_{\text{scaled}} = \lambda_C \cdot a_0 \tag{5.60}$$

$$D_{\text{scaled}} = \lambda_D \cdot \left(a_1 F_z^2 + a_2 F_z\right)\left(1 - a_{15}\gamma^2\right) \tag{5.61}$$

$$E_{\text{scaled}} = \lambda_E \cdot \left(a_6 F_z + a_7\right)\left(1 - \left(a_{16}\gamma + a_{17}\right)\text{sign}\left(\alpha + S_H\right)\right) \tag{5.62}$$

$$K_{\text{scaled}} = \lambda_K \cdot a_3 \sin\left(2\arctan\left(F_z / a_4\right)\right)\left(1 - a_5|\gamma|\right) \tag{5.63}$$

$$B_{\text{scaled}} = K_{\text{scaled}} / \left(C_{\text{scaled}} D_{\text{scaled}}\right) \tag{5.64}$$

$$S_{H,\text{scaled}} = \lambda_{SH} \cdot \left(a_8 F_z + a_9 + a_{10}\gamma\right) \tag{5.65}$$

$$S_{V,\text{scaled}} = \lambda_{SV} \cdot \left(a_{11} F_z + a_{12} + \left(a_{13} F_z + a_{14}\right) F_z \gamma\right), \tag{5.66}$$

where λ is the scaling factor for each of the main coefficients. The Pacejka coefficients in equations (5.2) – (5.8) are determined by curve fitting the collected data from the control set, which can be data collected from testing on a rolling road or dry asphalt. The known values of the Pacejka coefficients are then used with equations (5.60) – (5.66) to determine the scaling factor, λ, for each of the main coefficients. The goal is to determine the scaling factors for a driving surface so that the driving surface itself can be described strictly with the scaling factors.

It was shown in [7] that the scaling factors for lateral force are primarily surface dependent and are mostly independent of tire type, vehicle type, or vehicle speed. For this reason, tests were carried out on a Goodyear Assurance TT P215/60R16 at 10 mph with the portable tire test rig. Tests were performed on dry asphalt (the baseline surface), dirt, and gravel. The scaling factors for dirt and gravel determined from these tests can then be used to make an off-road extension to the studied tire model. It was also shown in [7] that the majority information in scaling force and moment data from one surface to another is contained in the peak value scaling factor, λ_D, and the cornering stiffness scaling factor, λ_K. This is a convenient fact because off-road data typically contains a lot of process noise from uncertainties in the driving surface. As a result, smooth force and moment curves are difficult to obtain, and it is therefore difficult to produce a complete set of Pacejka coefficients. However, peak value and cornering stiffness are relatively easy values to obtain from the collected off-road data. For this reason, the scaling factor extension to the studied tire will consist of determining the values of λ_D and λ_K for each off-road driving surface. The remainder of the scaling factors will be assumed to be unity.

Calculation of the scaling factors begins with extracting the peak value and cornering stiffness (the slope at the origin) of the lateral force vs. slip angle curves for each vertical load. Next, the Pacejka coefficients a_1 and a_2 need to be calculated for the control data set, which is dry asphalt. Since all of the tests were carried out at zero camber angle, equation (5.3) reduces to:

$$D = \left(a_1 F_z^2 + a_2 F_z\right) \tag{5.67}$$

The data set of peak values, D, and vertical loads, F_z, is then curve-fitted to equation (5.67) to determine the values of a_1 and a_2. Curve fitting of the dry asphalt data yields a_1 = -47.6 and a_2 =

-1624. The peak value scaling factor for each surface can then be obtained by using the peak value and vertical load data for each surface, the values for a_1 and a_2 previously calculated, and curve fitting to the equation:

$$D = \lambda_D \cdot \left(a_1 F_z^2 + a_2 F_z\right) \tag{5.68}$$

to solve for the peak value scaling factor λ_D.

Similarly, the stiffness scaling factor can be determined by first calculating the values for a_3 and a_4 with the dry asphalt data. Using the values of cornering stiffness at each vertical load, the Pacejka coefficients can be determined by curve-fitting to the equation:

$$K = a_3 \sin\left(2\arctan\left(F_z / a_4\right)\right) \tag{5.69}$$

which is obtained from setting camber angle equal to zero in equation (5.5). The values determined for dry asphalt are a_3 = -1898.33 and a_4 = -16.00. These can then be used with the cornering stiffness and vertical load data for the off-road surfaces and curve fitting it to the equation:

$$K = \lambda_K \cdot a_3 \sin\left(2\arctan\left(F_z / a_4\right)\right) \tag{5.60}$$

Figure 5.5 shows the collected data and curve fits for peak lateral force vs. vertical load for dry asphalt, dirt, and gravel. Figure 5.6 shows the collected data and curve fits for cornering stiffness vs. vertical load for dry asphalt, dirt, and gravel. The plots show that the curve-fits match the collected data reasonably well and also provide an easy way for determining the scaling factors. The plots display lateral force in Newtons, cornering stiffness in Newtons per degree, and vertical load in negative kilo-Newtons. This unit convention is used because these are the standard units to be used with the Magic Formula. This should be noted when using the calculated scaling factors.

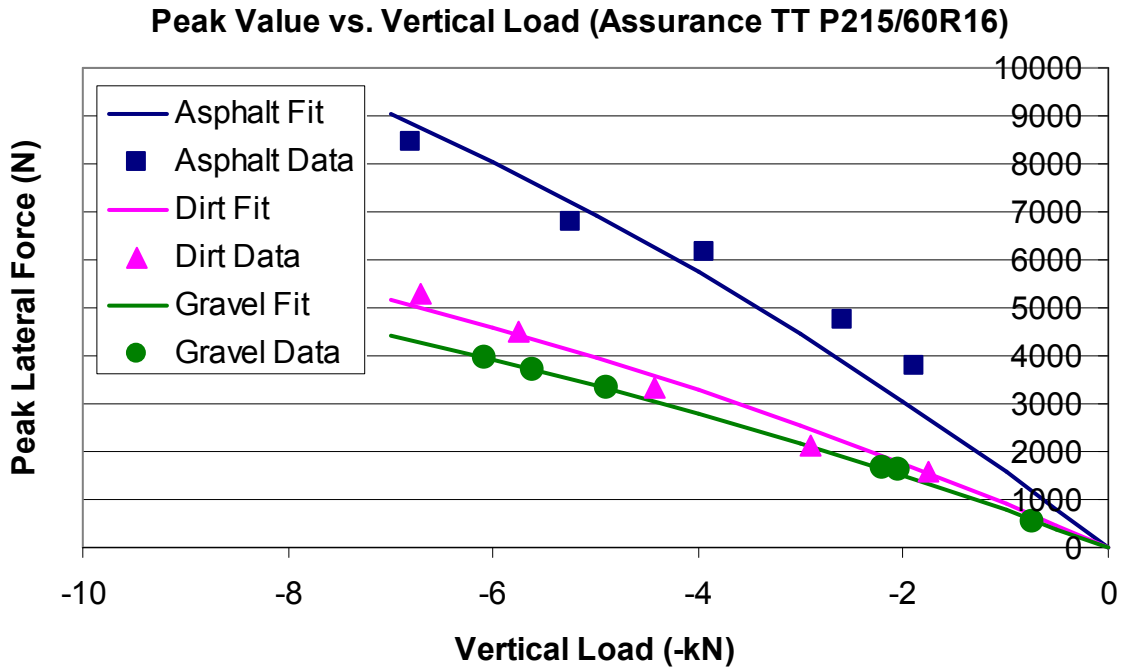

Figure 5.5. Peak lateral force vs. vertical load for P215/60R16 on asphalt, dirt, and gravel

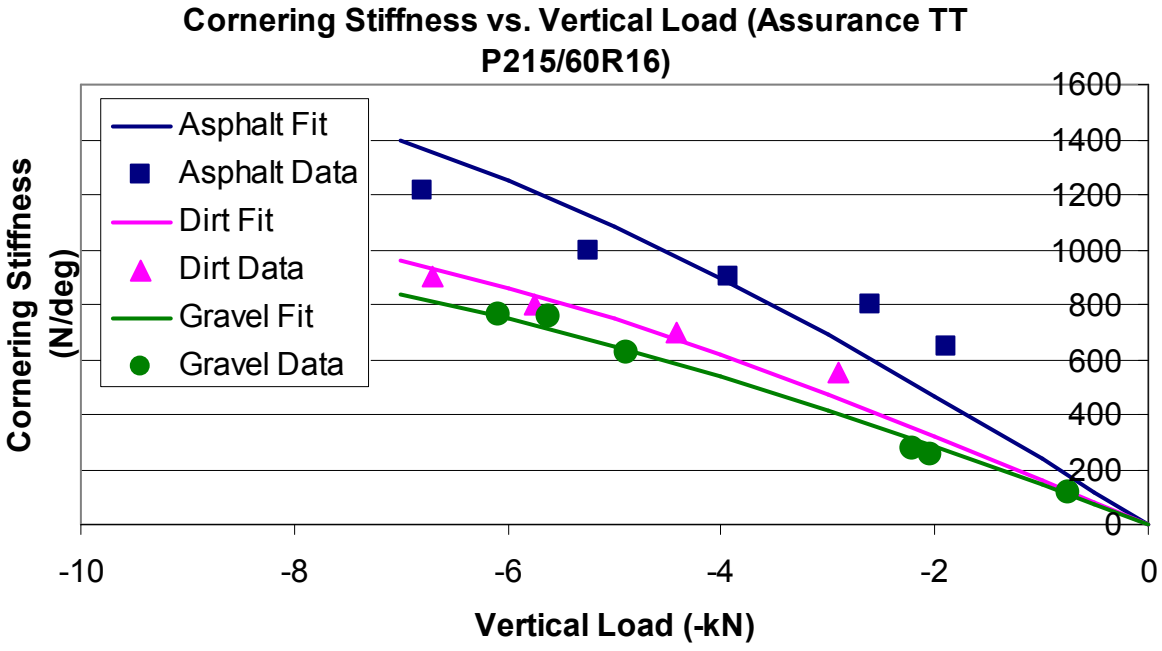

Figure 5.6. Cornering stiffness vs. vertical load for P215/60R16 on asphalt, dirt, and gravel

The peak value and cornering stiffness scaling factors for dirt and gravel calculated from this curve fitting procedure are shown in table 5-5. As can be seen from these values, the dirt driving surface is capable of producing 57.3% of the maximum lateral forces produced on dry asphalt and the gravel driving surface is capable of producing 49.0% of the maximum lateral forces produced on dry asphalt. The cornering stiffnesses, which governs the lateral force behavior in the linear region, is 69.0% of the dry asphalt value on dirt, and 60.2% of the dry asphalt value on gravel. Assuming $\lambda_C, \lambda_E, \lambda_{SH}, \lambda_{SV}$ to be unity, the scaling factors in table 5-5 can be used with equations (5.60) – (5.66) to extend a dry asphalt or flat track force and moment tire model to dirt and gravel.

Table 5-5. Peak value and cornering stiffness scaling factors for dirt and gravel

Driving Surface	λ_D	λ_K
Dirt	0.573	0.690
Gravel	0.490	0.602

5.5: Scaling Factor Extension to the Studied Tire

The lateral force tire model developed in section 5.4 can be extended to an off-road tire model through the use of the scaling factors in table 5-5. Even though the tire model was developed from flat track testing and the scaling factors were developed from dry asphalt testing as a baseline, dry asphalt and flat track tests typically exhibit similar friction characteristics, so the scaling factors can still be used. By setting $\lambda_C, \lambda_E, \lambda_{SH}, \lambda_{SV}$ equal to one and using the calculated values λ_D and λ_K, a lateral force tire model for dirt and gravel can be developed. The Pacejka coefficients in table 5-1 – 5-4 can be used with equations (5.60) – (5.66) and equation (5.1) to determine the lateral force acting on the tire as a function of vertical load, slip angle, and

camber angle. Figure 5.7 shows a plot of lateral force vs. slip angle for the studied tire at 40 mph and 7620 lbs lateral force. The flat track curve is the curve resulting from the Pacejka coefficients in table 5-1. The dirt and gravel curves are generated from the same Pacejka coefficients and the scaling factors in table 5-5. The scaling factor extension can thus be used to obtain the lateral force characteristic for any slip angle, camber angle, and vertical load on dirt and gravel. This off-road tire model can then be used in off-road vehicle simulations, which will be discussed in chapter 7.

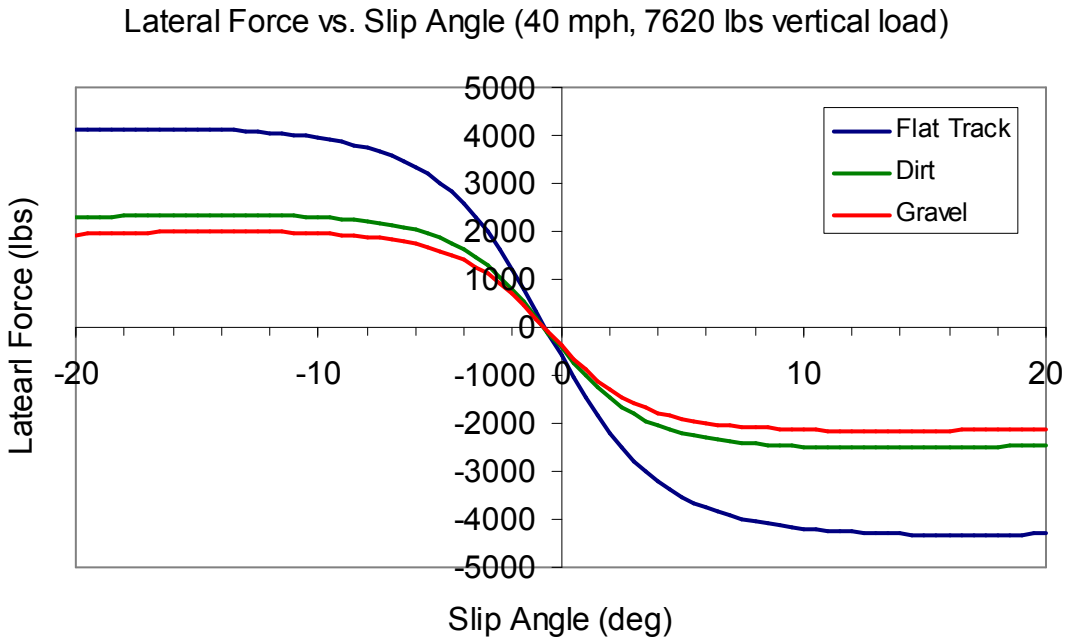

Figure 5.7. Lateral force vs. slip on flat track, dirt, and gravel at 40 mph, 7650 lbs. vertical load

5.6: Conclusions

The force and moment tire data collected from a rolling road (chapter 3) and the portable tire test rig (chapter 4) can be processed to generate a tire model. The Pacejka Magic Formula was used to do this. The Pacejka Magic formula consists of several parameters called Pacejka coefficients that are necessary for predicting the force and moment behavior of the tire. These

coefficients can be determined by using collected data along with the proposed curve fitting routine.

Scaling factors for dirt and gravel were calculated from the data obtained from the off-road tire testing described in chapter 4. These scaling factors can be used with the Pacejka coefficients determined from rolling road testing to generate an off-road lateral force tire model for dirt and gravel. This model can be used in vehicle simulations studies to develop rollover mitigation strategies, which will be discussed in chapter 7.

Chapter 6: Vehicle Model Development

The purpose of developing the tire model in the previous chapter was to implement it into an overall vehicle model so that vehicle dynamics studies can be performed and rollover mitigation strategies can be developed. A full vehicle model contains many degrees of freedom and can be difficult to develop. Vehicle simulation software, called TruckSim, is used by many vehicle manufacturers, suppliers, and universities to perform in depth vehicle dynamics studies. This chapter will first develop a two degrees of freedom (DOF) vehicle model, and then look at the TruckSim vehicle model. The purpose of the 2-DOF vehicle model is to use the equations of motion to develop control algorithms, and the purpose of the TruckSim model is to provide an accurate vehicle simulation environment to evaluate the control algorithms.

6.1: Two Degrees of Freedom Vehicle Model

A simple two DOF vehicle model was used to help develop the control laws for vehicle stability control. Figure 6.1 shows a diagram of this model. The two degrees of freedom considered are vehicle yaw rate, *r*, and vehicle lateral velocity, *v*, which are both measured at the vehicle center of gravity (CG). The distance from the front axle to the CG is *a*, and the distance from the rear axle to the CG is *b*. The front tire steer angle is δ_f and the front tire slip angle is α_f. The vehicle forward speed is *u*.

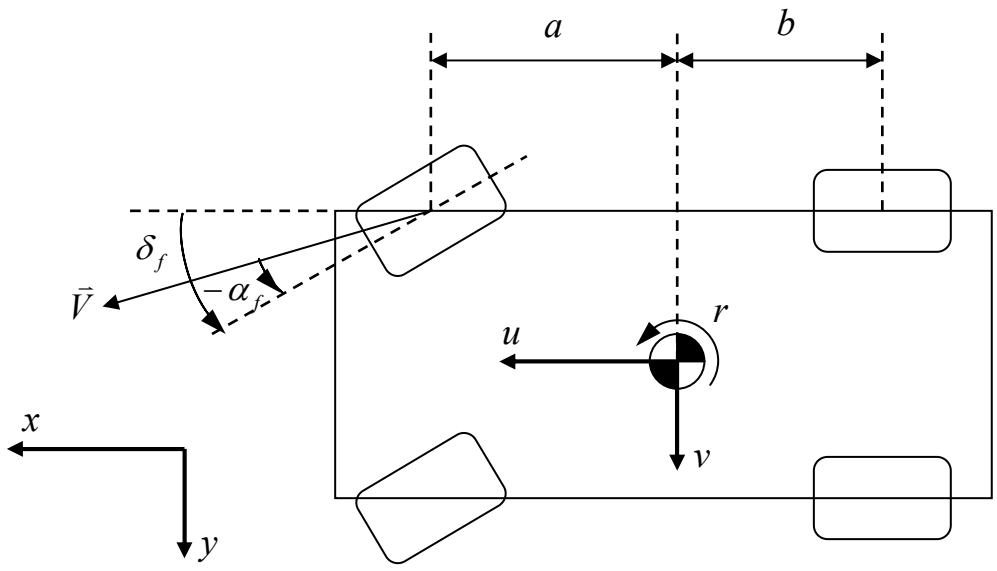

Figure 6.1. Two degree of freedom vehicle model

The following assumptions are made in deriving the equations of motion for the model:

- Same steer angle on front left and front right tires
- No steer angle on rear tires
- Small steer angles and small slip angles
- Same slip angle on both of the front tires and both of the rear tires
- No lateral load transfer, ie., same cornering stiffness for the left and right front tires, and also for the left and right rear tires
- Vehicle forward speed remains constant
- Neglect forces due to inertial effects

The assumption of small slip angles means that the lateral force will be linear with respect to slip angle. Therefore the lateral force can be written as:

$$F_{y-f} = C_{\alpha-f}\alpha_f \tag{6.1}$$

$$F_{y-r} = C_{\alpha-r}\alpha_r \tag{6.2}$$

where $F_{y\text{-}i}$ is the lumped (combined left and right tires) lateral force for the front axle and rear axle, respectively, and $C_{\alpha-i}$ is the lumped cornering stiffness for the front and rear axles, respectively. The slip angle for the front axle is α_f and the slip angle for the rear axle is α_r, which can be determined from Figure 6.2 and Figure 6.3, respectively.

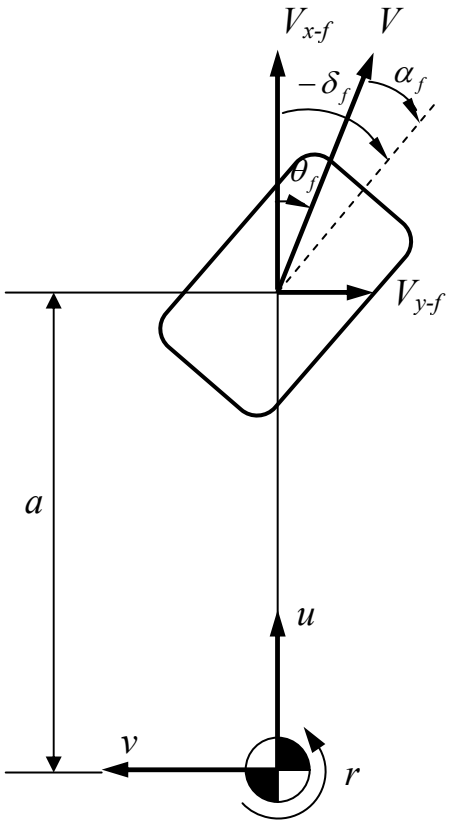

Figure 6.2. Diagram for calculating front tire slip angle

From Figure 6.2 it can be seen that

$$\alpha_f = -\delta_f - \theta_f \tag{6.3}$$

and that

$$\tan\theta_f = \frac{V_{y-f}}{V_{x-f}} \tag{6.4}$$

For the small angle assumption:

$$\theta_f = \frac{V_{y-f}}{V_{x-f}} = \frac{-v - ar}{u} \tag{6.5}$$

Inserting this into equation (6.3) gives

$$\alpha_f = -\delta_f + \frac{v + ar}{u} \tag{6.6}$$

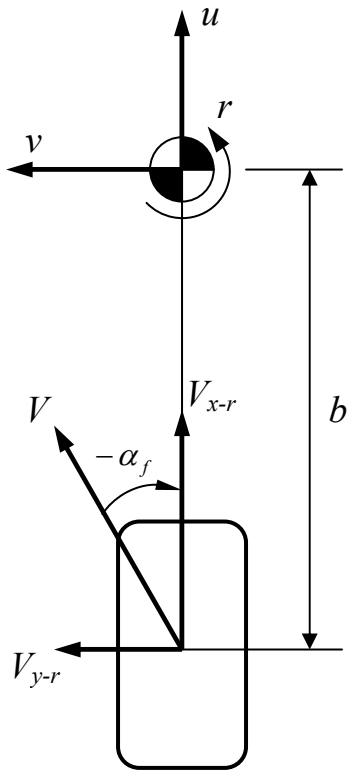

Figure 6.3. Diagram for calculating rear tire slip angle

From Figure 6.3 it can be seen that:

$$\tan\left(-\alpha_f\right)=\frac{V_{y-r}}{V_{x-r}} \tag{6.7}$$

For the small slip angle assumption, it can be written:

$$-\alpha_f=\frac{V_{y-r}}{V_{x-r}} \tag{6.8}$$

$$\alpha_r=\frac{-v-br}{u} \tag{6.9}$$

It can be seen from Figure 6.1 that the accelerations in the x and y direction of the vehicle, measured at the CG, are

$$a_y=\dot{v}+ur \tag{6.10}$$

$$a_x=\dot{u}-vr\,, \tag{6.11}$$

where the overdot denotes a derivative with respect to time.

The equations of motion for the vehicle can then be obtained by using Newton's second law of motion and summing the forces acting on the vehicle in the y direction and summing the moments about the CG of the vehicle. The equations are:

$$\sum F_y=ma_y=F_{y-f}+F_{y-r} \tag{6.12}$$

$$C_{\alpha-f}\left(-\delta_f+\frac{v+ar}{u}\right)+C_{\alpha-r}\left(\frac{-v-br}{u}\right)=m\left(\dot{v}+ur\right) \tag{6.13}$$

$$\sum M_{CG}=I_z\dot{r}=aF_{y-f}-bF_{y-r} \tag{6.14}$$

$$aC_{\alpha-f}\left(-\delta_f+\frac{v+ar}{u}\right)-bC_{\alpha-r}\left(\frac{-v-br}{u}\right)=I_z\dot{r} \tag{6.15}$$

These equations can be written in the form:

$$A\dot{x} + Bx + W = 0\,, \tag{6.16}$$

where

$$x = \begin{bmatrix} v \\ r \end{bmatrix},\ A = \begin{bmatrix} m & 0 \\ 0 & I_z \end{bmatrix},\ B = \begin{bmatrix} \dfrac{C_{\alpha-r} - C_{\alpha-f}}{u} & \dfrac{bC_{\alpha-r} - aC_{\alpha-f}}{u} + mu \\ \dfrac{-aC_{\alpha-f} - bC_{\alpha-r}}{u} & \dfrac{-a^2C_{\alpha-f} - b^2C_{\alpha-r}}{u} \end{bmatrix},\ W = \begin{bmatrix} C_{\alpha-f}\delta_f \\ aC_{\alpha-f}\delta_f \end{bmatrix} \tag{6.17}$$

6.2: TruckSim Vehicle Model

TruckSim vehicle simulation software was used to evaluate the control algorithms developed from the 2-DOF vehicle model. The TruckSim environment allows the user to create a full vehicle model that accurately represents the vehicle dynamics. The user is able to select from a database of existing vehicles and alter the parameters to match those of the studied vehicle. Non-linear mathematical models are available for tires, suspension, aerodynamics effects, frame twist, powertrain, steering, and braking. TruckSim essentially allows the user to specify as many degrees of freedom as necessary for the study being performed. The user can also define three dimensional driving surface geometry and friction. Figure 6.4 shows a screen shot of the main screen where the user can select the vehicle type and specify body type, aerodynamics properties, powertrain information, and also click on other links that lead to specification of tires, suspension, and steering.

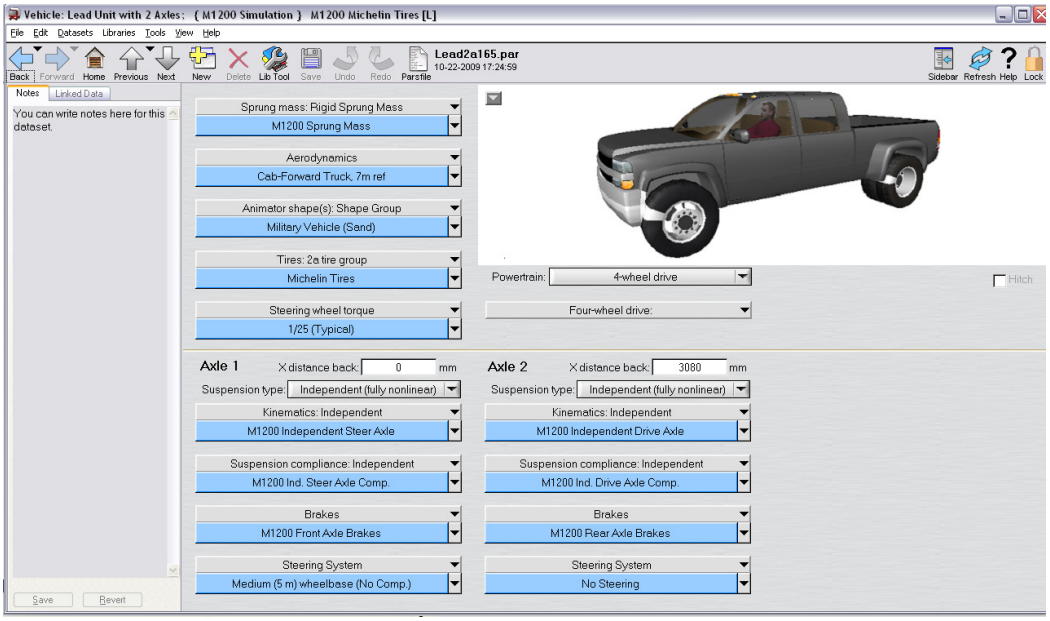

Figure 6.4. TruckSim user interface for specifying vehicle type

If the user clicks on the tires link on the interface in figure 6.4, the interface in figure 6.5 will appear for the user to further define the tire characteristics. Here, the user can set properties such as rolling radius, spring rate, and specifics of the tire force and moment model. The user can decide what force and moment characteristics to include in the tire model, such as longitudinal force vs. slip ratio, and lateral force, aligning moment, and overturning moment as functions of slip angle and camber angle. The tire force and moment characteristics can be specified by a set of Pacejka coefficients or by a set of data points. Figure 6.6 shows the interface where the user can enter data collected from tire force and moment testing, like that described in chapter 3 and chapter 4.

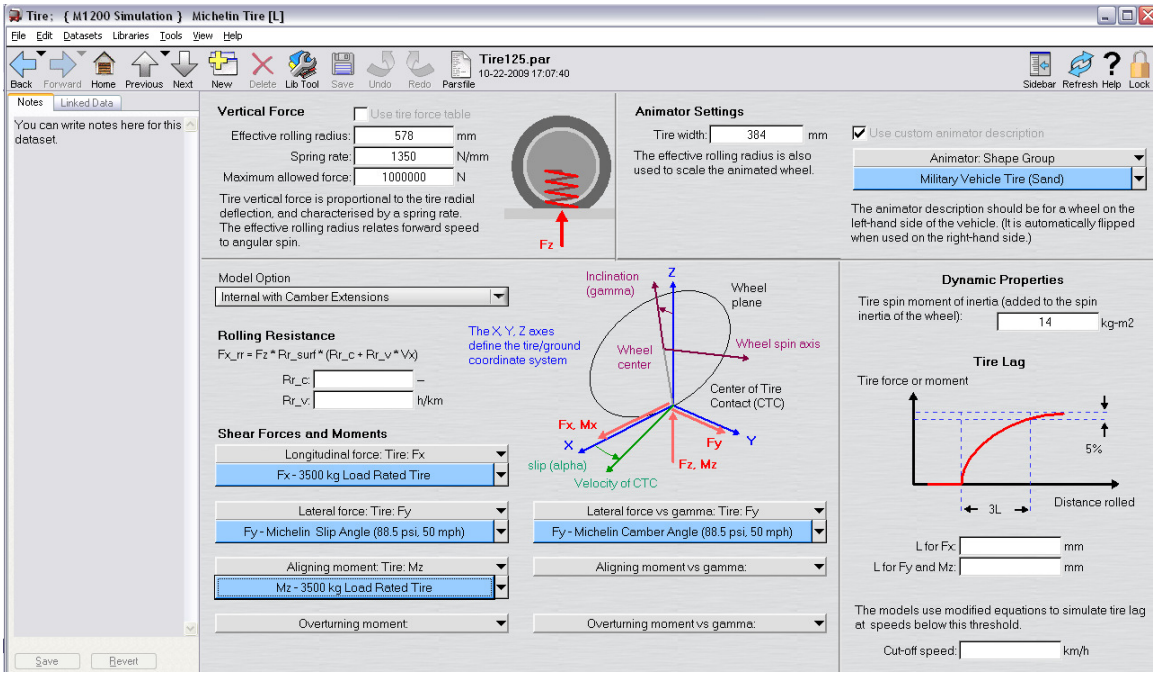

Figure 6.5. TruckSim user interface for specifying tire properties

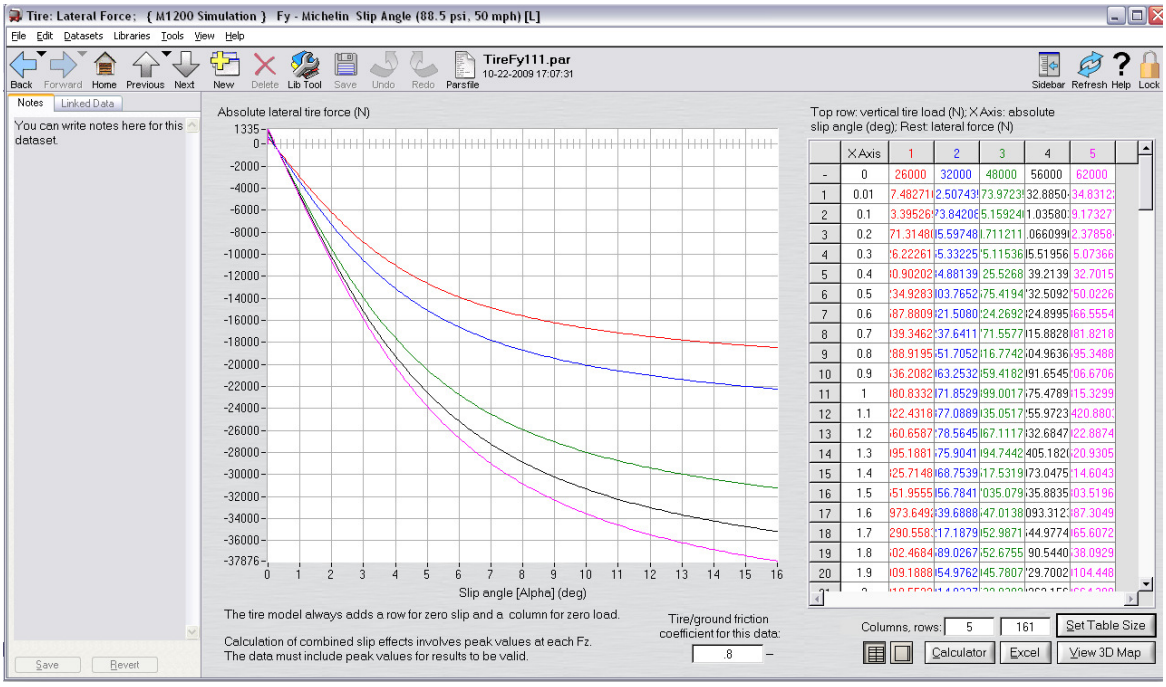

Figure 6.6. TruckSim user interface for providing force and moment tire data

Figure 6.7 shows the main screen for the TruckSim simulation. Here the user can select the driving surface, driving maneuvers, and link TruckSim to other software such as Simulink if desired. TruckSim is able to interface with other software by importing and exporting user selected variable values. This has its advantage in that control algorithms can be developed in Simulink and then tested on the studied vehicle in TruckSim. This can also allow the user to specify a tire model in Simulink and then access it by exporting tire vertical load, slip angle, camber angle, and forward speed from TruckSim to Simulink and importing calculated values of tire forces and moments into TruckSim from Simulink.

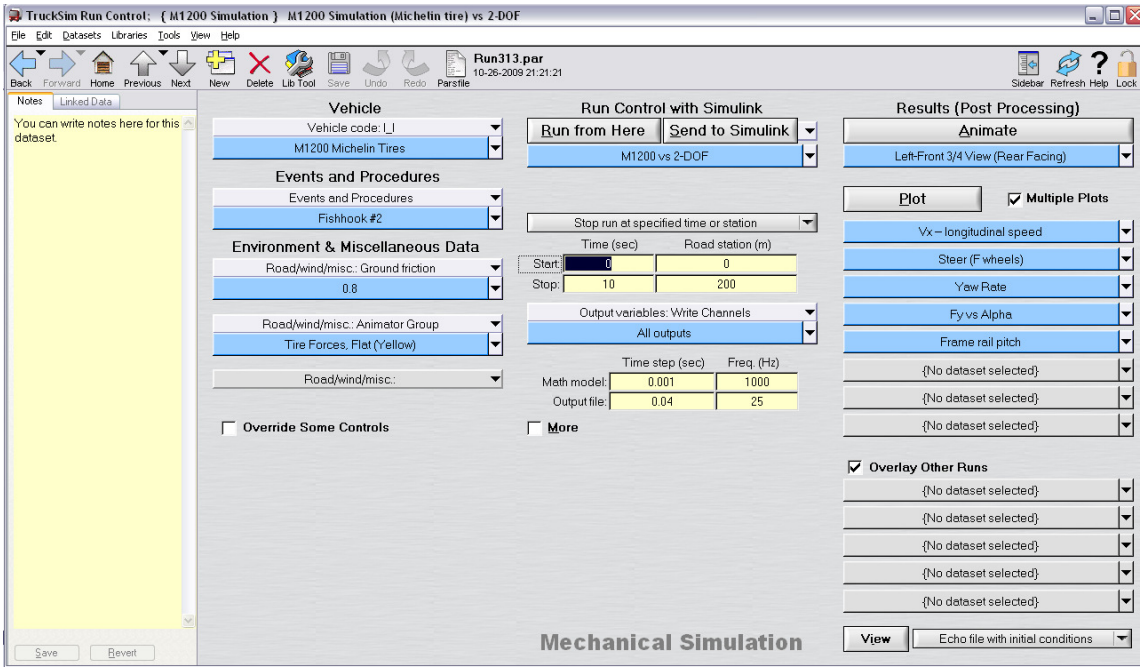

Figure 6.7. TruckSim main screen for selecting vehicle, environment, maneuvers, and external software to link to, such as Simulink

6.3: Comparison of Two Degrees of Freedom Model and TruckSim Model

The 2-DOF model described in section 6.1 was compared to the TruckSim model of section 6.2 to assess the ability of the two degree of freedom model to be used as a basis for developing control laws. A fishhook steer input, as shown in figure 6.8, was given to both vehicles while traveling at a constant forward speed of 25 mph.

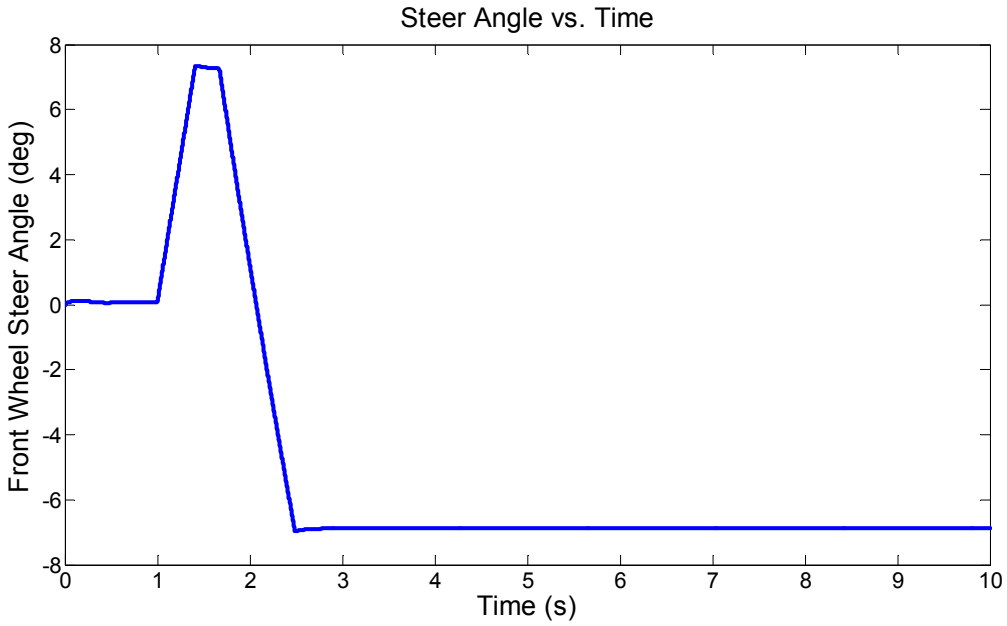

Figure 6.8. Front wheel steer angle vs. time for comparison of TruckSim and 2-DOF models

Since yaw rate and vehicle lateral speed are the state variables chosen for the two degree of freedom model in equation (6.17), yaw rate and lateral speed responses were observed. Figure 6.9 shows a plot of yaw rate vs. time and figure 6.10 shows a plot of lateral speed vs. time for the two models. As can be seen from the plots, the two degree of freedom model matches the TruckSim model fairly well. TruckSim is able to accurately model actual vehicle dynamics because its large library of models and solvers that allows the user to essentially specify as many

degrees of freedom as necessary. Because the two DOF model matches the TruckSim model reasonably well, the two DOF model will be used to develop the control algorithms in the next chapter.

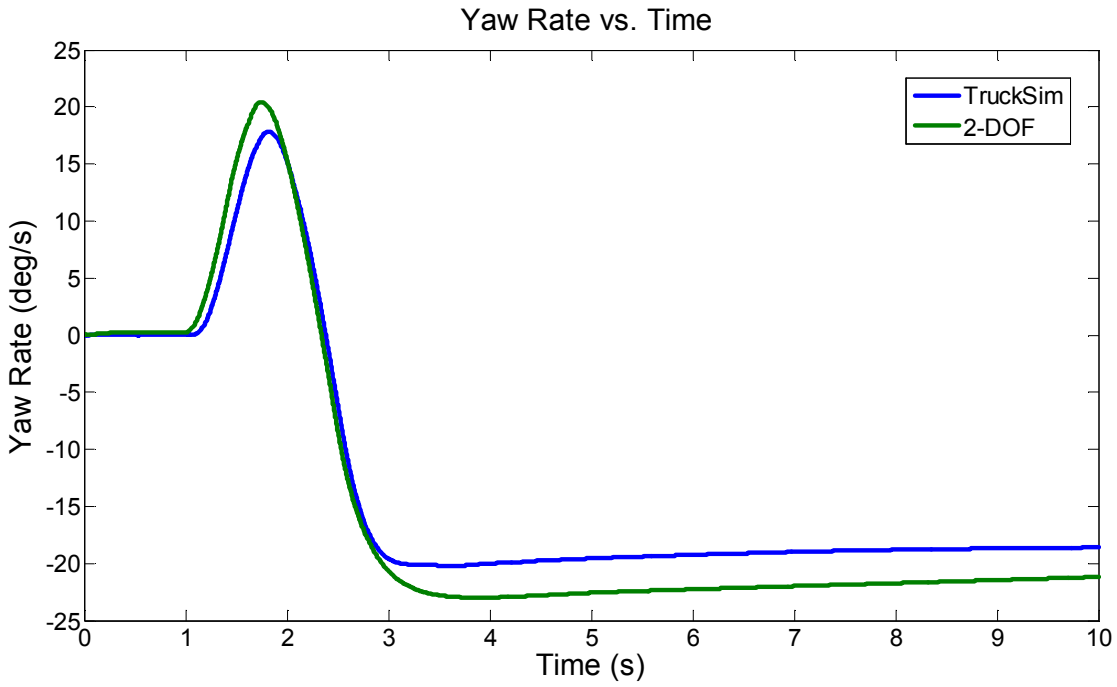

Figure 6.9. Yaw rate vs. time for comparison of TruckSim and 2-DOF models

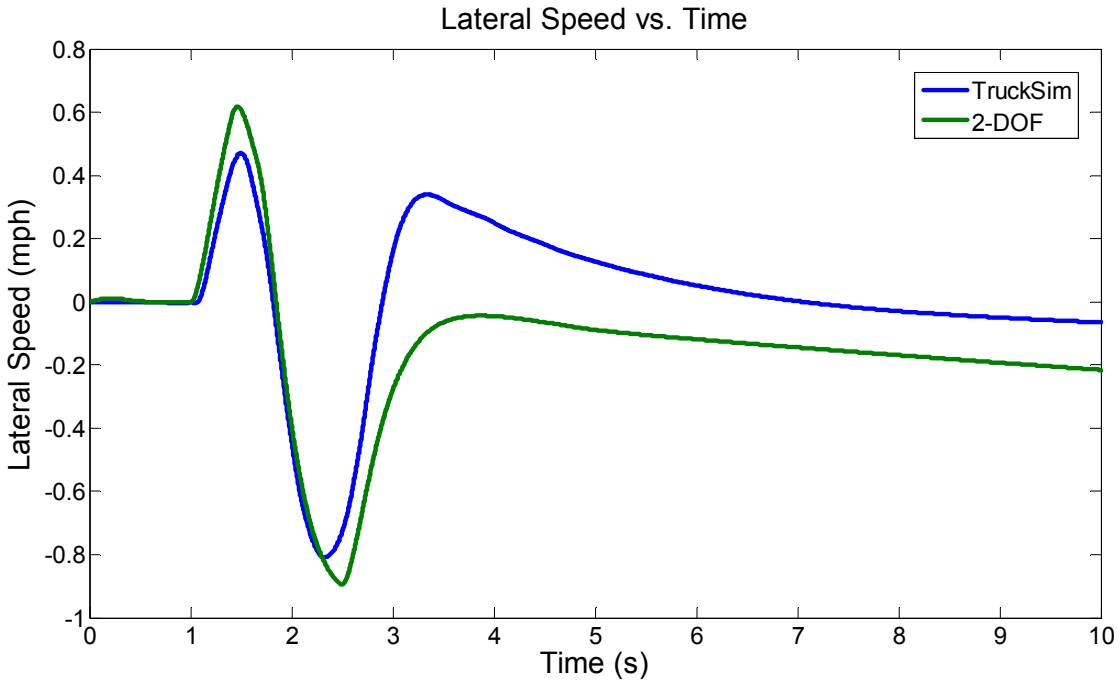

Figure 6.10. Vehicle lateral speed vs. time for comparison of TruckSim and 2-DOF models

The vehicle parameters used for the 2 DOF simulations in figure 6.9 and figure 6.10, and the parameters that will be used in the control laws in chapter 7 are shown in Table 6-1.

Table 6-1. Vehicle parameter values used in 2 DOF model

Vehicle Parameter	Symbol	Value	Units
Mass	m	12,100	kg
Yaw moment of inertia	I_z	61,760	kg-m^2
Length from front axle to CG	a	1.614	m
Length from rear axle to CG	b	1.466	m
Front axle cornering stiffness	$C_{\alpha-f}$	432,010	N/rad
Rear axle cornering stiffness	$C_{\alpha-r}$	466,731	N/rad

6.4: Conclusions

TruckSim vehicle simulation software allows the user to perform vehicle dynamics studies. It is also capable of interfacing with Simulink, allowing vehicle stability control algorithms to be tested. A two degree of freedom vehicle model with vehicle lateral speed and yaw rate as states was developed as a basis for designing control algorithms to improve vehicle roll response. Equivalent forward speed and steer angle trajectories were input into both the TruckSim model and the two degree of freedom model. The two degree of freedom model matched the lateral speed and yaw rate responses of the TruckSim model well. The two degree of freedom model will be used as a basis for developing stability control algorithms, which will then be put into Simulink. The control algorithms in Simulink will be linked to TruckSim to perform vehicle dynamics studies for controlled and uncontrolled vehicles. Development, implementation, and testing of the control algorithms will be discussed in the following chapter.

Chapter 7: Development and Implementation of Stability Control Algorithms for Rollover Prevention on Various Terrains

This chapter will include a discussion of the development, testing, and validation of control algorithms that will help prevent vehicle rollover on a variety of driving surfaces. The physics of vehicle rollovers caused by inertial forces and the striking of obstacles is first examined. The concepts of static stability factor and critical speed are explained, as they play a large role in vehicle rollovers.

Next, a yaw control algorithm is developed based on Lyapunov stability criteria. Because of the coupling between yaw moment and roll moment [21], as well as the increase in vehicle lateral acceleration and lateral speed when a vehicle goes into sliding, direct yaw control (DYC) is important in preventing vehicle rollover. Furthermore, an emergency roll control (ERC) algorithm is developed based on a proposed rollover coefficient [24]. The emergency roll control proves to be beneficial in providing an extra layer of roll protection during potential untripped rollover situations in which maximum braking is already being applied by the DYC.

The DYC and ERC strategies will then be tested by implementing them in a vehicle simulation environment. A series of tests that simulate emergency driving maneuvers are run on the controlled and uncontrolled vehicles driven on dry asphalt. Robustness of the combined DYC and ERC control system is examined by testing the control strategies on simulated off-road terrain. The off-road tire models developed in chapter 5 are used in the vehicle model to simulate vehicle handling on off-road terrain.

7.1: Physics of Untripped Vehicle Rollover

When a vehicle is traveling in a circular path, a centripetal force acts on the tires of the vehicle, forcing the vehicle towards the center of the circular path [17]. This force causes a centripetal acceleration at the vehicle center of gravity. As a result, a centrifugal force acts at the vehicle center of gravity in the direction to the outside of the circular path. An untripped rollover is a rollover that is caused by this centrifugal force. An untripped rollover is not the result of the vehicle striking an obstacle.

Static Stability Factor (SSF) is a commonly used measure of a vehicle's propensity of rollover. The SSF is defined as:

$$SSF = \frac{t_W}{2h_{CG}} \tag{7.1}$$

where t_w is the vehicle track width and h_{CG} is the height of the vehicle's center of gravity. If the entire vehicle is treated as a rigid body with no deflections in the suspension or tires, the SSF is equal to the lateral acceleration in g's that is required to begin vehicle rollover. As a result, knowledge of a vehicle's SSF is helpful in preventing untripped rollovers. It should be noted that although SSF is a good first measure of a vehicle's propensity to rollover, it does not take into account other factors, such as stability control systems, which can greatly reduce a vehicle's risk of rollover. As a result, SSF should not be the only factor examined when accessing a vehicle's likelihood of rollover [20].

7.2: Physics of Tripped Vehicle Rollover

A tripped rollover is defined as a rollover caused by a vehicle striking an obstacle while moving laterally [17]. The two tires (either the two on the left or two on the right) strike an obstacle, such as a curve, which creates a pivot point for the vehicle to roll over. To determine

whether or not a vehicle will roll over when it strikes an object laterally, the critical point is first defined. The critical point is the point at which the vehicle will roll over if there is any lateral velocity when the tire is pivoted about two tires contacting an obstacle. In this case, two of the tires are completely off the ground. The critical velocity is then defined as the velocity that will cause the vehicle to reach its critical point. The critical velocity is defined as:

$$v_{crit} = \left[2g\left(\sqrt{\left(\frac{t_w}{2}\right)^2 + h_{CG}^2} - h_{CG} \right) \right]^{1/2} \tag{7.2}$$

where t_w is the vehicle track width and h_{CG} is the height of the vehicle's center of gravity. If the vehicle is treated as a rigid body with no deflections in the tires or suspension, then the critical speed gives a maximum lateral speed that, if exceeded, will cause the vehicle to roll over if it strikes an object while moving laterally. Critical speeds can typically be as low as 5 mph for sport utility vehicles and can commonly be around 6 mph for sedans.

An understanding of the factors causing tripped and untripped vehicle rollovers is important in developing vehicle stability control systems that can prevent vehicle rollover. In the following sections, stability algorithms are developed and implemented in vehicle simulation software. The concepts of SSF and critical speed show up during these simulations.

7.3: Development of Yaw Controller

A control algorithm using a differential braking strategy was developed in [22] and [23] to stabilize vehicle yaw rate during severe maneuvers. The stability criteria for the controller are based on the definition for stability according to Lyapunov. The system will be locally asymptotically stable if the control law and adaptation law are derived to ensure that the Lyapunov function, $V(x,p,t)$:

- $V(x, p, t) \geq 0$ (positive definite) (1)
- $\dot{V}(x, p, t) < 0$ (negative definite) (2)

that is, for any bounded input to the system, the system will have a bounded output.

The two degree of freedom vehicle model discussed in chapter 6 is used to develop the control law for the direct yaw controller. A control vector, *U*, can be added to the right hand side of equations (6.16) to account for the forces and moments required to stabilize the yaw rate of the vehicle. This gives:

$$A\dot{x} + Bx + W = U\,, \tag{7.3}$$

Where *A*, *B*, *W*, and *x*, are defined in equation (6.17). The control vector is defined as $U = [F_s \; M_s]^T$, where F_s and M_s are the force and moment required to stabilize the system, respectively.

A control algorithm based on Lyapunov direct method was proposed in [22]. This algorithm considers the following candidate Lyapunov function:

$$V(x, p, t) = \frac{1}{2}\left[\tilde{x}^T A\tilde{x} + \tilde{p}^T \Gamma \tilde{p}\right] + \int \tilde{x}^T B\tilde{x}\, dt \tag{7.4}$$

where $\tilde{x} = x - x_d$, $\tilde{p} = p - p_d$, Γ is the adaptation gain matrix, and *A* and *B* are the matrices from equation (7.3). *x* is the state vector consisting of vehicle lateral velocity and vehicle yaw rate. *p* is the adaptation parameter vector that is used to implement adaptive parameters into the controller which will be defined later. The values for *x* and *p* are the actual values for those variables, the subscript *d* denotes a desired value, and the ~ denotes the error, which is the difference between the actual and desired value.

A and *B* are positive definite matrices, so choosing the adaptation gain matrix, Γ, to be a positive diagonal matrix, *V*(*x*,*p*,*t*) will be positive definite. This satisfies the first stability criterion. Taking the derivative of equation (7.4) gives:

$$\dot{V}(x,p,t) = \frac{1}{2}\left[\dot{\tilde{x}}^T A\tilde{x} + \tilde{x}^T A\dot{\tilde{x}} + \dot{\tilde{p}}^T \Gamma\tilde{p} + \tilde{p}^T \Gamma\dot{\tilde{p}}\right] + \tilde{x}^T B\tilde{x} \tag{7.5}$$

Since A and Γ are both diagonal matrices, $\dot{\tilde{x}}^T A\tilde{x} = \tilde{x}^T A\dot{\tilde{x}}$ and $\dot{\tilde{p}}^T \Gamma\tilde{p} + \dot{\tilde{p}}^T \Gamma\tilde{p}$. Equation (7.5) can then be rewritten as:

$$\dot{V}(x,p,t) = \tilde{x}^T A\dot{\tilde{x}} + \tilde{p}^T \Gamma\dot{\tilde{p}} + \tilde{x}^T B\tilde{x} \tag{7.6}$$

The equations of motion can then be implemented into the Lyapunov function to ensure that the control law will stabilize the system. Using $\tilde{x} = x - x_d$ and equation (7.3), the following can be written:

$$A\dot{\tilde{x}} = A\dot{x} - A\dot{x}_d = -Bx - W + U - A\dot{x}_d \tag{7.7}$$

This can be inserted into equation (7.6) to give:

$$\dot{V}(x,p,t) = \tilde{x}^T\left(-Bx - W + U - A\dot{x}_d\right) + \tilde{p}^T \Gamma\dot{\tilde{p}} + \tilde{x}^T B\tilde{x} \tag{7.8}$$

which can be simplified:

$$\dot{V}(x,p,t) = \tilde{x}^T\left(-Bx + B\tilde{x} - W + U - A\dot{x}_d\right) + \tilde{p}^T \Gamma\dot{\tilde{p}} \tag{7.9}$$

and finally:

$$\dot{V}(x,p,t) = \tilde{x}^T\left(-Bx_d - W + U - A\dot{x}_d\right) + \tilde{p}^T \Gamma\dot{\tilde{p}} \tag{7.10}$$

Next, the control law is defined as:

$$U = \hat{A}\dot{x}_d + \hat{B}x_d + \hat{W} - \Lambda\tilde{x} \tag{7.11}$$

where $\tilde{A} = \hat{A} - A$, $\tilde{B} = \hat{B} - B$, $\tilde{W} = \hat{W} - W$, and ^ denotes an estimated value. Inserting equation (7.11) into equation (7.10) gives:

$$\dot{V}(x,p,t) = \tilde{x}^T\left(\hat{B}x_d - Bx_d + \hat{W} - W + \hat{A}\dot{x}_d - A\dot{x}_d - \Lambda\tilde{x}\right) + \tilde{p}^T \Gamma\dot{\tilde{p}} \tag{7.12}$$

which can be simplified as:

$$\dot{V}(x,p,t) = \tilde{x}^T\left(\tilde{A}\dot{x}_d + \tilde{B}x_d + \tilde{W} - \Lambda\tilde{x}\right) + \tilde{p}^T \Gamma\dot{\tilde{p}} \tag{7.13}$$

Now the adaptation law can be implemented, which is:

$$H\tilde{p} = \tilde{A}\dot{x}_d + \tilde{B}x_d + \tilde{W} \tag{7.14}$$

where H is called the adaptation matrix. This can be inserted into equation (7.13) to give:

$$\dot{V}(x, p, t) = \tilde{x}^T \left(H\tilde{p} - \Lambda\tilde{x}\right) + \tilde{p}^T \Gamma \dot{\tilde{p}} \tag{7.15}$$

Rearranging terms gives:

$$\dot{V}(x, p, t) = -\tilde{x}^T \Lambda\tilde{x} + \tilde{p}^T \left(H^T x + \Gamma\dot{\tilde{p}}\right) \tag{7.16}$$

It is desired that $\dot{V}(x, p, t) < 0$ to satisfy criterion 2 and ensure local asymptotic stability. If Λ is a positive diagonal matrix, $-\tilde{x}^T \Lambda\tilde{x}$ will always be negative. Therefore $\tilde{p}^T \left(Hx + \Gamma\dot{\tilde{p}}\right) = 0$ will ensure that equation (7.16) is negative definite. This will hold true if the following equation holds true:

$$\dot{\tilde{p}} = -\Gamma^{-1} H^T \tilde{x} \tag{7.17}$$

Since the two degree of freedom vehicle model uses a linear lateral force tire model and cornering stiffness is not easily measured online, front axle and rear axle cornering stiffness estimates are used as the adaptation parameters. Therefore, $p = [\,\hat{C}_{\alpha-f}\ \hat{C}_{\alpha-r}\,]^{\mathrm{T}}$. Equation (7.14) can then be used to solve for H, which gives:

$$H = \begin{bmatrix} \dfrac{-v_d - ar_d}{u} + \delta_f & \dfrac{v_d + br_d}{u} \\ \dfrac{-av_d - a^2 r_d}{u} + a\delta_f & \dfrac{-bv_d + b^2 r_d}{u} \end{bmatrix} \tag{7.18}$$

This value of H can be used with equation (7.17) to force the front and rear cornering stiffness estimates to converge to the true values. This gives:

$$\hat{C}_{\alpha-f} = -\Gamma_{11}^{-1} \int \left[\left(\frac{-v_d - ar_d}{u} + \delta_f \right)(v - v_d) + \left(\frac{-av_d - a^2 r_d}{u} + a\delta_f \right)(r - r_d) \right] dt + \hat{C}_{\alpha-f,0} \tag{7.19}$$

$$\hat{C}_{\alpha-r} = -\Gamma_{22}^{-1}\int\left[\left(\frac{v_d + br_d}{u}\right)(v - v_d) + \left(\frac{-bv_d - b^2 r_d}{u}\right)(r - r_d)\right]dt + \hat{C}_{\alpha-r,0}, \tag{7.20}$$

where $\hat{C}_{\alpha-f,0}$ and $\hat{C}_{\alpha-r,0}$ are the initial guesses for front and rear cornering stiffness, respectively.

The control law in Equation (7.11) then becomes:

$$U = \begin{bmatrix} \dfrac{\hat{C}_{\alpha-r} - \hat{C}_{\alpha-f}}{u} & \dfrac{b\hat{C}_{\alpha-r} - a\hat{C}_{\alpha-f}}{u} + mu \\ \dfrac{-a\hat{C}_{\alpha-f} - b\hat{C}_{\alpha-r}}{u} & \dfrac{-a^2\hat{C}_{\alpha-f} - b^2\hat{C}_{\alpha-r}}{u} \end{bmatrix}\begin{bmatrix} v_d \\ r_d \end{bmatrix} + \begin{bmatrix} \hat{C}_{\alpha-f}\delta_f \\ a\hat{C}_{\alpha-f}\delta_f \end{bmatrix} - \Lambda\begin{bmatrix} v - v_d \\ r - r_d \end{bmatrix} \tag{7.21}$$

Since there is no way to get a direct lateral force using just braking, it is assumed that $U = [0 \; M_s]^T$. From this, the desired lateral velocity of the vehicle becomes a constraint equation, which is:

$$v_d = \frac{\left(\dfrac{b\hat{C}_{\alpha-r} - a\hat{C}_{\alpha-f}}{u} + mu + \Lambda_{12}\right)r_d + \hat{C}_{\alpha-f}\delta_f - \Lambda_{11} - \Lambda_{12}r}{\dfrac{\hat{C}_{\alpha-f} - \hat{C}_{\alpha-r}}{u} - \Lambda_{11}} \tag{7.22}$$

The desired yaw rate is

$$r_d = \frac{u\delta_f}{(a+b)\left(1 + K_{us}u^2\right)}, \tag{7.23}$$

where K_{us} is the understeer gradient for the vehicle. From equation (7.21), the moment required to stabilize the vehicle is:

$$M_s = \left(\frac{-a\hat{C}_{\alpha-f} - b\hat{C}_{\alpha-r}}{u}\right)v_d + \left(\frac{-a^2\hat{C}_{\alpha-f} - b^2\hat{C}_{\alpha-r}}{u}\right)r_d + a\hat{C}_{\alpha-f}\delta_f - \Lambda_{22}(r - r_d) \tag{7.24}$$

The corrective moment, M_s, is the moment required to stabilize the yaw response of the vehicle. The moment is implemented by braking one of the four wheels. The brake torque corresponding to the required corrective moment is:

$$T_b = \frac{2R_s}{t_w} M_s, \tag{7.25}$$

where R_s is the tire static loaded radius and t_w is the vehicle track width. The selection criteria for choosing the wheel to be braked are shown in Table 7-1. If none of the selection criteria for any of the wheels is met, then no wheel is braked.

Table 7-1. Selection criteria for wheel to be braked

Wheel	r_d	$r - r_d$	M_s
Front right	+	+	–
Rear left	+	–	+
Rear right	–	+	–
Front left	–	–	+

7.4: Development of Emergency Roll Controller

In order to further improve vehicle roll response, an emergency roll controller (ERC) was developed. The purpose of the ERC is to add an extra layer of rollover protection during near rollover situations. In [24], the author proposes a rollover coefficient as a criteria for actuating an emergency rollover prevention technique. The strategy is to have other control algorithms in continuous operation while the emergency control is only activated when the rollover coefficient of the vehicle exceeds some predetermined value. According to the author, this rollover coefficient can be approximated by the equation:

$$R \approx \left(\frac{2h_{CG}}{t_w} \right) \left(\frac{a_{y,s}}{g} \right), \tag{7.26}$$

where R is the rollover coefficient, t_w is the vehicle track width, h_{CG} is the height of the vehicle center of gravity with respect to the ground, $a_{y,s}$ is the lateral acceleration of the sprung mass, and g is the acceleration due to gravity. Comparing this equation to equation (7.1), it can be seen that R is effectively the ratio of the vehicle's current lateral acceleration to the lateral acceleration that would cause the vehicle to rollover in an untripped case. A value of $R = 1$ or $R = -1$ would therefore cause the vehicle to begin to roll over. The user can choose a safety margin and set the reference value $\hat{R}$. If $|R| \geq \hat{R}$, then the emergency roll control is activated. The simulations that will be discussed later in this chapter involve severe emergency maneuvers, therefore a very conservative roll coefficient reference value was chosen ($\hat{R} = 3$).

In this case, the rollover prevention technique for the emergency situation is the activation of hydraulic actuators placed in the suspension of the vehicle. The actuators apply a vertical load to the body of the vehicle on the side of the vehicle that it is rolling towards. This vertical load reduces the roll angle and the lateral acceleration of the body of the vehicle.

7.5: Implementation of DYC and ERC

The purpose of the direct yaw control (DYC) is to stabilize the yaw moment of the vehicle and the purpose of the emergency roll control (ERC) is to reduce the roll angle of the vehicle during emergency situations. DYC is implemented by braking one of the wheels to provide a corrective yaw moment and ERC is implemented by supplying a vertical force to the body of the vehicle by actuators located in the vehicle suspension. Figure 7.1 shows a block diagram of the implementation of these two control algorithms. The block diagram shows that

the two control algorithms operate independent of one another. DYC receives values for vehicle states from onboard sensors to estimate tire cornering stiffness and calculate the yaw moment required to stabilize the vehicle yaw rate. ERC uses values of vehicle states from onboard sensors to calculate a roll coefficient, which determines whether or not to actuate the suspension forces.

The strategy behind equipping the vehicle with DYC and ERC is to constantly stabilize the yaw rate of the vehicle via braking forces with DYC and only activate ERC during emergency situations. The ability of DYC to stabilize the vehicle yaw moment also leads to reductions in vehicle lateral acceleration and vehicle lateral speed, which help in the prevention of untripped rollover and tripped rollover, respectively. ERC is incorporated to add an extra layer of protection in near rollover situations. If a vehicle is performing a severe emergency maneuver and full braking is being applied via DYC, the vehicle may still roll over due to high lateral accelerations that the DYC is not able to prevent. In this case, the ERC is able to further reduce the roll angle of the vehicle to prevent vehicle rollover. In the following sections, simulations of the studied vehicle are carried out for the vehicle equipped with both DYC and ERC, only DYC, and the uncontrolled vehicle. Figures of the Simulink block diagrams of the controllers can be found in Appendix A.

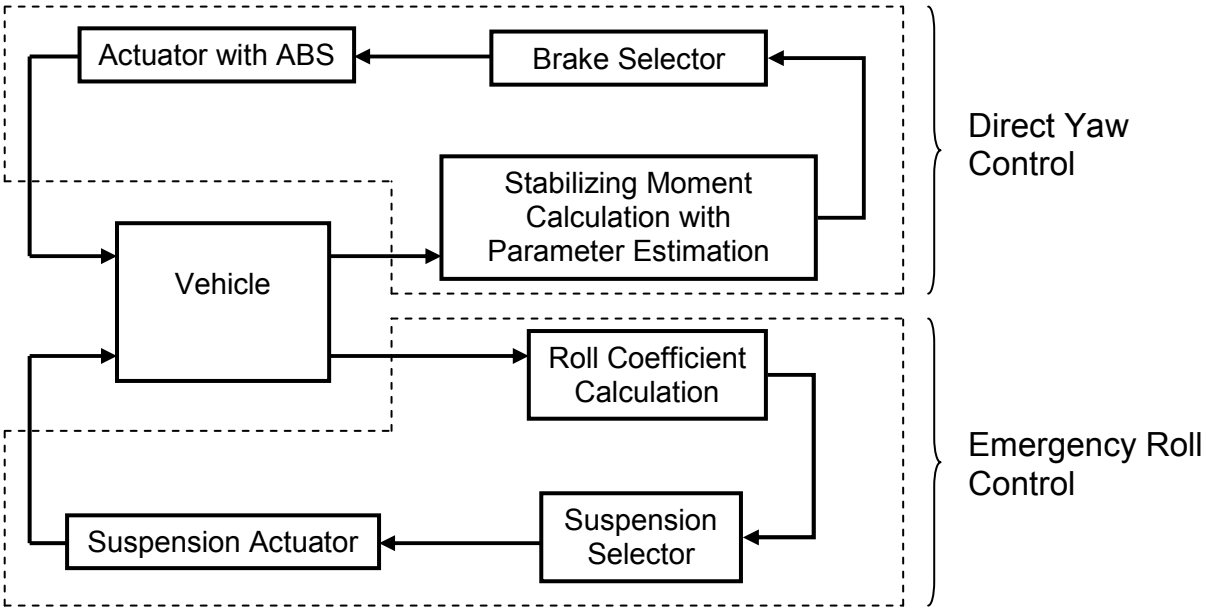

Figure 7.1. Control strategy including direct yaw control and emergency roll control

7.6: Vehicle Simulation of Untripped Rollover on Dry Asphalt

To assess the performance of the proposed control systems, vehicle simulations were run on the studied vehicle for three cases: equipped with DYC and ERC, equipped with DYC, and uncontrolled. The control gain matrix for the DYC is chosen to be

$$\Lambda = \begin{bmatrix} 10^6 & 0 \\ 0 & 10^6 \end{bmatrix} \tag{7.27}$$

In the simulations, a high steer angle, high speed fishhook maneuver is executed in order to simulate an emergency maneuver by the driver during actual driving. The simulations are carried out at a forward speed of 56 mph and a steer input as shown in figure 7.2. For a ten second run, at one second the steering wheel is quickly turned counterclockwise 280 degrees, and then quickly turned clockwise 560 degrees. This steer position is then maintained for the remainder of the run.

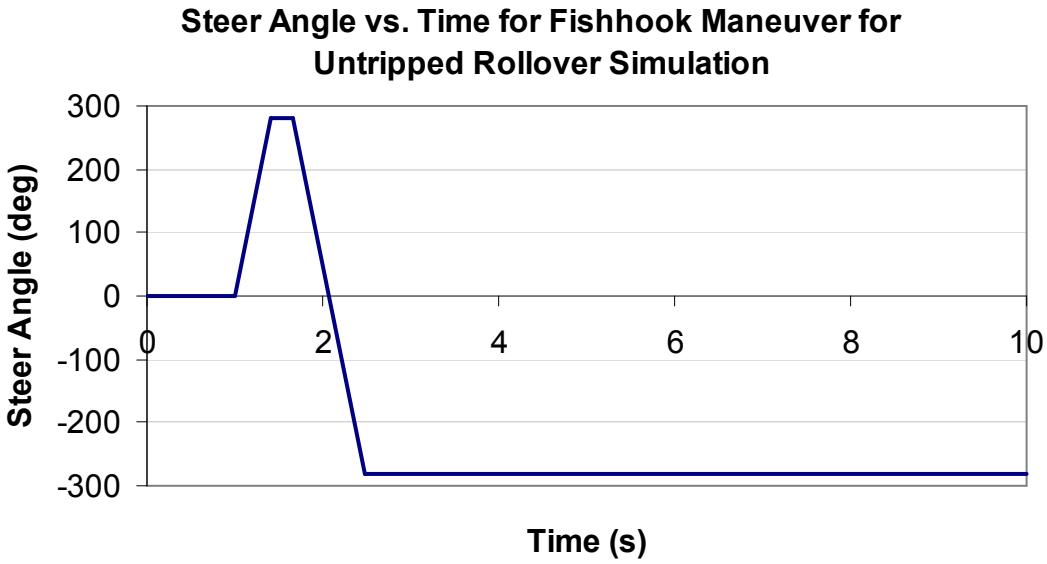

Figure 7.2. Steer angle for fishhook maneuver for untripped rollover study

The fishhook maneuver was performed on all three cases and vehicle yaw rate, lateral acceleration, and roll angle responses were observed. Figure 7.3 shows a plot of lateral acceleration vs. time for all three vehicles. Since the SSF is a measure of the lateral acceleration in g's required to roll a vehicle over in an untripped situation, the positive and negative values of this acceleration are shown in the plot, which is ± 0.891. The vehicle equipped with DYC and ERC stays within the bounds of the SSF for the duration of the simulation. The vehicle equipped with DYC and the uncontrolled vehicle reach lateral accelerations greater than the SSF. The result of this can be seen in figure 7.4. Figure 7.4 shows a plot of vehicle roll angle vs. time for all three situations. Comparing figure 7.3 and figure 7.4, it can be seen that the uncontrolled vehicle reaches a lateral acceleration equal to the SSF of the vehicle around 4.5 seconds, which is around the time that it begins to roll over. Likewise, the lateral acceleration of the vehicle equipped with just DYC exceeds the SSF around 6 seconds, which is when it begins to roll over.

The lateral acceleration of the vehicle equipped with DYC and ERC stays within the bounds of the SSF for the duration of the run and does not roll over.

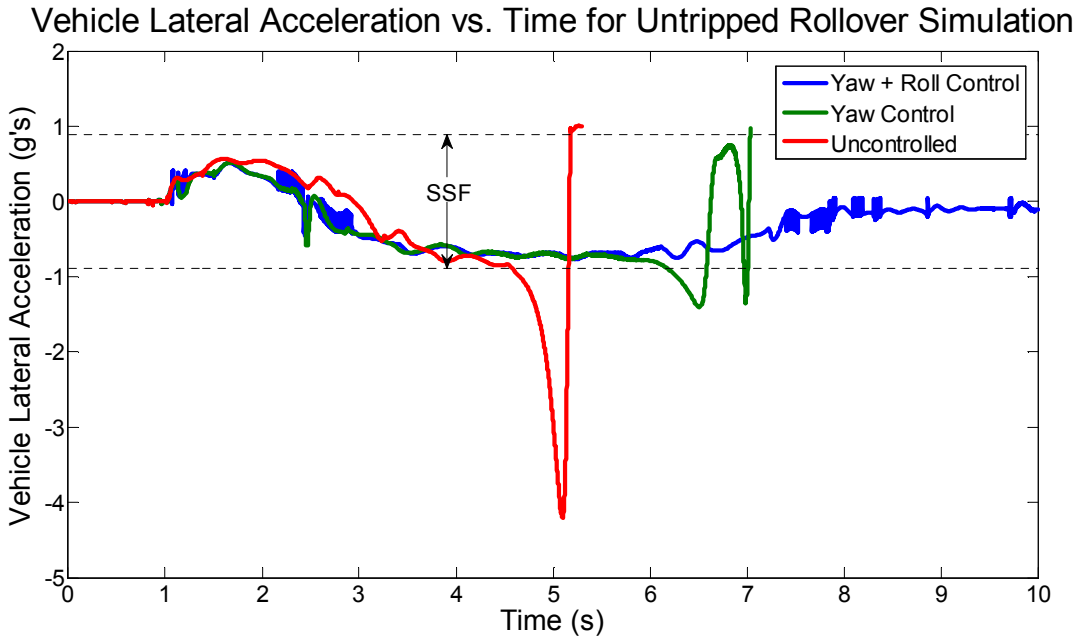

Figure 7.3. Lateral acceleration vs. time for untripped rollover study

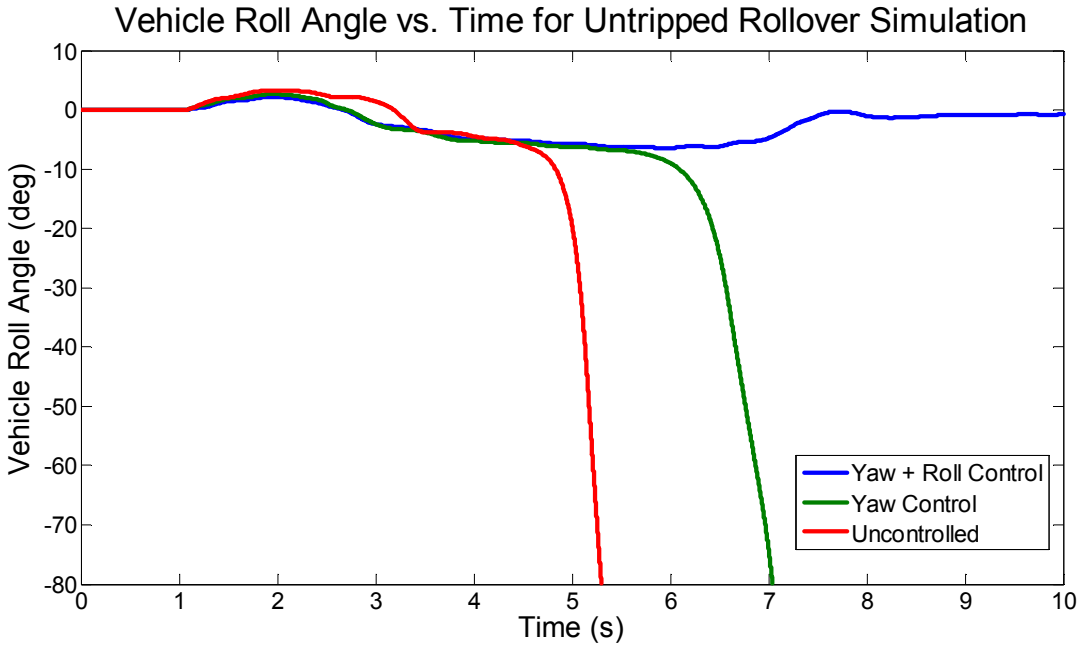

Figure 7.4. Vehicle roll angle vs. time for untripped rollover study

Comparing the three cases where the vehicle is uncontrolled, controlled by DYC, and controlled by DYC and ERC, it can be seen that DYC can greatly reduce a vehicle's lateral acceleration. It should be noted that DYC does not operate on lateral acceleration measurements but on yaw rate measurements. DYC does not directly stabilize a vehicle's lateral acceleration to prevent untripped rollovers, but stabilizes the vehicle's yaw rate. Decreasing the vehicle yaw rate will decrease the vehicle's lateral acceleration which can prevent untripped vehicle rollover during many maneuvers, but does not guarantee prevention of vehicle rollover as it does not take into account the lateral acceleration. The effects of DYC can be seen in a yaw rate vs. time plot, which is shown in figure 7.5. Comparing this plot with the lateral acceleration in figure 7.3, it can be seen that the reduction in vehicle yaw rate due to DYC causes the vehicle lateral acceleration to decrease, helping to prevent vehicle rollover.

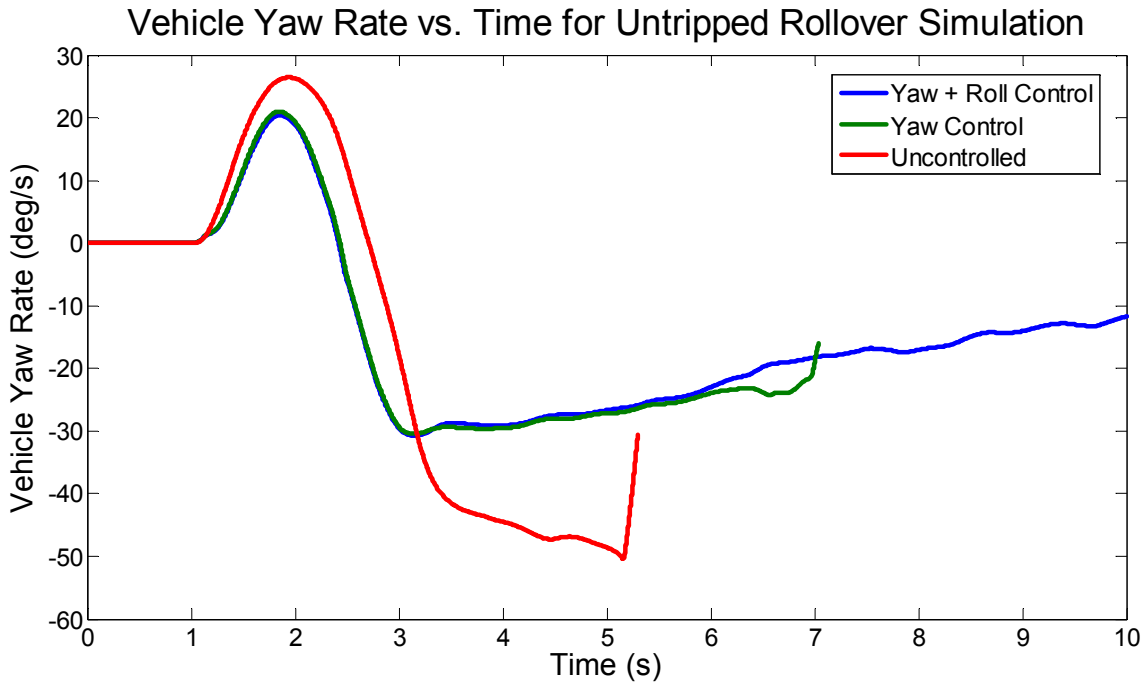

Figure 7.5. Vehicle yaw rate vs. time for untripped rollover study

Figure 7.4 shows that the DYC helps reduce roll angle but does not prevent rollover during the maneuver when it is used as the only stability control system. The addition of ERC to a DYC equipped vehicle further reduces the roll angle of the vehicle in near rollover situations. Figure 7.4 shows that vehicle rollover is prevented in this vehicle by the implementation of both DYC and ERC. In the case of the DYC and ERC equipped vehicle, the ERC provides enough of a counter moment through the activation of actuators in the suspension to reduce the lateral acceleration of the vehicle body. This additional assistance prevents the vehicle from rolling over in a severe situation in which DYC cannot provide any additional control because maximum braking is already being applied.

7.7: Vehicle Simulation of Tripped Rollover on Dry Asphalt

As discussed in section 7.2, vehicle critical speed plays an important role in the case of a tripped rollover. The ERC does not do much to reduce vehicle lateral speed, so only the case of a vehicle equipped with DYC and an uncontrolled vehicle will be studied. For these simulations, the vehicle travels at a constant forward speed of 31 mph and performs a 270 deg fishhook maneuver as shown in figure 7.6. To simulate a tripped rollover scenario, an obstacle is added to the simulation by multiplying the lateral friction coefficient by 20 from four seconds to six seconds.

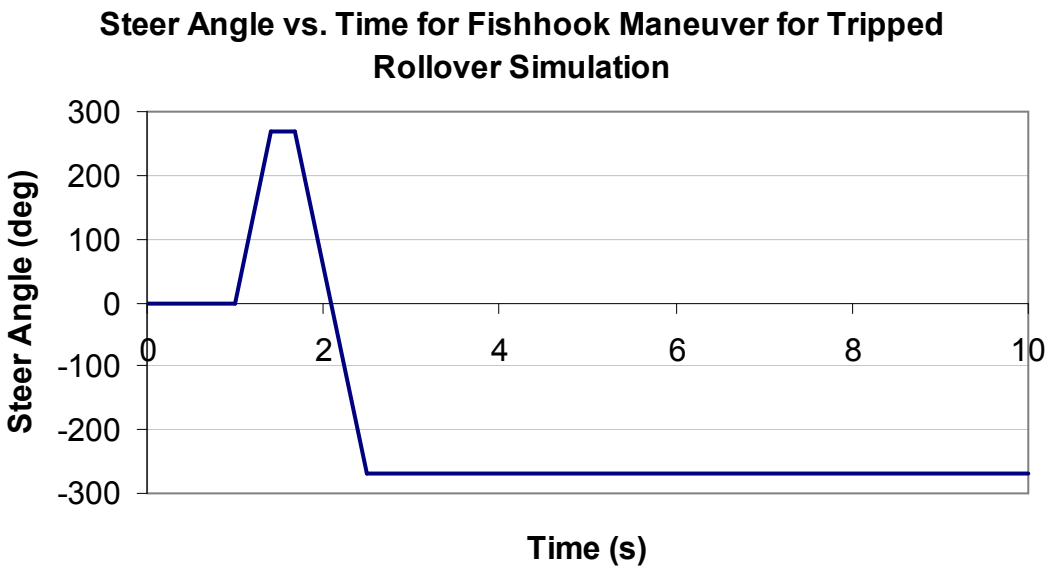

Figure 7.6. Steer angle for fishhook maneuver for tripped rollover study

The direct effect of DYC is shown in figure 7.7. The controlled vehicle consistently maintains yaw rate lower in magnitude than that of the uncontrolled vehicle. The effect of the reduced yaw rate on vehicle lateral velocity can be seen in figure 7.8. Figure 7.8 also shows the positive and negative critical speed of the studied vehicle with the dashed red line, which is at ± 2.55 m/s. The DYC causes a reduction in the lateral velocity of the vehicle and causes the vehicle to stay within the critical speed bounds. At four seconds when the obstacle is encountered, the controlled vehicle has a lateral velocity of about 0.2 m/s which is below the critical speed, and the uncontrolled vehicle has a lateral velocity of 7.4 m/s which is well above the critical speed. As stated in section 7.2, it is expected that a vehicle will roll over when the vehicle strikes an obstacle while moving laterally at a speed greater than the critical speed. This is the case for this simulation, as shown in the roll angle vs. time plot of figure 7.9. When the uncontrolled vehicle strikes the obstacle at four seconds, the vehicle immediately begins to roll over.

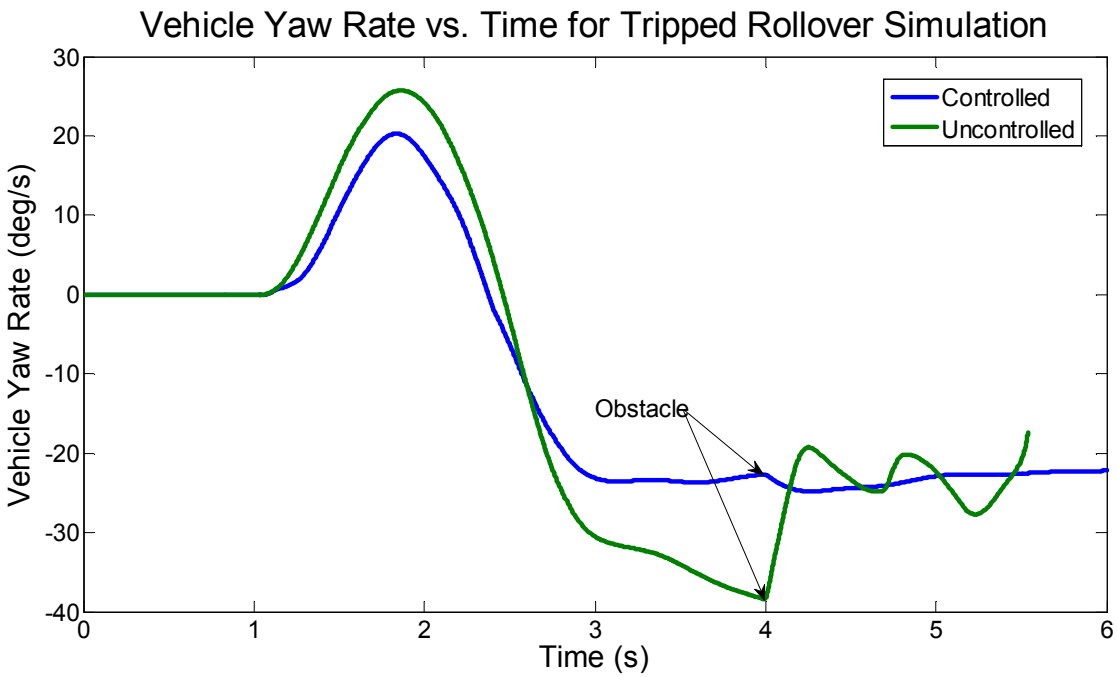

Figure 7.7. Yaw rate vs. time for tripped rollover simulation

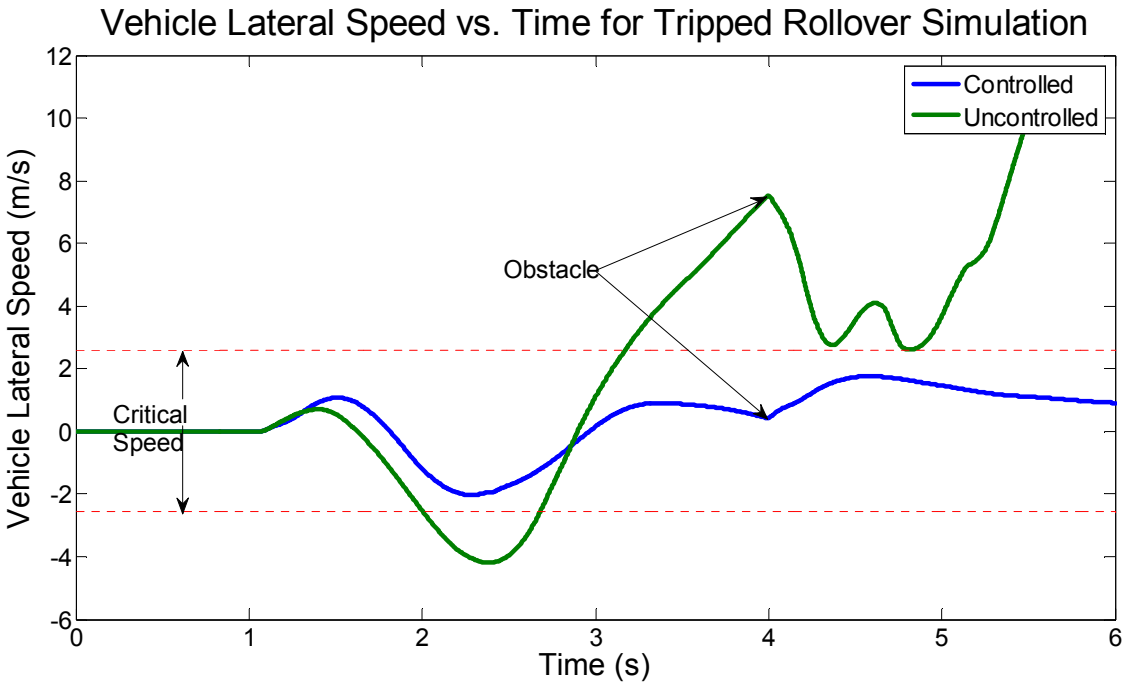

Figure 7.8. Vehicle lateral speed vs. time for tripped rollover simulation

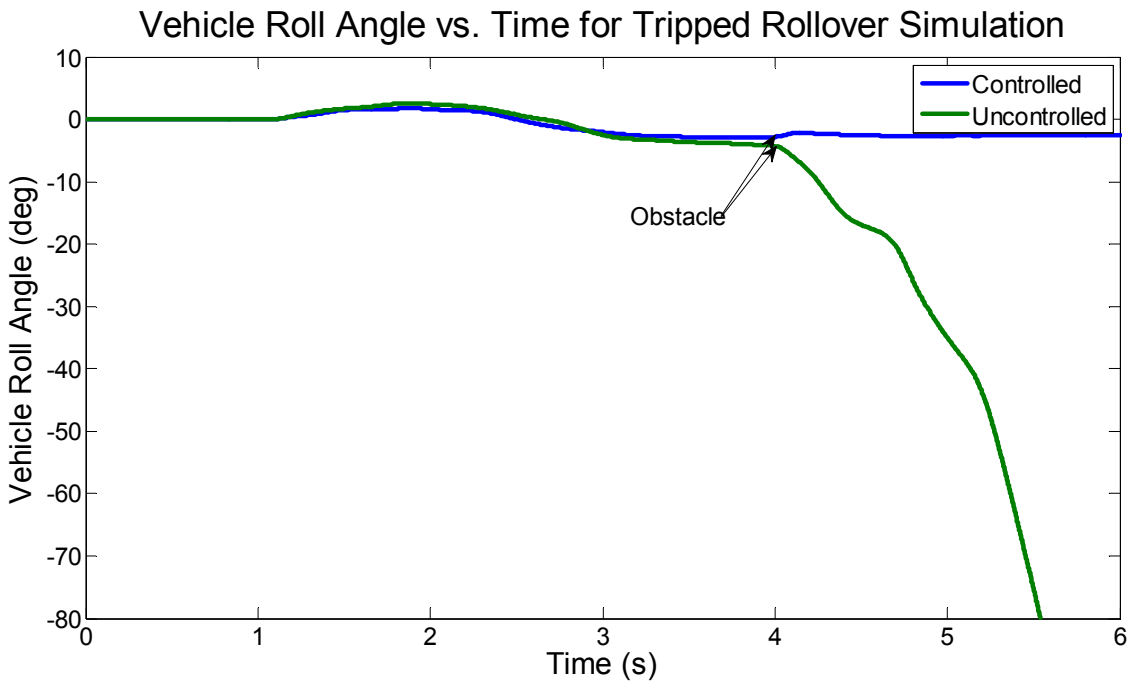

Figure 7.9. Vehicle roll angle vs. time for tripped rollover simulation

It should be noted that the DYC is not able to detect an impending obstacle and is therefore not able to directly "prepare" for a tripped rollover. The stabilizing of the yaw rate does, however, decrease the lateral speed of the vehicle and is able to help prevent a tripped roll over in some situations, including this simulation.

7.8: DYC and ERC Simulations on Off-Road Terrain

The off-road tire model for dirt and gravel developed in Chapter 5 was used in vehicle simulations to assess the performance of the DYC and ERC control strategies. Since the studied vehicle will constantly be driving on different surfaces, it is important that the controllers are able to adapt to the different surfaces. Choosing tire cornering stiffness as the adaptive parameter in the DYC, as discussed in section 7.3, will allow the controller to account for different driving surfaces [23]. Also, the ERC is activated based on the value of the rollover

coefficient of equation (7.26), which is a function of three parameters that are assumed to be constant (track width, CG height, and acceleration due to gravity) and one variable, the lateral acceleration of the sprung mass. As a result, the ERC is also able to accomodate different driving surfaces.

To assess the ability of the combined DYC and ERC system to operate on multiple driving surfaces, untripped rollover simulations like those described in section 7.4 were carried out on a vehicle equipped with both DYC and ERC and an uncontrolled vehicle. The vehicle traveled with a constant forward speed of 56 mph with a steer input as shown in figure 7.2. These simulations were performed on both dirt and gravel driving surfaces. This was simulated by including the off-road lateral force tire model for dirt and gravel from chapter five in the vehicle simulation software. Other tire force and moment properties were automatically adjusted by the software through the specification of the friction coefficient between the tires and ground. The friction values were calculated by multiplying the peak value scaling factor times the friction coefficient for dry asphalt (the baseline). The friction coefficient for the simulated dirt surface is $\mu_{\text{dirt}} = 0.458$ and the friction coefficient for the simulated gravel surface is $\mu_{\text{gravel}} = 0.392$.

The results for the untripped rollover simulation on dirt are shown in figure 7.10 – 7.12. Figure 7.10 shows a plot of yaw rate vs. time. The DYC reduces the yaw rate on the controlled vehicle. The DYC is able to effectively do this without changing the gain matrix of equation (7.27) because of the use of tire cornering stiffness as the adaptive parameters in the control algorithm. The effect of reduced yaw rate from the DYC on vehicle lateral acceleration is shown in the lateral acceleration vs. time plot of figure 7.11. Furthermore, activation of the ERC can also be seen in the spikes of lateral acceleration change in the plot. Although the spikes due ERC activation cause quick changes in the lateral acceleration of the vehicle, which can be felt

by the driver and may be uncomfortable, the ERC does additionally reduce the roll angle of the vehicle. The combined effort of the DYC and ERC on the controlled vehicle is seen in the roll angle vs. time plot of figure 7.12. The controlled vehicle remains stable while the uncontrolled vehicle rolls over.

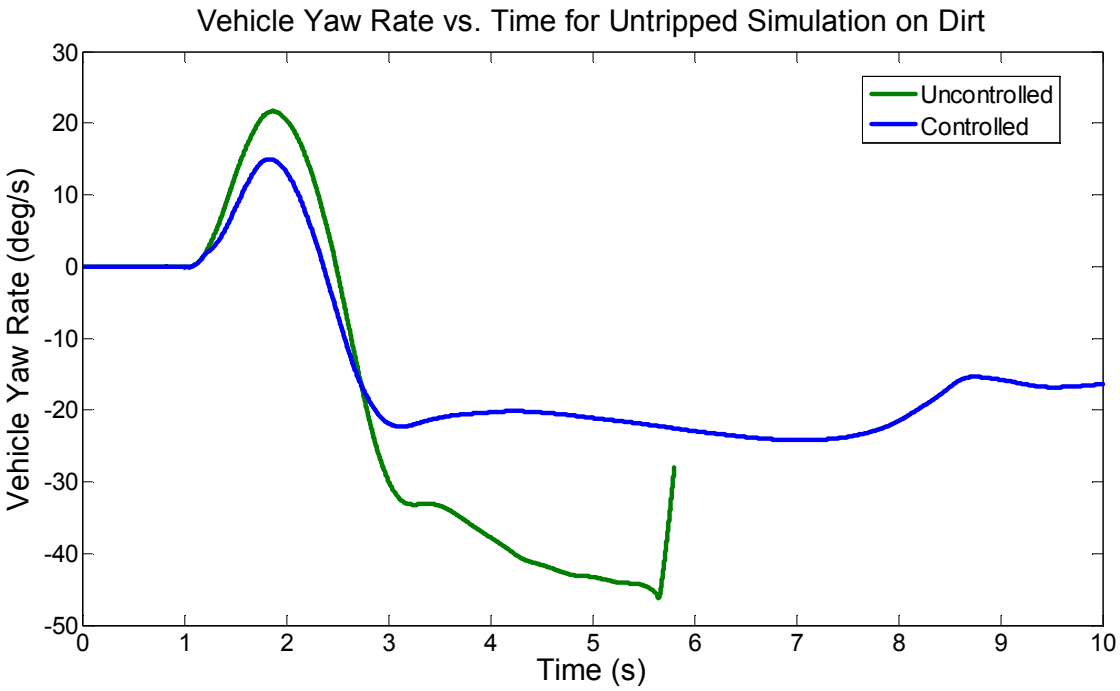

Figure 7.10. Vehicle yaw rate vs. time for untripped rollover simulation on dirt

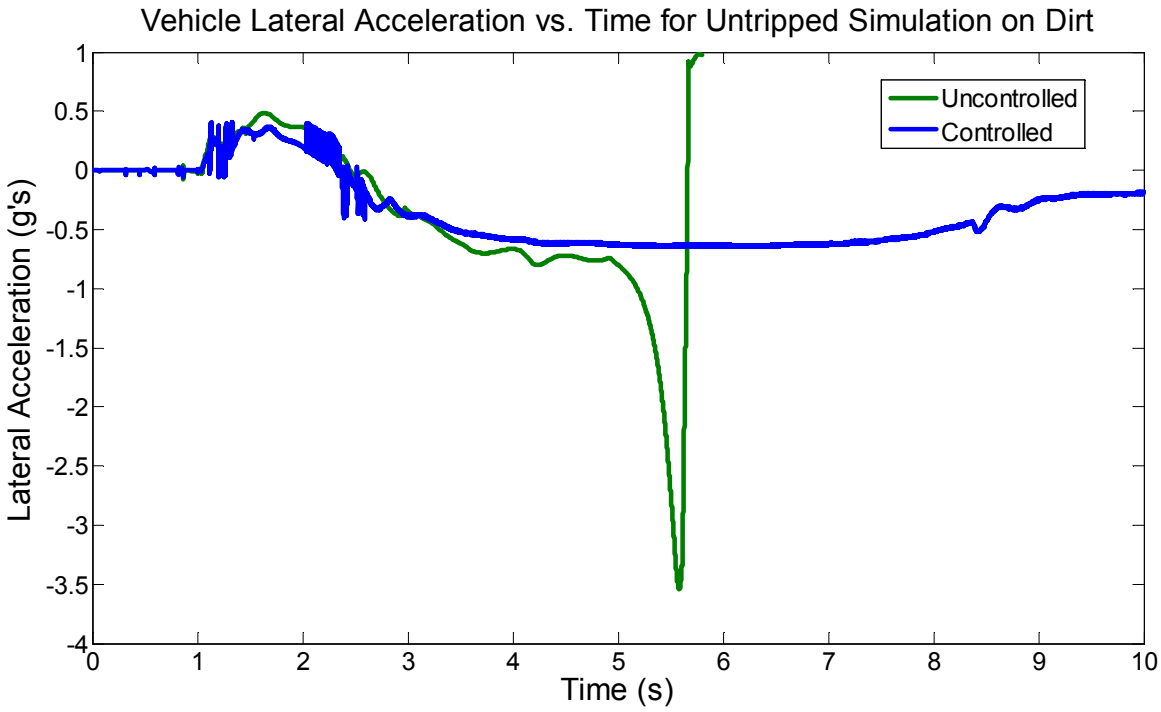

Figure 7.11. Vehicle lateral acceleration vs. time for untripped rollover simulation on dirt

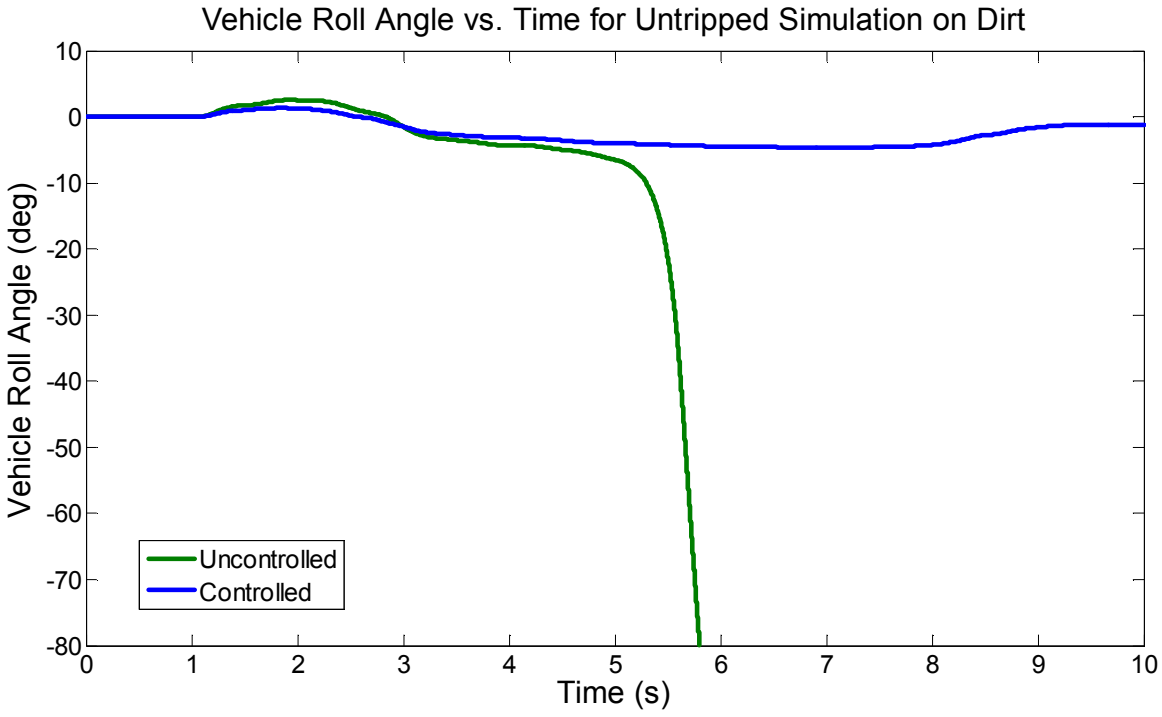

Figure 7.12. Vehicle roll angle vs. time for untripped rollover simulation on dirt

The ability of the combined DYC and ERC control system to operate on various driving surfaces is further shown by the results of the untripped rollover simulation on gravel, shown in figure 7.13 – 7.15. The yaw rate vs. time plot of figure 7.13 shows that the DYC reduces the yaw rate, and therefore the lateral acceleration as well, of the controlled vehicle driven on gravel. The ERC further reduces the roll angle of the vehicle. The controlled vehicle remains stable while the uncontrolled vehicle rolls over.

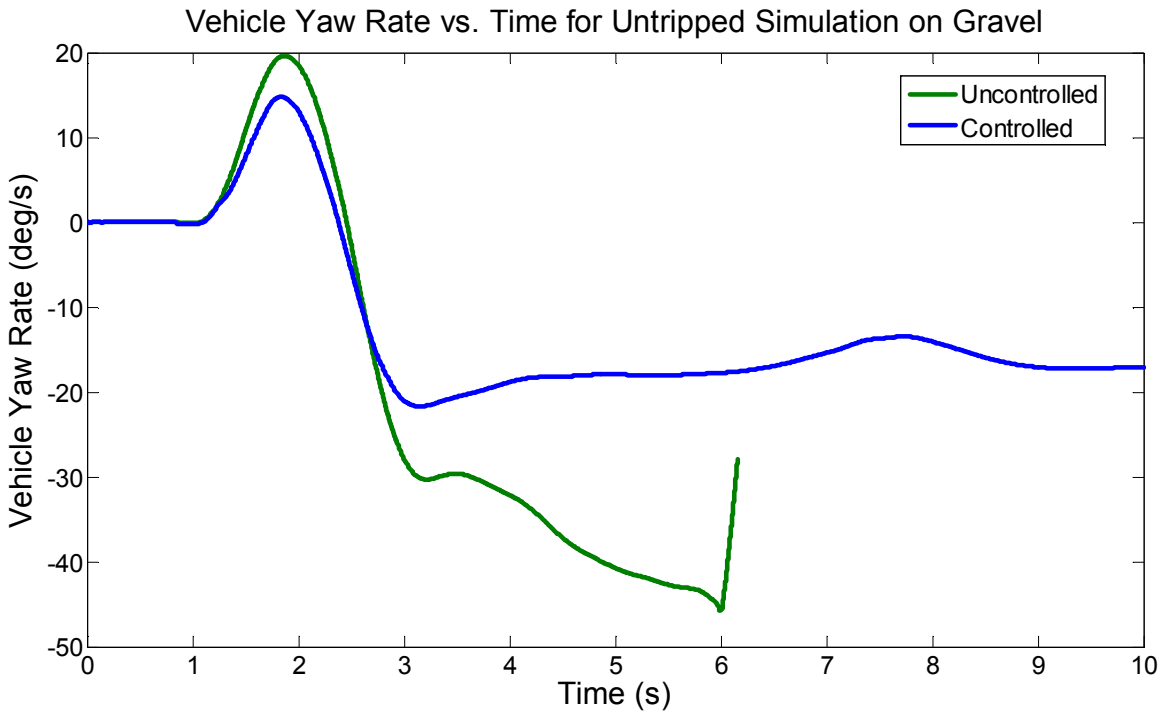

Figure 7.13. Vehicle yaw rate vs. time for untripped rollover simulation on gravel

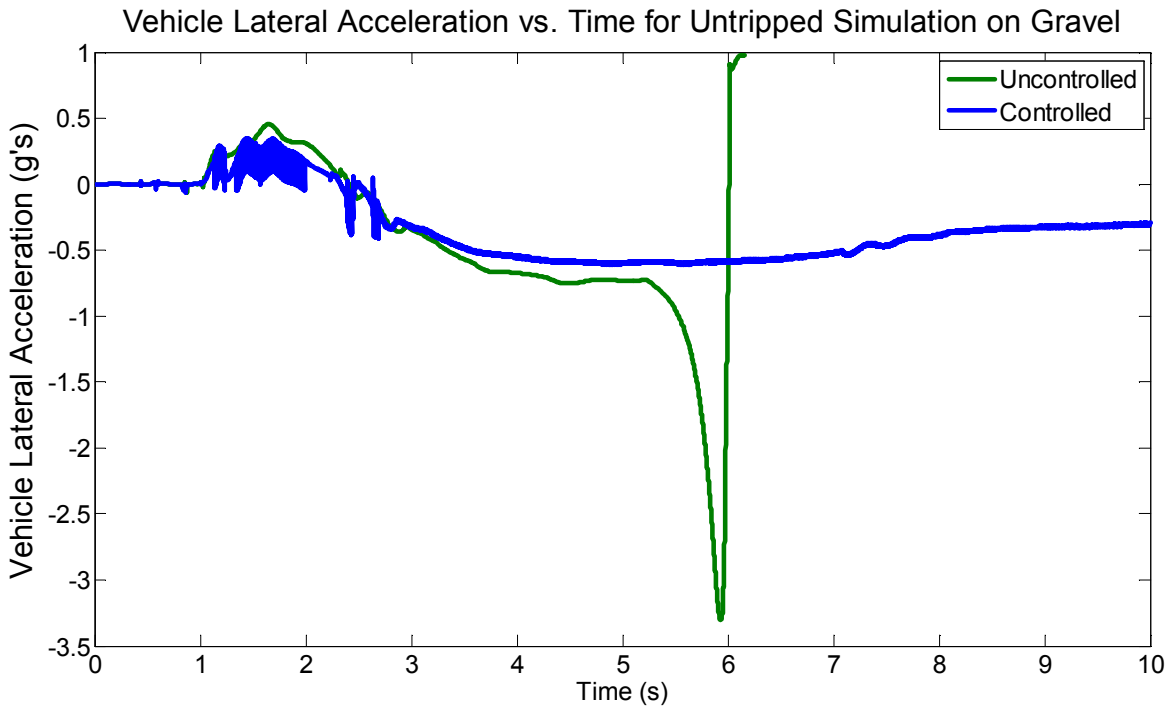

Figure 7.14. Vehicle lateral acceleration vs. time for untripped rollover simulation on gravel

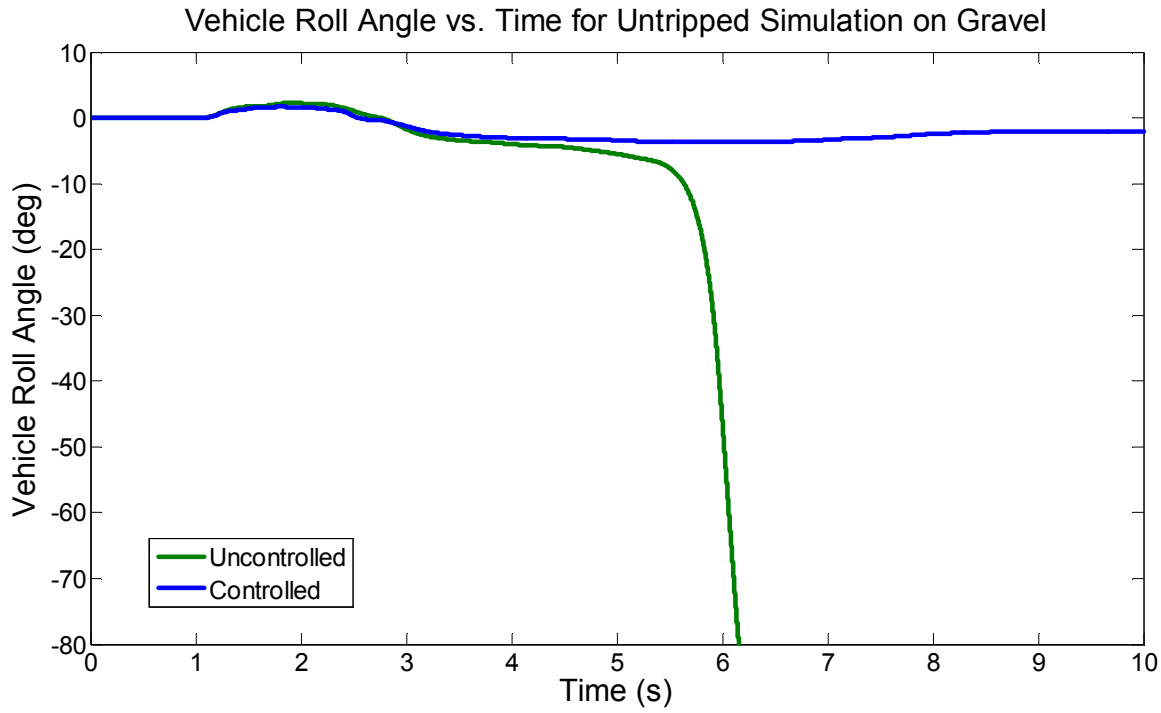

Figure 7.15. Vehicle roll angle vs. time for untripped rollover simulation on gravel

7.9: DYC Cornering Stiffness Estimation

During the simulations, the DYC algorithm calculates estimates for the cornering stiffness of the front and rear axles using equations (7.19) and (7.20), respectively. Figures 7.16 – 7.19 show the cornering stiffness estimates for a 25 mph, 180 deg. fishhook maneuver on dry asphalt and dirt. For all simulations it was assumed that no knowledge of cornering stiffness existed, therefore the initial guesses were chosen to be 0 N/rad. The actual initial values of cornering stiffness are plotted as a dashed line and are shown in table 7-2.

Table 7-2. Actual initial values of front and rear cornering stiffness for dry asphalt and dirt

Driving Surface	$C_{\alpha-f}$ (N/rad)	$C_{\alpha-r}$ (N/rad)
Dry Asphalt	432,000	466,700
Dirt	298,100	322,000

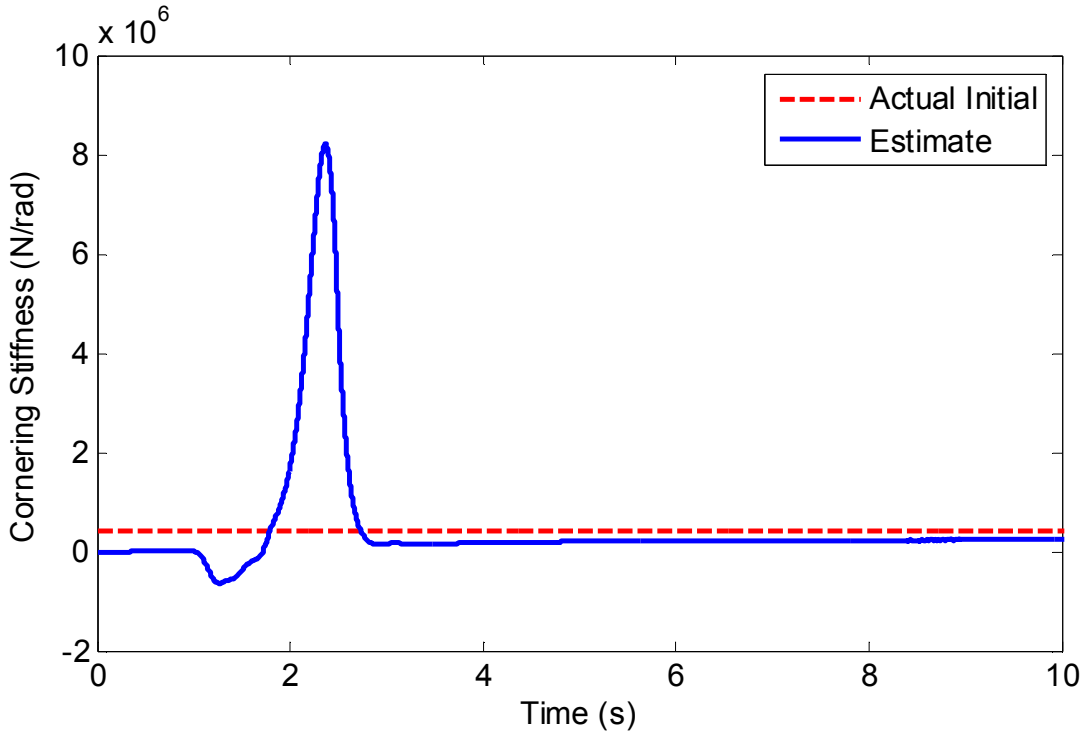

Figure 7.16. Front axle cornering stiffness estimation for vehicle driven on dry asphalt

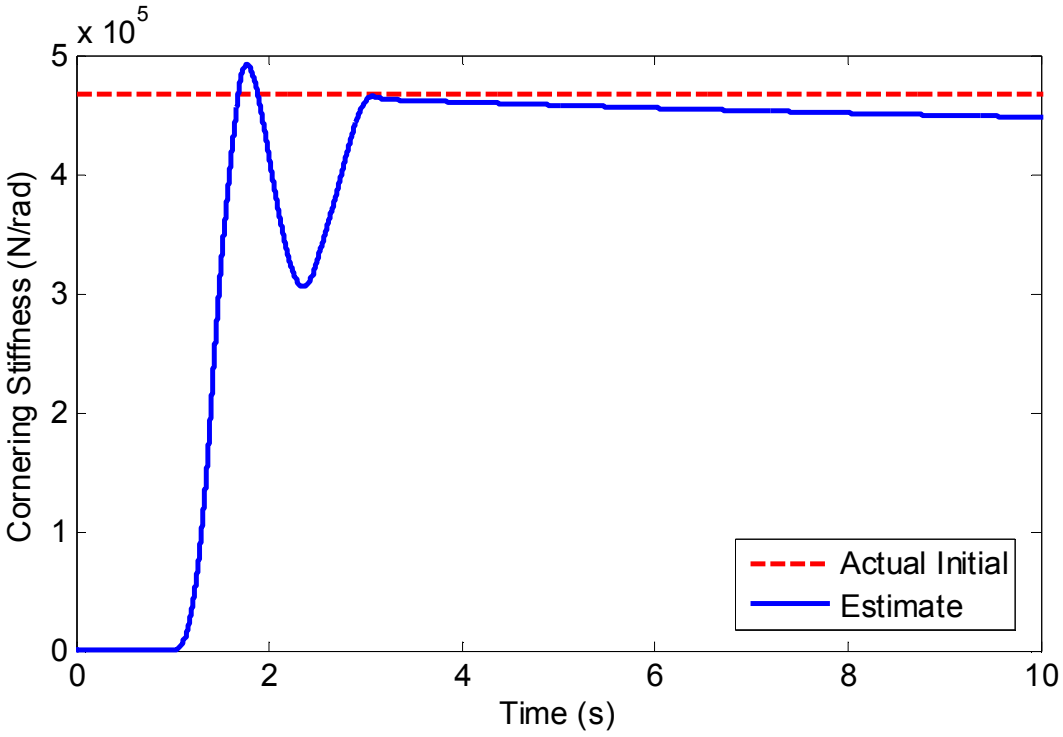

Figure 7.17. Rear axle cornering stiffness estimation for vehicle driven on dry asphalt

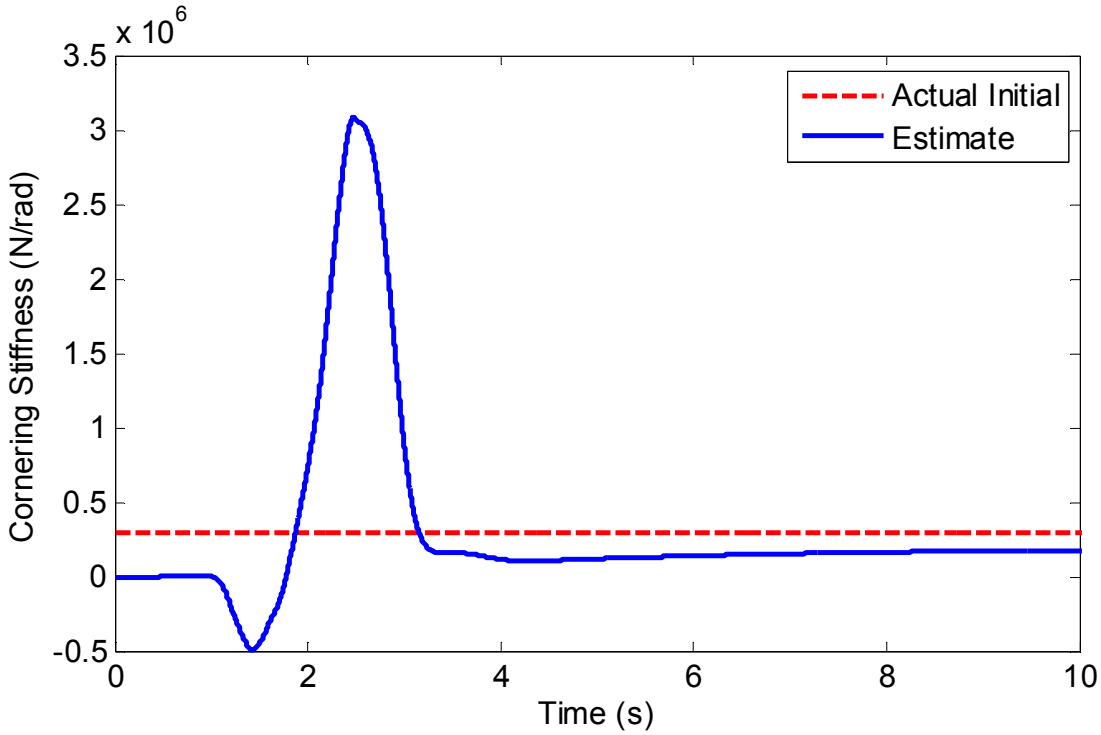

Figure 7.18. Front axle cornering stiffness estimation for vehicle driven on dirt

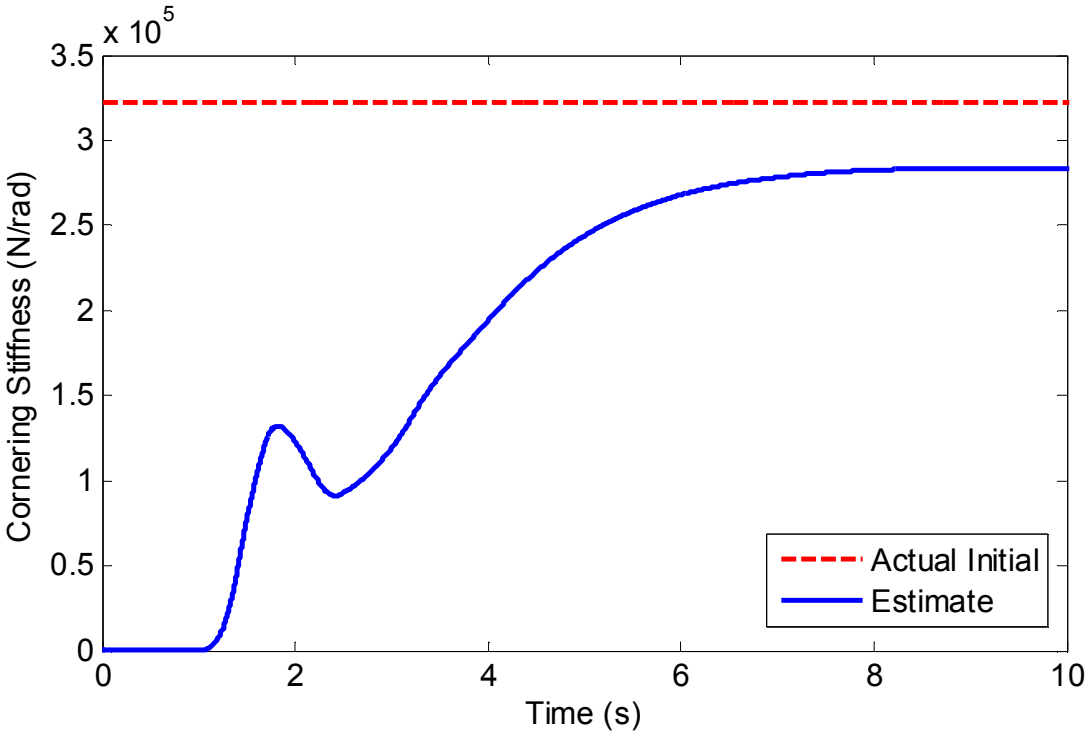

Figure 7.19. Rear axle cornering stiffness estimation for vehicle driven on dirt

With the exception of the rear axle for dry asphalt, for the selected adaptation gains for each simulation, the adaptation law causes the cornering stiffness estimates to converge to values close to the actual values. The values in the adaptation gain matrix, Γ, were changed for each driving surface. No significant study was performed on gain tuning for various driving surfaces, however, for figure 7.16 – 7.19, the gains used for the dirt simulation were 20% of the value of the gains used for the dry asphalt simulation. The values used in the adaptation gain matrix for dry asphalt and dirt are shown in table 7-3. Since Γ is a diagonal matrix, $\Gamma_{12} = \Gamma_{22} = 0$.

Table 7-3. Adaptation gains used for cornering stiffness estimation on dry asphalt and dirt

Driving Surface	Γ_{11}^{-1}	Γ_{22}^{-1}
Dry Asphalt	5×10^{9}	5×10^{7}
Dirt	1×10^{9}	1×10^{7}

7.10: DYC and ERC Control Power

Figures 7.20 and 7.21 show the control power required from the brakes for DYC and the power required from the actuators for ERC for the dirt simulation of section 7.9. The DYC will brake one wheel at a time according to the braking strategy in table 7-1, and will apply a brake torque to that wheel according to equation (7.25). Figure 7.20 shows the brake torque applied to each of the four wheels over the course of the simulation. The maximum possible torque that can be applied to the front and rear wheels is 7,500 N m and 10,000 N m, respectively. The plots show full-braking being applied to the rear right wheel for the last two seconds of the simulation which includes flutter due to anti-lock brakes.

Figure 7.21 shows the force applied to the vehicle body by hydraulic actuators located near the suspension. The necessary actuators apply an upward force of 6000 N when the roll coefficient is exceeded in its respective direction and apply no force when the roll coefficient is not exceeded. At approximately 2.8 seconds until the end of the run the front and rear actuators on the left side apply a constant upward force of 6000 N to the vehicle body.

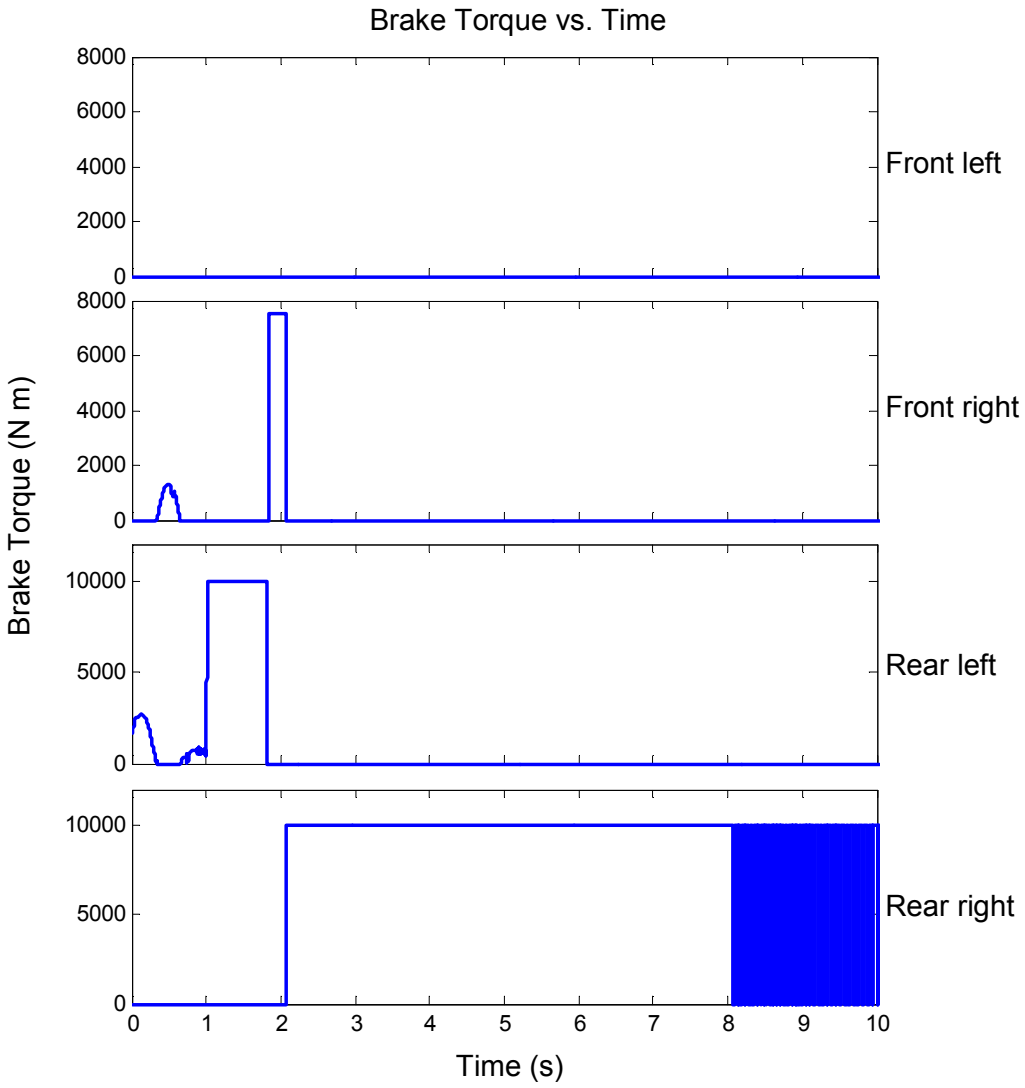

Figure 7.20. Brake torque vs. time from DYC for simulation on dirt

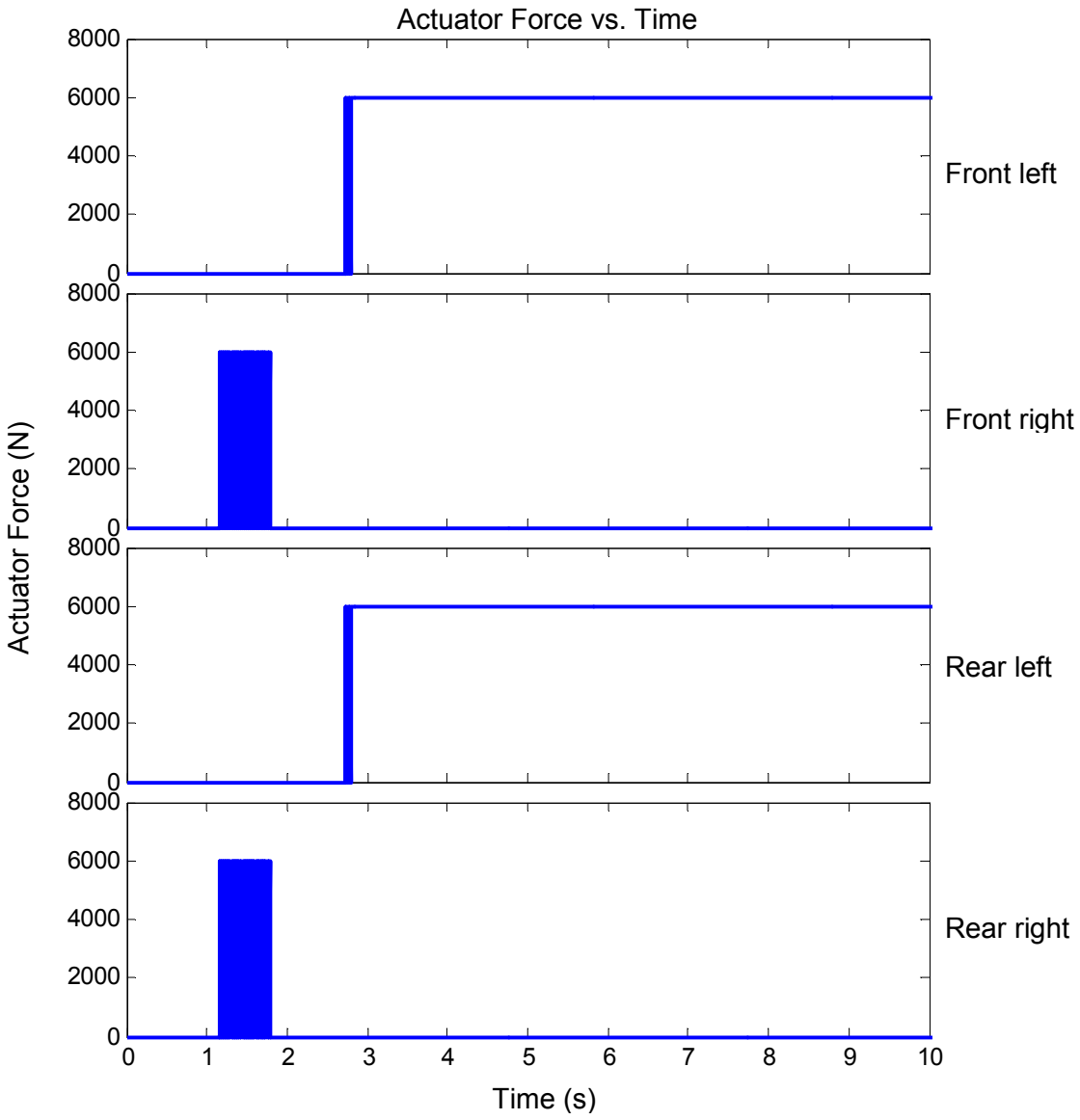

Figure 7.21. Actuator force vs. time from ERC for simulation on dirt

7.11: Conclusions

The physics of vehicle rollover were examined in order to gain insight on the important factors affecting vehicle rollover. Specifically, the static stability factor (SSF), equation (7.1), describes the lateral acceleration required to roll a vehicle over when the vehicle is treated as a single rigid body. An understanding of SSF is important for untripped rollover studies, which

are rollovers caused by inertial forces. The vehicle critical speed, equation (7.2), gives the lateral speed at which a vehicle can travel and strike an obstacle moving laterally and still not roll over. If a vehicle strikes an object moving at a lateral velocity greater in magnitude than the critical velocity, the vehicle will roll over and this is called a tripped rollover.

Two control algorithms were developed to minimize and prevent vehicle rollover. A controller based on Lyapunov stability criteria was developed to stabilize vehicle yaw moment. The controller incorporates an adaptive parameters matrix that allows for tire cornering stiffness estimation. The purpose of the direct yaw control (DYC) is to continuously apply a braking force to one of the four wheels to create a corrective yaw moment, as needed. An emergency roll controller (ERC) was also developed as an extra measure of rollover prevention. The ERC operates independently of the DYC and is activated when the vehicle crosses some threshold value of a rollover coefficient. Activation of the ERC includes the application of a vertical load to the vehicle body by actuators located in the vehicle suspension.

Emergency maneuvers were performed on the studied vehicle in the vehicle simulation environment. Untripped and tripped rollover scenarios were simulated on controlled and uncontrolled vehicles driven on dry asphalt. The results showed that a vehicle equipped with DYC has improved yaw response. The reduction of yaw rate leads to a decrease in vehicle lateral acceleration, reducing the likelihood of untripped rollover. Stabilized yaw moment also decreases the vehicle's lateral speed, which decreases the probability of tripped rollover. It was also demonstrated that the further addition of ERC provides a good extra measure of roll stability, especially when maximum braking is already being applied by the DYC during extreme maneuvers. The combined control system can reduce vehicle lateral acceleration and lateral

speed to lower the probability of untripped and tripped rollovers, respectively, however it does not ensure that the thresholds of SSF and critical speed will never be crossed.

Simulations were also run on simulated dirt and gravel surfaces by using the off-road tire models developed in chapter 5. The simulations showed the ability of the proposed control system to operate on a variety of driving surfaces. The DYC can be used on a variety of surfaces by changing the values in the adaptation gain matrix which allows for estimates of tire cornering stiffness. ERC is activated based on a rollover coefficient that can be calculated independent of the driving surface. The driving surface will affect the value of the rollover coefficient; however, the surface effects show up in the sprung mass lateral acceleration term of the rollover coefficient equation. The combination of DYC and ERC can significantly improve a vehicle's roll response and prevent vehicle rollover during some emergency maneuvers on a variety of driving surfaces. It should be understood that the implementation of the proposed control system does not guarantee rollover prevention. Vehicle rollover can still be caused by split-mu terrain, irregular driving surfaces geometry, and driver inputs.

Chapter 8: Conclusions and Recommendations

This chapter will first give a summary of the research that was performed. Next, it will provide the major conclusions developed along with recommendations for any user who chooses to use this research.

8.1: Summary of Research

The vehicle studied in this research has recently experienced an undesired number of rollovers due to severe maneuvers on off-road terrain. The tire is the single component on the vehicle responsible for transmitting all of the non-inertial forces and moments that govern the movement of the vehicle. As a result, it was important to study the tire and develop an accurate off-road tire model that affects the handling of the vehicle. The purpose of developing the tire model was to gain an understanding of vehicle handling behavior on off-road driving surfaces so that rollover mitigations strategies could be developed.

The research began by performing force and moment testing on the studied tire. This was accomplished by testing the studied tire on a rolling road. Force and moment responses were measured as a function of forward speed, vertical load, slip angle, and camber angle. The data collected from these tests was analyzed and processed using a developed Matlab routine to produce a set of Pacejka coefficients which were used in the off-road tire model.

Next, hardware control and data acquisition software was developed for an existing portable tire test rig to perform off-road tire tests. The rig is capable of recording tire force and moment response due to inputs such as forward speed, tire inflation pressure, vertical load, slip angle, and camber angle. Lateral force vs. slip angle tests at different vertical loads were performed on a passenger tire on dry asphalt, dirt, and gravel driving surfaces. This data was

then used with the previously developed force and moment tire model to create a lateral force tire model of the studied tire on dirt and gravel.

Next, stability control algorithms were developed to decrease the probability of rollover and prevent rollover of the studied vehicle. Specifically, direct yaw control (DYC) and emergency roll control (ERC) were used. The robustness of the controllers to prevent rollover on a variety of driving surfaces was investigated by performing vehicle simulations in the TruckSim environment. Emergency maneuvers were performed for the controlled and uncontrolled vehicle and vehicle yaw rate, roll angle, lateral speed, and lateral acceleration responses were observed.

8.2: Major Conclusions and Recommendations for Use of this Research

The scaling factors for dirt and gravel developed from this research include the scaling of the peak value and cornering stiffness of lateral force. The majority of the scaling from one surface to another can be modeled in the scaling of the peak value and cornering stiffness. These scaling factors provide a good approximation of the lateral force behavior of a tire on the respective surfaces, and are good for use in vehicle handling studies. However, the scaling applied in this research is not a complete scaling. It should be understood that the offsets with respect to the origin are not modeled by the proposed scaling factors, and that it is assumed that the offsets will be the same on all driving surfaces.

A direct yaw control stability algorithm based on Lyapunov direct method was implemented. It was found that the use of DYC can significantly improve a vehicle's yaw response and therefore improve the vehicle's roll response as well. The improvement of roll

response through DYC shows up in its ability to decrease the vehicle's lateral speed and lateral acceleration. Decreased lateral speed can significantly decrease the likelihood of a tripped rollover, as critical speed is a governing factor in whether or not a vehicle will roll over when it strikes an obstacle while moving laterally. Decreased lateral acceleration can significantly reduce the likelihood of an untripped rollover, as static stability factor is a governing factor in whether or not a vehicle will roll over due to inertial forces while cornering. The stabilization of vehicle yaw rate through DYC also helps to prevent vehicle skidding. When a vehicle goes into skidding, the driver loses the majority of his control over the vehicle. Skidding can cause the vehicle to strike obstacles, which can lead to tripped rollovers. DYC can significantly improve a vehicle's roll response and help to prevent vehicle rollover.

The further addition of the ERC provides another layer of roll protection in the potential untripped rollover situation. The ERC monitors the lateral acceleration of the vehicle and activates when the lateral acceleration approaches an unsafe value, defined as a percentage of the static stability factor of the vehicle. The ERC helps by decreasing the roll angle and lateral acceleration of the vehicle. This is beneficial when full braking is already being applied by the DYC.

Simulations were performed that show that DYC can significantly improve a vehicle's roll response during an emergency maneuver, as compared to the uncontrolled vehicle. It was further shown that ERC adds an extra layer of roll protection during extreme maneuvers and can further reduce the likelihood of vehicle rollover, primarily in the potential untripped situation.

The developed lateral force off-road tire model was also used in the simulations to assess the performance of the vehicle and the ability of the control algorithms to prevent rollover on

multiple surfaces. It was shown that the gains in the DYC can be changed to allow the controller to be affective when operating on different driving surfaces. Simulations run on dirt and gravel also showed that the DYC and ERC significantly improve the studied vehicle's handling and can prevent vehicle rollover during emergency maneuvers. The adaptive nature of the DYC to operate on different driving surfaces lies in its ability to estimate the tire cornering stiffness. The ERC is also operable on different driving surfaces because it operates on the measurement of the lateral acceleration of the vehicle. Assuming accuracy of the lateral acceleration sensor on the vehicle, the rollover coefficient accurately predicts a vehicles impending rollover regardless of the driving surface. The proposed control algorithms are operable on a variety of driving surfaces and significantly help to prevent vehicle rollover during emergency driving maneuvers.

It should be understood that the DYC and ERC operate independently of one another. It should also be understood that the DYC is not capable of predicting potential tripped rollovers, and is only capable of reducing the lateral speed of the vehicle, which helps in tripped rollover prevention. The driver should not rely on the control systems as a failsafe method for preventing rollover. The driver should be well-trained in operating the studied vehicle on off-road surfaces.

In conclusion, an off-road tire model was developed for the studied vehicle. The tire model was used as a basis for developing control algorithms that prevent vehicle rollover on a variety of driving surfaces. The developed control algorithms are operable on different driving surfaces and can effectively prevent vehicle rollover during some emergency maneuvers.

Chapter 9: Future Work

Future work related to this research should first include more extensive research on the scaling factors. This should include testing multiple tires of multiple sizes to further validate scaling factors as being primarily independent of tire type and size. Also, scaling factors should be determined for all of the main coefficients in the Magic Formula, not just peak value and cornering stiffness. This can be partially accomplished by making improvements to the tire test rig. These improvements include: more accurate measurements of slip angle and camber angle, ability to perform camber angle sweeps, and isolation of tire from trailer vibrations. It would also be beneficial to test on more driving surfaces, such as different types of gravel, different types of dirt, grass, sand, soft soil, mud, etc.

These extensions to the off-road tire model would further improve the vehicle handling studies. The control algorithms could be tested on more driving surfaces as well as split driving surfaces that consist of a combination of several of the tested surfaces. Also, all of the vehicle simulations in this research were performed on flat, level ground. In future studies, three dimensional surfaces with surfaces irregularities should be studied.

In addition, the proposed control algorithms can be implemented into a hardware-in-the-loop driving simulator to assess the controller performance for real-world driver steer, throttle, and brake inputs. Furthermore, an actual vehicle could be acquired and instrumented with lateral acceleration and yaw rate sensors to test how well the proposed TruckSim vehicle model matches actual vehicle performance. The vehicle could be driven on different surfaces, including split-mu surfaces with elevation irregularities. The proposed control algorithms could be implemented into the actual hardware of the vehicle to test the actual controller performance on the studied vehicle.

References

1. Pacejka, H.B., Bakker, E., *The Magic Formula Tyre Model.* Vehicle System Dynamics, 1992. **21**(S 1): p. 1 - 18.
2. Pacejka, H.B., Besselink, I.J.M., *Magic Formula Tyre Model with Transient Properties.* Vehicle System Dynamics, 1997. **27**(1): p. 234-249.
3. Pacejka, H.B., *Tire and Vehicle Dynamics*. Second ed. 2006: SAE International. 642.
4. Masahiko Mizuno, T.T., Masatoshi Hada, *Magic Formula Tire Model Using the Measured Data of a Vehicle Running on Actual Roads.* Advanced Vehicle Control (AVEC), 1998: p. 329 - 334.
5. Bakker, J.v.O.a.E., *Determination of Magic Formula Tyre Model Parameters.* Vehicle System Dynamics, 1992. **21**(Supplement 1 (S1)): p. 19 - 29.
6. Toshimichi Takahashi, M.H., *Modeling of Tire Overturning Moment Charactersitics and the Analysis of Their Influence on Vehicle Rollover Behavior.* R&D Review of Toyota CRDL, 2003. **38**(4): p. 10 - 16.
7. F. Braghin, F.C., E Sabbioni, *Environmental Effects on Pacejka's Scaling Factors.* Vehicle System Dynamics, 2006. **44**(7): p. 547 - 568.
8. Bakker, E., Nyborg, L., Pacejka, H.B. , *Tyre Modeling for Use in Vehicle Dynamics Studies.* SAE, 1987(870421): p. 1-15.
9. Bakker, E., Pacejka, H.B., Lidner L., *A New Tire Model with an Application in Vehicle Dynamics Studies.* SAE, 1989(890087): p. 83-95.
10. A. Ghazi Zadeh, A.F., *An Analytical Transient Tire Model.* Tire Science and Technology, 2001. **29**(2): p. 108 - 132.

11. Heydinger, G., Garrot, W., Chrstos, Jeffrey, *The Importance of Tire Lag on Simulated Transient Vehicle Response.* SAE, 1991(Document Number: 910235): p. 49 - 61.

12. Huston, J.S.a.J.C., *Lateral Stability Analysis of a 2 Degree-of-Freedom Vehicle Using a Time Lagged Lateral Tire Force Model.* SAE, 1999(Document Number: 1999-01-0791).

13. Loeb, J., Guenther, Dennis, Hung-Hsu, Fred Chen, *Lateral Stiffness, Cornering Stiffness and Relaxation Length of the Pneumatic Tire.* SAE, 1990(Document Number: 900129): p. 1 - 9.

14. Pacejka, J.P.M.a.H.B., *Relaxation Length Behaviour of Tyres.* Vehicle System Dynamics, 1997. **27**(Supplement 1): p. 339 - 342.

15. Pacejka, A.H.a.H.B., *The Relaxation Length Concept at Large Wheel Slip and Camber.* Vehicle System Dynamics, 1997. **27**(Supplement 1): p. 50 - 64.

16. Beauregard, W.B.a.C., *Transient Tire Properties.* SAE, 1974(Document Number: 740068).

17. Roper, L.D. (2001) *Physics of Automobile Rollover*.

18. Aleksander Hac, T.B., and John Martens, *Detection of Vehicle Rollover.* SAE, 2004(SAE Paper No. 2004-01-1757).

19. Peter J. Schubert, D.N., Edward J. Wallner, Henry Kong, Jan K. Schiffmann, *Electronics and Algorithms for Rollover Sensing.* SAE, 2004(SAE paper no. 2004-01-0343).

20. Ali Y. Ungoren, H.P., Danny R. Milot, *Rollover Propensity Evaluation of an SUV Equipped with a TRW VSC System.* SAE, 2001(SAE paper no. 2001-01-0128).

21. Hac, A., *Influence of Chassis Characteristics on Sustained Roll, Heave and Yaw Oscillations in Dynamic Rollover Testing.* SAE, 2005(SAE paper no. 2005-01-0398).

22. Seyed Hossein Tamaddoni, S.T. *A New Control Algorithm for Vehicle Stability Control*. in *10th International Conference on Advanced Vehicle and Tire Technologies*. 2008. New York City, New York.

23. Ding, N., *An Adaptive Integrated Algorithm for Active Front Steering and Direct Yaw Moment Control Based on Direct Lyapunov Method.* 2009.

24. Dirk Odenthal, T.B., Jurgen Ackerman, *Nonlinear Steering and Braking Control For Vehicle Rollover Avoidance*, in *European Control Conference*. 1999.

25. Hopkins, B., Fox, D., Caffee, J., Sides, B., Burke, W., Craft, M., Taheri, S., *Construction and Operational Verification of a Medium Duty Truck Tire Force and Moment Testing Trailer Suitable for On or Off Road Use*, in *Tire Society Conference*. 2009: Akron, OH.

26. Fox, D., *Design of a Portable Tire Test Rig and Vehicle Roll-Over Stability Control*, in *Mechanical Engineering*. 2009: Blacksburg.

Appendix A: Simulink Block Diagrams

This appendix contains the some of the Simulink block diagrams of the controllers discussed in Chapter 7. Figure A.1 shows the main block diagram with the emergency roll controller and direct yaw controller. The TruckSim S-Function block allows for the importing and exporting of variables from TruckSim to Simulink. Figure A.2 shows the contents of the Brake Selector/ Actuator block from figure A.1. Figure A.3 shows the contents of one of the torque calculation subsystems from figure A.2. Figure A.4 shows the contents of the Front Cornering Stiffness Estimation subsystem, which is located in the Cornering Stiffness Estimation clock in figure A.1. Figure A.5 shows the contents of the Stabilizing Yaw Moment subsystem from figure A.1

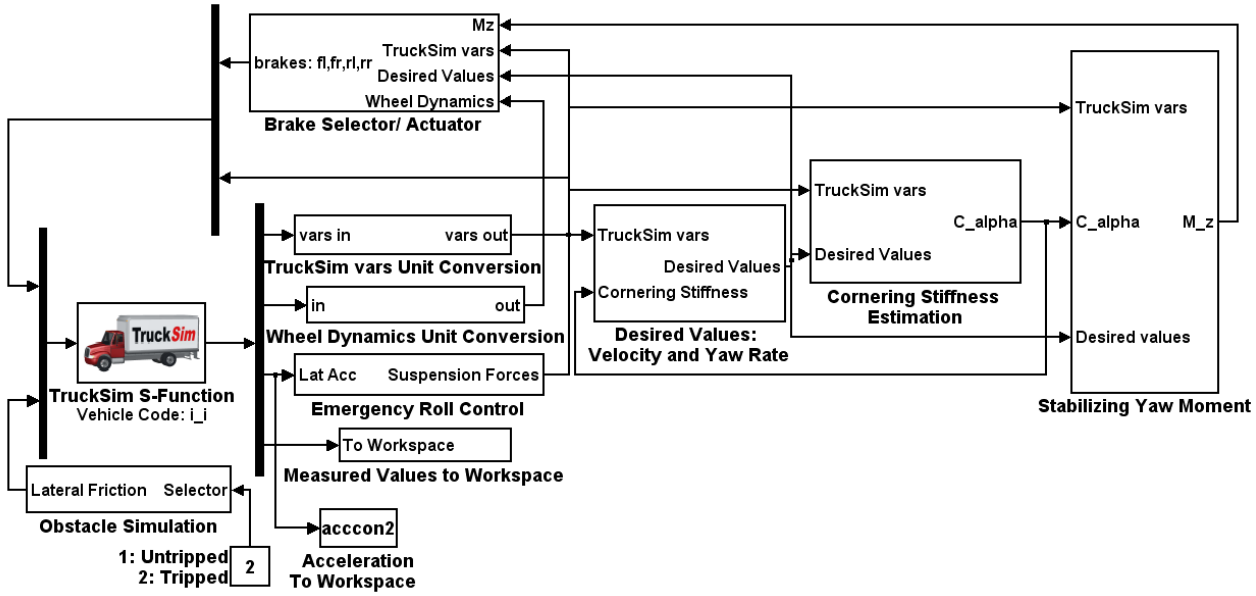

Figure A.1. Simulink model for DYC and ERC control algorithms

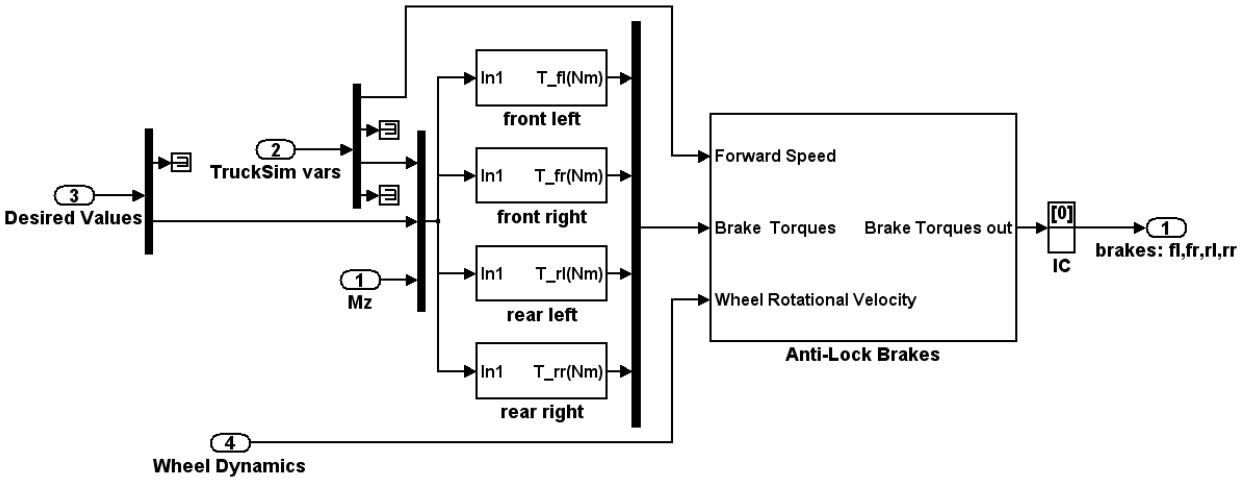

Figure A.2. Contents of Brake Selector/Actuator subsystem

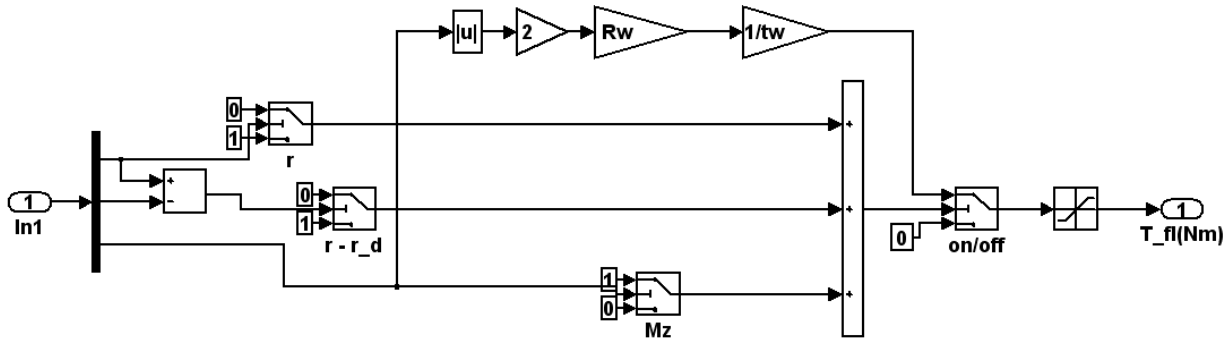

Figure A.3. Contents of torque calculation subsystem for front left wheel

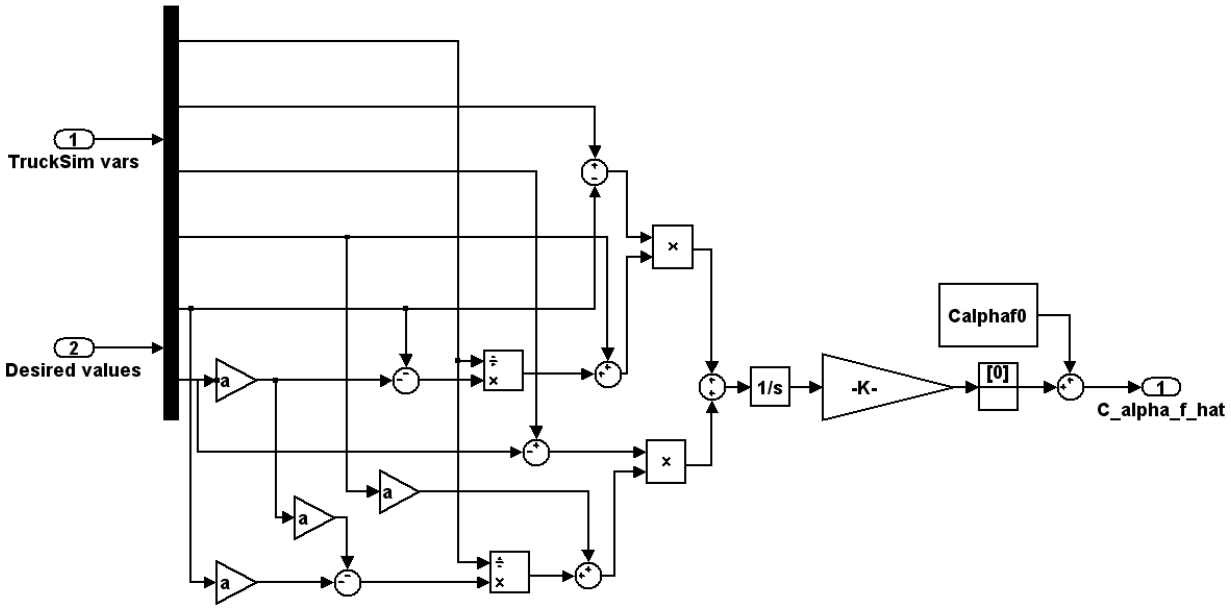

Figure A.4. Contents of Front Cornering Stiffness Estimation subsystem

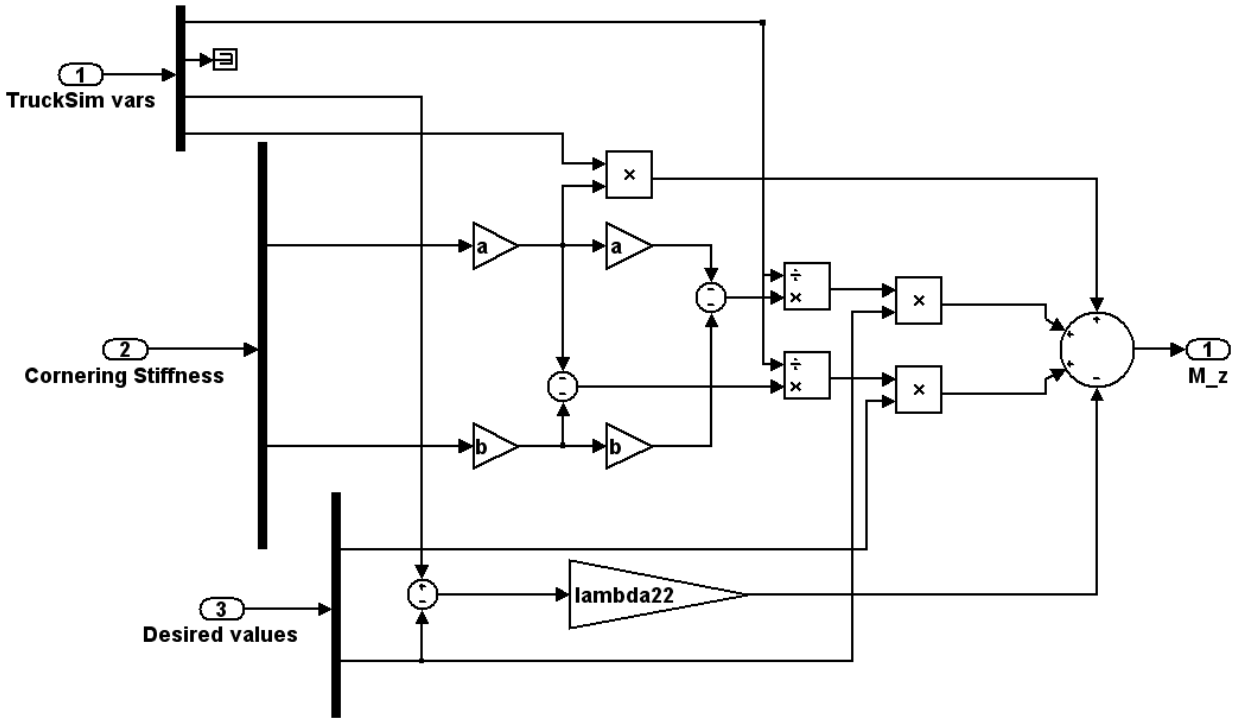

Figure A.5. Contents of Stabilizing Yaw Moment subsystem